Spatial control of light in nonlinear and periodic photonic structures

A thesis submitted for the degree
of Doctor of Philosophy of
the Australian National University

Christian Romer Rosberg

February 2008

THE AUSTRALIAN NATIONAL UNIVERSITY

Declaration

This thesis is an account of research undertaken in the Nonlinear Physics Centre and the Laser Physics Centre within the Research School of Physical Sciences and Engineering at the Australian National University between November 2004 and February 2008 while I was enrolled for the Doctor of Philosophy degree.

The research has been conducted under the supervision of Dr. Dragomir N. Neshev, Prof. Wieslaw Krolikowski, and Prof. Yuri S. Kivshar. However, unless specifically stated otherwise, the material presented within this thesis is my own.

None of the work presented here has ever been submitted for any degree at this or any other institution of learning.

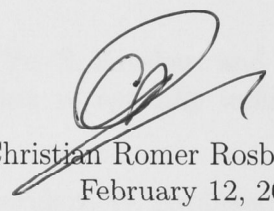

Christian Romer Rosberg
February 12, 2008

Refereed journal publications

1. **C. R. Rosberg**, F. H. Bennet, D. N. Neshev, P. D. Rasmussen, O. Bang, W. Krolikowski, A. Bjarklev, and Yu. S. Kivshar, *"Tunable diffraction and self-defocusing in liquid-filled photonic crystal fibers,"* Opt. Express **15**, 12145–12150 (2007).

2. **C. R. Rosberg**, D. N. Neshev, A. A. Sukhorukov, W. Krolikowski, and Yu. S. Kivshar, *"Observation of nonlinear self-trapping in triangular photonic lattices,"* Opt. Lett. **31**, 1498–1500 (2007).

3. **C. R. Rosberg**, D. N. Neshev, W. Krolikowski, A. Mitchell, R. A. Vicencio, M. I. Molina, and Yu. S. Kivshar, *"Observation of surface gap solitons in semi-infinite waveguide arrays,"* Phys. Rev. Lett. **97**, 083901–4 (2006).

4. **C. R. Rosberg**, I. L. Garanovich, A. A. Sukhorukov, D. N. Neshev, W. Krolikowski, and Yu. S. Kivshar, *"Demonstration of all-optical beam steering in modulated photonic lattices,"* Opt. Lett. **31**, 1498–1500 (2006).

5. M. Matuszewski, **C. R. Rosberg**, D. N. Neshev, A. A. Sukhorukov, A. Mitchell, M. Trippenbach, M. W. Austin, W. Krolikowski, and Yu. S. Kivshar, *"Crossover from self-defocusing to discrete trapping in nonlinear waveguide arrays,"* Opt. Express **14**, 254–259 (2006).

6. **C. R. Rosberg**, D. N. Neshev, A. A. Sukhorukov, Yu. S. Kivshar, and W. Krolikowski, *"Tunable positive and negative refraction in optically induced photonic lattices,"* Opt. Lett. **30**, 2293–2295 (2005).

7. **C. R. Rosberg**, B. Hanna, D. N. Neshev, A. A. Sukhorukov, W. Krolikowski, and Yu. S. Kivshar, *"Discrete interband mutual focusing in nonlinear photonic lattices,"* Opt. Express **13**, 5369–5376 (2005).

Other publications

1. **C. R. Rosberg**, R. Fischer, and A. Prasad, *"Long-distance learning: teaching optics in the outback,"* Optics and Photonics News **18**(6), 22–23 (2007).

2. **C. R. Rosberg**, R. Fischer, and A. Prasad, *"Optics in the outback,"* Australian Optical Society News **21**(2), 11–12 (2007).

3. **C. R. Rosberg**, D. N. Neshev, Ya. V. Kartashov, R. A. Vicencio, W. Krolikowski, M. I. Molina, A. Mitchell, V. A. Vysloukh, L. Torner, and Yu. S. Kivshar, *"Nonlinear Tamm states in periodic photonic structures,"* Optics and Photonics News **17**(12), 29 (2006).

4. **C. R. Rosberg**, D. N. Neshev, A. A. Sukhorukov, W. Krolikowski, and Yu. S. Kivshar, *"Tunable negative refraction of light in photonic lattices,"* Optics and Photonics News **16**(12), 38 (2005).

Acknowledgments

First of all I wish to thank the members of my supervisory panel, Dr. Dragomir Neshev, Prof. Wieslaw Krolikowski, and Prof. Yuri Kivshar, for excellent support and guidance throughout the time that I have been with the group. They have followed the progress of my work with constant attention, providing inspiration, help, and encouragement whenever needed, and I am deeply indebted to all of them for this and for all that I have learned and achieved.

Thanks to the staff and students from the Nonlinear Physics Centre who, lead by Prof. Kivshar's enthusiasm and ability to encourage others, constitute a great research team in which professionalism and personal respect go hand in hand. I am grateful in particular to Dr. Andrey Sukhorukov, Dr. Michal Matuszewski, fellow PhD students Ivan Garanovich and Aliaksandr Minovich, and visitors to our department Alex Szameit and Per Dalgaard Rasmussen, for useful discussions and for help with simulations and theory. Thanks also to former student Brendan Hanna, for the introduction to the research subjects and to the experiments in the lab. I have enjoyed supervising and working closely with honours student Francis Bennet, and I am very glad that he will pursue our efforts in establishing a new research direction in the group based on infiltrated structures.

Arnan Mitchell and his team from the RMIT University in Melbourne provided crucial components for several of my studies. Without their expertise in the fabrication of high quality waveguide structures I would never have been able to perform the experiments I did, so I wish to thank Arnan many times for a great collaboration. Likewise I thank my advisor Dr. Ole Bang and Prof. Anders Bjarklev for their great enthusiasm and commitment to our collaborative projects, for providing the photonic crystal fiber samples used in my experiments, and for supporting my visits to their group at the Technical University of Denmark.

Establishing links with research groups overseas is a privilege and an essential part of career development, and I would therefore like to warmly thank Prof. Mark Saffman, at the University of Wisconsin, and Dr. Zhigang Chen, at the San Francisco State University, for supporting my visits to their labs and for sharing their knowledge with me. Along the same lines I would like to thank Prof. Robert Crompton and his wife Helen for showing a great interest in the students and their research at our school, and for providing very genereous support for my overseas conference travel through the Robert and Helen Crompton Scholarship for Travel.

Thanks to all the students who joined me in the adventure of establishing and

running a local student chapter of the Optical Society of America at the Australian National University. The various outreach programs and related activities that we organised have greatly enriched our personal and professional lives and, together with the interaction that I have enjoyed with fellow student chapter members around the world, represent an invaluable part of my PhD experience. Thanks in particular to Robert Fischer for help with planning and realising the "Optics in the Outback" [1] project - what a great trip we had - and to Amrita Prasad for taking over as chapter President after me.

I gratefully acknowledge advice and technical assistance at many occasions from Maryla Krolikowska, Craig MacLeod, and John Bottega, from the Laser Physics Centre.

I also wish to thank our departmental administrator Wendy Quinn, her successor Kathleen Hicks, Prof. Neil Manson, and student officer Liudmila Mangos, for excellent support in sorting out all sorts of administrative and practical issues in the course of my PhD program at the school. I never had to ask twice for help in any such matters, and this has been an important factor allowing me to focus on the research.

Finally, I acknowledge the financial support provided by the Australian Government, the Australian National University, and the ARC Centre of Excellence "Centre for Ultrahigh-bandwidth Devices for Optical Systems" (CUDOS), without which I would not have been able to carry out the research and obtain the results presented in this thesis.

Abstract

The combination of nonlinearity and periodicity in optical media gives rise to a wealth of novel physical effects and unique opportunities for control and manipulation of the propagation of light. This has become evident over the last decades by the surge of interest in photonic crystal research and related areas. Many important and emerging applications such as all-optical switching, supercontinuum generation, and optical sensor devices are based on the fundamentals of light propagation in nonlinear and periodic optical structures.

Experimental studies in the field rely on access to physical systems that exhibit both appropriate periodicity and nonlinearity. It is the purpose of this thesis to explore a number of different experimental platforms and geometries for the study of discrete light propagation in nonlinear and periodic media, and to exploit the unique advantages of each of them to demonstrate novel effects with potential applications in active photonic devices. The work focuses on structures and material systems which offer dynamic tunability of the optical properties and which allow for observation of nonlinear effects at moderate laser powers.

Chapter 1 provides a general introduction to the subject and a brief overview of some of the previous experiments in the field of discrete nonlinear optics, providing the background and motivation for the research carried out in this thesis. The fundamental aspects of wave propagation in nonlinear and periodic media are briefly introduced, with emphasis on the rich effects arising from the combination of nonlinearity and periodicity. These include the unique diffractive properties of periodic media, and the appearance of families of self-trapped optical beams including discrete and gap spatial solitons.

Chapter 2 describes a series of experiments on linear and nonlinear light propagation in one-dimensional optically induced photonic lattices in biased photorefractive strontium barium niobate crystals. We start out by showing how selective excitation of optical Bloch waves can be realised experimentally with a multiple probe beam technique. This is motivated by the fact that the unique diffractive properties of periodic structures give rise to a host of interesting linear and nonlinear effects: selective Bloch wave excitation is first used to study the *nonlinear interaction* of co-propagating beams associated with the edges of the linear transmission bands, leading to the observation of mutual interband beam focusing and simultaneous self-focusing, defocusing, and spatial reshaping of beams with different diffractive characteristics. Next it is demonstrated that by tilting the optically induced lat-

tice by a small angle, probe beams associated with specific Bloch waves refract in different directions, and that this *beam steering* can be dynamically tuned by modifying the lattice depth through external tuning of the bias voltage. Finally optically controlled steering of self-localised beams is demonstrated in a lattice which is modulated by a third plane wave control beam.

Moving on to the study of fabricated nonlinear periodic structures, Chapter 3 presents the results of two experiments on discrete self-trapping of light in planar lithium niobate waveguide arrays. The photovoltaic self-defocusing nonlinearity exhibited by this material system opens up new possibilities for the study of beam localisation in the Bragg reflection bandgap. The generation of strongly localised gap solitons is demonstrated by use of a single beam excitation scheme which greatly simplifies experimental efforts and reveals new physics of the self-trapping mechanism. Subsequently the boundaries of the fabricated lattice structure are explored in the study of nonlinear surface waves, and surface gap solitons - a nonlinear optical equivalent of electronic Tamm states - are observed at the edge of a semi-infinite waveguide array.

Chapter 4 explores linear and nonlinear beam propagation in two-dimensional periodic structures. Returning briefly to the optical induction technique, we first demonstrate discrete diffraction and beam self-trapping in an optically induced triangular photonic lattice with self-focusing nonlinearity. Next we propose and develop a novel experimental platform for discrete nonlinear optics based on microstructured fibers infiltrated with nonlinear liquids. Exploiting the strong thermo-optic response of the infiltrated liquids, we demonstrate tunable discrete diffraction and thermal nonlinear beam self-defocusing in a triangular fiber waveguide array. Finally, based on the observed effects, we realise a compact all-optical power limiting device with tunable characteristics.

Contents

CHAPTER 1

Introduction to nonlinear and periodic optical media

1.1 Introduction

Nonlinearity is a universal phenomenon which appears across many different branches of physics. Nonlinearity in general results from the interaction or coupling between individual parameters of a system, leading to complex behaviour which is known to cause a wealth of interesting and often surprising effects.

In optics, nonlinearity is at the heart of many effects of both fundamental and practical importance, for example frequency conversion and harmonic generation. Optical nonlinearity originates from the interaction between intense light waves and the optical materials through which they propagate, resulting in a local modification of the polarisation density and the refractive index. As a consequence of nonlinearity, an optical beam can dynamically affect its own propagation, or the propagation of other beams. Light waves can thus interact with each other in a nonlinear medium. Another example of a fundamental concept in nonlinear optics is the optical soliton, which is a self-trapped optical wave that does not change its shape upon propagation. The formation of an optical soliton is possible when the nonlinear response from an optical material counteracts the effects of diffraction and dispersion, leading to the localisation of the optical wave in time or space, respectively. Nonlinear beam interaction and self-action effects represent invaluable tools for the study of the nature of light, and in addition show great promise for the realisation of efficient and dynamic control of optical beams and signals for applications, for example in all-optical technologies.

Periodicity is another fundamental concept found in many forms throughout nature. One of the prime examples is the regular arrangement of atoms in crystalline lattices. The physics of such systems is very rich and has been extensively studied. Periodic crystal potentials can be used to efficiently control the flow of electrons, and this represents one of the fundamental principles behind the development and ongoing advances of the microelectronics industry.

In optics, periodicity is associated with materials that exhibit a refractive index modulation in one or more spatial dimensions. Generic examples include optical gratings, slab waveguides, waveguide arrays and, introduced more recently, photonic

crystals and photonic crystal fibers. Periodic photonic structures can be used to control the flow of light in a way quite similar to the case of electrons in periodic electronic potentials, and thus hold an immense potential for the realisation of optical integrated circuits e.g. for optical computing, signal processing, and fiber communication systems. Much of today's research in optics is thus directed at exploring periodicity effects in photonic micro and nano-structures.

The *combination* of nonlinearity *and* periodicity in optical systems introduces new and enhanced possibilities for controlling the flow of light, and in particular shows inherent advantages for dynamically tunable and all-optical operation. The aim of the research described in this thesis is to explore schemes for achieving dynamic spatial control of light in optical structures exhibiting both periodicity and strong nonlinearity. Linear and nonlinear beam propagation effects of both fundamental and practical character are studied in a number of different experimental systems, namely: (i) optically induced lattices in biased photorefractive crystals; (ii) fabricated planar waveguide arrays; and (iii) liquid-filled microstructured optical fibers. Furthermore, dynamic tunability of the investigated photonic structures is explored as a means of achieving additional functionality and experimental flexibility.

This Chapter introduces the fundamental concepts necessary for the understanding of the experiments carried out in the thesis, as well as the historical background and context of the work. In Section 1.2, some of the basic aspects associated with the appearance of nonlinearity in optics are explained. Sections 1.3 and 1.4 discuss the particular types of nonlinearity employed in our studies, namely the photorefractive and thermal nonlinearities. Section 1.5 then introduces the nonlinear effects of self-focusing and self-defocusing which play a central role in the formation of spatial solitons, which are discussed subsequently in Section 1.6. Section 1.7 presents the fundamentals of light propagation in periodic photonic structures, and introduces the use of both discrete models and the Bloch wave formalism in the description of such systems. Finally, bringing together the effects of nonlinearity and periodicity, Section 1.8 explains and discusses the unique types of spatial solitons that can exist in periodic structures. Section 1.9 provides a historical summary of the developments in the field, which serves as a motivation for the scope and structure of the thesis outlined in Section 1.10.

1.2 Nonlinearity in optics

In linear systems, the principle of superposition applies. A linear system's response to a number of inputs is equal to the sum of its response to each individual input. Mathematically, this can be expressed as

$$F(a+b) = F(a) + F(b), \tag{1.1}$$

where F is a function which characterises the response of the system, and a and b represent two separat inputs. Many physical systems behave linearly for small inputs, whereas they become nonlinear for larger inputs. The use of the terms

"linearity" and "nonlinearity" is linked to the fact that the equations that describe a system's behaviour can be either linear or nonlinear. Whereas this mathematical distinction is clear, it is often impossible to strictly categorise a physical system as being either linear or nonlinear. In fact, linearity in physics typically represents an idealised *first order* approximation to a more complex nonlinear problem.

Sometimes nonlinearity is a nuisance because it complicates theoretical and computational analysis and introduces effects that deteriorate the linear performance of the system. On the other hand, there is a wealth of situations where physical processes can benefit from nonlinearity, and where nonlinearity leads to rich and novel effects which cannot be observed in linear systems.

In free space, the propagation of light in the form of electromagnetic waves, as governed by Maxwell's equations, is a truly linear problem. As a consequence of this, individual light beams cannot interact with each other, and once emitted from a source light cannot change its frequency. However, when light propagates in physical media such as dielectric materials, nonlinearity can appear as a result of interaction between the optical field and the atoms in the medium. The nonlinear interaction in general modifies the optical properties (refractive index) of the material which in turn affects the light propagation. This *feedback type* coupling of light and matter is manifested mathematically through the appearence of nonlinear terms in the governing equations. As a result, it is possible for an intense light beam to interact with itself or other beams, and remarkable effects such as energy exchange and optical frequency shifting can occur.

Nonlinear effects have been of great fundamental and practical interest in optics since the invention of the laser in the 1960's. However, in most typical optical materials, including fused silica, very high light intensities are required in order to experimentally observe nonlinear effects. It is also important to remember that optical nonlinearity is a property of the material, rather than of the light field itself. If the physical medium is removed any nonlinear effect will cease. Optical rectification, harmonic generation, frequency conversion, pulse generation, optical bistability, self-phase modulation, self-focusing, and soliton formation are all nonlinear effects, which can occur only inside a medium which provides an appropriate nonlinear response to an applied optical field. The same is true for effects such as four-wave mixing, parametric generation and amplification, and cross phase modulation, which rely on an *interaction* of two or more optical waves, mediated by a nonlinear medium.

1.2.1 Nonlinear susceptibility and refractive index

In the framework of classical electromagnetic theory, light-matter interaction is characterised by the relationship between the polarisation density P of the medium and the electric field E associated with the light wave. The polarisation density represents the medium's response to the applied electric field. In linear dielectric media

$$P = \epsilon_0 \chi E, \tag{1.2}$$

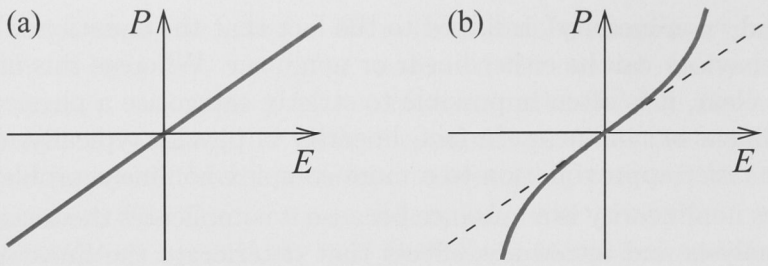

Figure 1.1: The relationship between electric field E and polarisation density P in (a) a linear medium and (b) a nonlinear medium.

where ϵ_0 is the permittivity of free space and χ is the (linear) electric susceptibility of the medium. The relation between the susceptibility and the refractive index n of the material is given by

$$n^2 = 1 + \chi. \tag{1.3}$$

Any departure from the linear relationship (1.2) between E and P is a manifestation of a nonlinear interaction. In most situations, nonlinearity is relatively small and can be treated as a perturbation to the linear relation, which only becomes significant when E is large (see Fig. 1.1). It is therefore possible to expand P in a Taylor's series about $E = 0$, using only a few terms. In common notation, the expansion reads [2]

$$P = \epsilon_0(\chi^{(1)}E + \chi^{(2)}E^2 + \chi^{(3)}E^3 + ...), \tag{1.4}$$

where $\chi^{(1)}$ represents the linear susceptibility, and $\chi^{(n)}$ is the n-th order nonlinear correction. Thus, in a nonlinear material, the susceptibility and hence the refractive index are not constant, but depend on the value of the electric field E. The nonlinear expansion coeffecients, $\chi^{(n)}$, characterise the nature and strength of the nonlinear interaction between the optical field and a particular material.

1.2.2 The electro-optic Pockels effect

In non-centrosymmetric media, including certain crystalline systems, the second order correction to the susceptibility is the dominating nonlinear term in Eq. (1.4). $\chi^{(2)}$ materials can exhibit the electro-optic Pockels effect, i.e. a linear change in refractive index in response to a DC electric field (e.g. applied through external electrodes). The macroscopic Pockels effect is often described by the equation [2]

$$\Delta n = -\frac{1}{2}n^3 r E_{DC}, \tag{1.5}$$

where Δn is the refractive index change, r is the Pockels coefficient (or linear electro-optic coefficient), and E_{DC} is the applied electric field. The Pockels coefficient characterises the strength of the electro-optic response of the material, and it is related to the nonlinear expansion coefficient $\chi^{(2)}$ in Eq. (1.4) [2]. Interestingly, the

refractive index change can be either positive or negative depending on the polarity of the applied field E_{DC}.

In a more general description, which takes into account material anisotropy, the electro-optic response is characterised by a tensor rather than a single Pockels coefficient, and the values of the individual tensor elements, r_{ijk}, are determined by the symmetry properties and the specific physical properties of the material. In anisotropic materials, the electro-optic response can thus depend strongly on the polarisation of light and its direction of propagation. This effect is exploited later in the thesis in the implementation of optically induced lattices [see Section 2.2].

1.2.3 The optical Kerr effect

In centrosymmetric media, the second order nonlinear susceptibility vanishes due to the requirement of inversion symmetry and, in this case, the third order term $\chi^{(3)}$ is the leading nonlinear correction. The refractive index change in case of third order nonlinearity is proportional to the *intensity* I of the optical field such that $\Delta n = n_2 I$ and

$$n(I) = n_0 + n_2 I, \tag{1.6}$$

where n_0 is the unperturbed linear refractive index, $I = |E|^2/2\eta$, $\eta = \eta_0/n_0$, $\eta_0 = (\mu_0/\epsilon_0)^{1/2}$, μ_0 is the permeability of free space, and the nonlinear material coefficient $n_2 = 3\eta_0/(n^2\epsilon_0)\chi^{(3)}$ [2]. The effect described by Eq. (1.6) is known as the optical Kerr effect, and it is at the heart of many fundamental effects observed in nonlinear optics [2, 3].

1.2.4 The nonlinear wave equation

In a dielectric medium with no free charges and no currents, the wave equation derived from Maxwell's equations reads

$$\nabla^2 E - \frac{1}{c_0^2}\frac{\partial^2 E}{\partial t^2} = \mu_0 \frac{\partial^2 P}{\partial t^2}, \tag{1.7}$$

where c_0 is the speed of light in free space, and P is given by the nonlinear expansion (1.4).

When driven by an optical field $E(\omega)$ oscillating at frequency ω, the nonlinear polarisation term on the right hand side of Eq. (1.7) can act as a radiation source emitting higher order frequency components (e.g. at 2ω and 3ω) which are not present in the original field $E(\omega)$. In $\chi^{(2)}$-materials, this can lead to second harmonic generation or optical rectification, i.e. the appearance of field components at 2ω and 0 frequency in response to an applied field at frequency ω. It can also lead to three-wave mixing resulting in sum or difference frequency generation ($\omega_1 \pm \omega_2$) in response to the interaction of two waves at frequencies ω_1 and ω_2.

In $\chi^{(3)}$ materials, processes like third harmonic generation (3ω) and four-wave mixing can occur. Although not exploited in this thesis, such frequency generation and conversion effects in $\chi^{(2)}$ and $\chi^{(3)}$ media represent some of the most intriguing and useful applications in nonlinear optics.

1.2.5 Physical mechanisms behind optical nonlinearity

For the purpose of this thesis, optical nonlinearity can be summarised as the ability of light to macroscopically modify the refractive index of the material through which it propagates, e.g. as described by the Kerr law [Eq. (1.6)]. In fact a multitude of different physical mechanisms can be responsible for the appearance of an intensity dependent refractive index.

Regardless of its specific physical origin, the nonlinear optical response can be characterised on a macroscopic level by its effect on the refractive index, and thus by a function $n(I)$ which depends on the beam intensity I. Many types of nonlinearities behave effectively or approximately like the Kerr nonlinearity, i.e. the light induced refractive index change varies linearly with the optical intensity, and this provides a convenient way of theoretically treating many similar problems using the same macroscopic description of the nonlinear interaction [Eq. (1.6)].

In general, one can distinguish between two different classes of nonlinearities, namely: (i) fast nonlinearities and (ii) slow nonlinearities. **Fast nonlinearities** involve the local distortion of electronic potentials and the formation of induced atomic dipole moments in a nearly instantaneous response to the electric field of the optical wave. Such nonlinearities can exhibit response times on the order of picoseconds or femtoseconds, but require very large optical intensities in order for the nonlinear response to be of an appreciable size. In practice, this implies the use of pulsed lasers with peak powers exceeding hundreds of watts, and even then the achieved nonlinear effects are often modest in most materials. Fast nonlinearities are responsible for harmonic generation, where accelerated dipole moments on the atomic scale radiate harmonics at optical frequencies (as discussed in the previous Section).

Slow nonlinearities, on the other hand, rely on modification of the material on a scale much larger than that of the atomic electronic response and on a much longer time scale. Examples relevant to this thesis are photorefractive and thermal nonlinearities. The former rely on diffusion and drift of photo-excited mobile charge carriers in certain crystalline systems. Nonuniform charge distributions set up macroscopic space-charge fields which in combination with the electro-optic effect result in an effective optical nonlinerity (see Section 1.3). Thermal nonlinearity relies on absorption of optical power and thermo-optic effects (see Section 1.4).

Slow type nonlinearities can allow for nonlinear effects to be observed at intensities as low as microwatt or milliwatt levels, which represents a great advantage in experimental research. The dramatic decrease in power requirements is possible because the nonlinear processes do not depend on the instantaneous magnitude of the optical field, but rather on the combined (accumulative) effect of many successive small interaction events such as individual photon absorptions. Furthermore, slow nonlinearities are often of a saturable and a spatially dispersive (nonlocal) nature. For example, photorefractive nonlinearity can saturate when all available mobile charge carriers have been depleted after a certain time of illumination, while heat diffusion can cause a thermal nonlinear response to extend beyond the optical intensity profile itself.

For many practical applications of nonlinear optics, including optically controlled (all-optical) switching and signal processing in optical communication systems, a fast nonlinear response on the order of femtoseconds or picoseconds is essential. In other applications of nonlinear beam control, however, time scales may be less critical, and response times on the order of microseconds or milliseconds, as provided for example by thermal nonlinearity, may be sufficient to achieve a certain functionality. In such cases, the use of slow nonlinearities represents a number of unique experimental advantages, including the fact that much less sophisticated light sources, such as continuous-wave lasers, can be used.

From the point of view of fundamental research, where the aim is to demonstrate fundamental nonlinear phenomena, the response time associated with the particular physical process is often irrelevant. This thesis focusses mainly on such generic nonlinear *effects* of optical beam propagation. Many of the studied effects are of a universal nature in the sense that their essential features do not depend on the particular choice of nonlinearity and physical system. Although interesting, the physics of the underlying nonlinear mechanisms associated with a particular experimental system are therefore secondary in this context.

1.2.6 The nonlinear Schrödinger equation

The nonlinear *beam propagation* effects studied later in this thesis can be understood directly from the concept of the intensity dependent refractive index $n(I)$. The beam profile $I = I(x, y, z)$ in general depends on the three spatial coordinates x, y, and z. In addition, in nonuniform optical media such as periodically modulated structures, the linear refractive index itself depends explicitly on the spatial coordinates, such that $n = n(x, y, z, I)$.

We consider steady state propagation of continuous-wave laser beams, i.e. there is no time evolution of the electric field envelope. In this case, the electric field can be represented as a rapidly oscillating plane wave $\exp(-ikz)$ modulated by a slowly varying field envelope $\psi(x, y, z)$, where $k = n_0 k_0$ is the wavevector, n_0 is the (average) linear refractive index, $k_0 = \omega/c_0$, and ω is the angular optical frequency. Assuming in addition that $\partial^2\psi/\partial z^2 \approx 0$ (the paraxial approximation [2]) and that nonlinear perturbations Δn_{NL} are small compared to the linear refractive index, i.e. $\Delta n_{NL} \ll n_0$, the nonlinear wave equation [Eq. (1.7)] can be rewritten in the form of a time-independent nonlinear Schrödinger equation [2, 4],

$$i\frac{\partial\psi}{\partial z} + D\left(\frac{\partial^2\psi}{\partial x^2} + \frac{\partial^2\psi}{\partial y^2}\right) + \mathcal{F}(x, y, z, |\psi|^2)\psi = 0, \tag{1.8}$$

where $\psi(x, y, z)$ is the normalised electric field amplitude, x and y are the transverse coordinates, and z is the propagation coordinate, normalised to the characteristic values x_0, y_0, and z_0, respectively, $D = z_0\lambda/(4\pi n_0 x_0^2)$ is the diffraction coefficient, λ is the wavelength in vacuum, and n_0 is the average linear refractive index of the medium.

The first term of Eq. (1.8) describes the phase accumulation associated with longitudinal propagation along z, while the second term accounts for linear beam

diffraction in the transverse dimensions x and y. The larger the value of the diffraction coefficient D, the faster the beam diverges upon propagation. The function $\mathcal{F}(x, y, z, |\psi|^2)$ in general accounts for the effects of both (i) nonlinearity and (ii) material inhomogeneity, e.g. the presence of a periodic refractive index modulation, and hence depends explicitly on x, y, and z, as well as the beam intensity $I \propto |\psi|^2$.

Since the form of $\mathcal{F}(x, y, z, |\psi|^2)$ is not yet specified, Eq. (1.8) represents a general model which is widely applicable to a range of optical systems. As an example, the function $\mathcal{F}(x, y, z|\psi|^2) = -\gamma|\psi|^2$ describes a bulk medium with a nonlinear response which is a linear function of the light intensity $I \propto |\psi|^2$, as in the case of Kerr nonlinear media [cf. Section 1.2.3]. The magnitude and sign of the parameter γ characterises the strength and type of nonlinearity, respectively, where $\gamma > 0$ corresponds to self-focusing nonlinearity and $\gamma < 0$ corresponds to self-defocusing nonlinearity [see Section 1.5]. In our studies, Eq. (1.8) is used to simulate beam propagation in a number of different periodic nonlinear structures, and in each particular case, $\mathcal{F}(x, y, z, |\psi|^2)$ is chosen to appropriately account for a specific type of nonlinearity and periodic refractive index modulation [see e.g. Eq. (2.2) in Section 2.5.4].

In one-dimensional periodic structures with no beam dynamics in one of the transverse dimensions [see Section 1.7], Eq. (1.8) reduces to an equation involving only two spatial variables x and z, and in this case $\psi = \psi(x, z)$.

Equation (1.8) is widely used to study beam propagation effects in nonlinear optics. A similar nonlinear Schrödinger equation in which the propagation coordinate z is replaced by the time coordinate t (and the second term describes dispersion rather than diffraction) is commonly used to describe nonlinear pulse propagation in optical fibers [5].

1.3 Photorefractive nonlinearity

The photorefractive effect is a nonlinear process which can occur in certain non-centrosymmetric materials (predominantly crystals). Photorefractive crystals possess a high concentration of weakly bound charge carriers (electrons) which can be excited by a resonant light wave and thereby become mobile in the crystal potential. The photo-excited charge carriers redistribute nonuniformly in illuminated regions and set up internal *space-charge* fields which locally alter the refractive index through the electro-optic effect [cf. Eq. (1.5)]. The photorefractive crystals used in our experiments are strontium barium niobate (SBN) and lithium niobate ($LiNbO_3$). Other common photorefractive materials include potassium niobate ($KNbO_3$), barium titanate ($BaTiO_3$), bismuth titanate ($Bi_{12}TiO_{20}$), and gallium arsenide (GaAs).

The mobile charge carriers which produce the internal space-charge fields originate from impurity centres (crystal dopants) which create energy levels associated with defect states between the electronic valence and conduction bands of the photorefractive crystal. The impurity centres act as either donors or acceptors (or both), corresponding to the processes of charge carrier generation and recombination, respectively. The photorefractive process is illustrated in Fig. 1.2. In the presence of

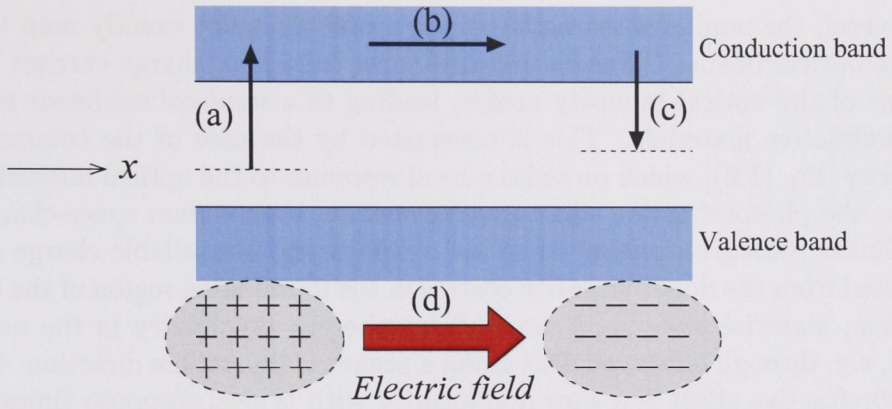

Figure 1.2: Schematic illustration of (a) photo-induced generation, (b) migration, and (c) recombination of mobile charge carriers, and (d) resulting space-charge field, in a photorefractive material. Energy levels marked by dashed lines between the valence and conduction bands represent impurity levels acting as (a) donors and (c) acceptors of free charge carriers.

an intense optical beam, photons are absorbed at impurity centres in the crystal, leading to the generation of mobile electrons [Fig. 1.2(a)]. The free charges migrate through the crystal [Fig. 1.2(b)], and eventually recombine at impurity centres located in darker regions further away from the beam centre [Fig. 1.2(c)]. The transfer of charge carriers within the crystal lattice leads to the formation of a space-charge electric field [Fig. 1.2(d)] which then produces an electro-optic modification of the refractive index [cf. Eq. (1.5)].

The photorefractive effect has interesting applications in optical memory technologies. When the illuminating beam is turned off, the redistributed charges can remain trapped in their respective locations in the crystal. In this way the photorefractive effect can be used to store information about an optical field $I(x, y, z)$ in the form of a refractive index modulation $\Delta n(x, y, z)$ which can subsequently be read out by a (weak) probe beam. The system can be brought back to its initial state at any time by subjecting it to bright background illumination or heating, ensuring a uniform redistribution of all mobile charge carriers. Among a number of applications exploiting such effects, photorefractive crystals can be used in real-time holography and phase conjugation [6]. However, in the context of our work, we are interested in how the photorefractive effect can provide a *nonlinear response that supports the formation and observation of spatial solitons and related beam propagation effects.*

The spatial redistribution of mobile charge carriers is governed by the effects of diffusion and drift. Diffusion causes charge carriers to migrate away from illuminated areas at a rate depending on the gradient of the optical intensity. Drift of charge carriers, on the other hand, is caused by electrostatic forces from electric fields, which may be externally applied fields or internal space-charge fields. The intensity profile of the optical field and the diffusion and drift mechanisms together determine the refractive index modulation arising from the photorefractive process.

In general, the nonlinear refractive index profile does not exactly map the profile of the optical beam. Diffusion and drift may transport charge carriers beyond the extent of the optical intensity profile, leading to a *nonlocal* nonlinear response in photorefractive materials. This is contrasted by the case of the common Kerr nonlinearity [Eq. (1.6)] which provides a local response to the optical intensity. Furthermore, the photorefractive effect is *saturable*, i.e. a maximum space-charge field and nonlinear refractive index change is reached when all available charge carriers are depleted from the donor impurity centres in the illuminated region of the crystal. In addition, material *anisotropy* can lead to inherent asymmetry in the nonlinear response, e.g. through enhanced drift along a preferred crystalline direction. Finally, the photorefractive effect is a slow nonlinearity with typical response times on the order of seconds. The dynamics associated with the generation, migration, and recombination of mobile charge carriers is complicated, but here we shall consider only beam propagation in situations where a steady state equilibrium is reached, i.e. when the charge carrier distribution and the nonlinear response do not change after a certain relaxation time. In most cases studied in this work, steady state is achieved within a few seconds of illumination.

Because of the inherent nonlocality, saturation, anisotropy, and complex dynamics associated with the photorefractive nonlinearity, it is important to carefully choose a particular regime of operation in order to achieve an appropriate nonlinear response for a given purpose. However, the difficulties caused by the above mentioned effects are often compensated for by the easy access to strong nonlinearity in photorefractive media, which is of great experimental value. The *screening* method described below is an attractive approach in which the effects of nonlocality and asymmetry are minimised, and where the saturation and the strength of the nonlinear response can be externally controlled. It is particularly suitable for the realisation and study of periodic nonlinear structures, as discussed in Section 2.2.

1.3.1 Screening of external electric field

Applying an external bias field to a photorefractive crystal such as SBN can lead to a strong enhancement of the nonlinear optical response. The idea behind this effect is that the applied field causes an increased drift of mobile charge carriers and correspondingly a stronger internal space-charge field which screens the external bias field in the regions of high intensity. In addition to enhancing the photerefractive nonlinearity, it is possible to reduce the effects of diffusion and inherent asymmetric drift, and achieve a quasi-local, quasi-symmetric nonlinear response.

Figure 1.3 illustrates the implementation of photorefractive screening nonlinearity for two cases: (i) a single Gaussian beam [Fig. 1.3, left] and (ii) an extended periodic intensity pattern [Fig. 1.3, right] such as the interference fringes created by two plane waves intersecting at a small angle. The external field E_0 pointing to the right in the top of Fig. 1.3 is applied along the crystalline c-axis which provides the largest Pockels coefficient and hence the strongest electro-optic response [cf. Section 1.2.2]. This direction also determines the orientation of the transverse beam dimension x. Figure 1.3 shows (a) the transverse beam intensity profile, (b) the

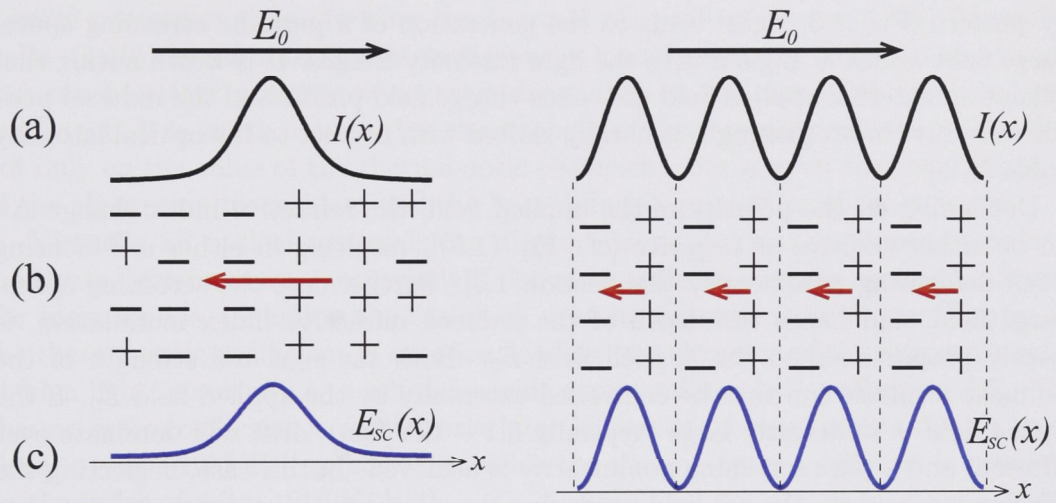

Figure 1.3: Generation of an internal space-charge field in response to local illumination of a biased photorefractive crystal when the drift of mobile charge carriers is dominated by the external electric field E_0 applied along the crystalline c-axis. The schematic illustrates the cases of a single beam (left) and an extended periodic intensity pattern (right). (a) Intensity profile of the illuminating beam $I(x)$; (b) distribution of photo-excited charge carriers (+ and -) under the influene of E_0. The resulting space-charge field is indicated by red arrows; (c) profile of the space-charge field E_{SC}, screening the applied electric field E_0 in the illuminated areas. The corresponding electro-optically induced refractive index change maps the space-charge field profile E_{SC}.

distribution of photo-excited charge carriers (+ and -), and (c) the corresponding profile of the space-charge field $E_{SC}(x)$. The electro-optically induced refractive index change is directly proportional to the space-charge field $E_{SC}(x)$ and thus has a similar profile.

For the Gaussian beam [Fig. 1.3, left] the space-charge field essentially maps the beam intensity profile and, pointing in the opposite direction of E_0 [see Fig. 1.3(b), left], results in *screening* of the applied electric field in the illuminated areas (assuming $|E_0| > |E_{SC}|$). Comparing the beam intensity and space-charge field profiles [Fig. 1.3(a,c)] indicates that the screening technique provides a quasi-local and quasi-symmetric nonlinear response. Illumination by an extended sinusoidal intensity pattern [Fig. 1.3, right] leads to the generation of a periodic screening space-charge field, which is aligned with the light intensity fringes. It is worth noting that without an external applied field the space-charge field profile and the induced periodic refractive index grating is generally shifted with respect to the optical intensity profile [2, 6].

Depending on the polarity of the applied field, the refractive index change Δn can be either positive or negative [cf. Eq. (1.5)], resulting in either self-focusing or self-defocusing nonlinearity [see Section 1.5]. Furthermore the screening space-charge field, and hence the depth of the induced refractive index modulation, is directly proportional to the applied field E_0. Both the sign and strength of the nonlinear response can thus be controlled externally by the applied field E_0. If the applied field is sufficiently large (typically $0.1 - 1\text{kV/cm}$), drift will dominate over diffusion, and a pure screening nonlinearity is achieved. In this case, neglecting the diffusion mechanism, the net field producing the electro-optic response, i.e. the sum of space-charge and external fields, is given approximately as [7, 8]

$$E_{DC} = E_0 \frac{I_d}{I(x,y,z) + I_d}, \tag{1.9}$$

where E_0 is the applied field, $I(x,y,z)$ is the beam intensity, and I_d is the constant dark irradiance accounting for additional charge carriers excited thermally or by a uniform background illumination. The corresponding refractive index modulation is directly proportional to E_{DC} as given by Eq. (1.5). Equation (1.9) shows that in addition to the possibility of tuning the strength of the nonlinear response by varying the external field E_0, changing the crystal temperature or the background illumination and hence I_d can be used to modify the response, allowing in particular to control the saturation of the nonlinearity.

1.4 Thermal nonlinearity

Thermal nonlinearity is employed in our experiments on light propagation in liquid-infiltrated microstructured optical fibers [see Chapter 4]. Thermal nonlinearity is caused by heating of the optical material due to partial absorption of energy from propagating beams through an optical loss mechanism. The temperature change resulting from the heating process produces a refractive index change

which depends on the amount of absorbed energy and hence on the light intensity. Different physical effects may be responsible for the energy absorption and the resulting heating and nonlinear response. The relationship between the light induced temperature change ΔT and the resulting refractive index n can be described as [3]

$$n = n_0 + \left(\frac{dn}{dT}\right)\Delta T, \tag{1.10}$$

where n_0 is the refractive index of the medium in the absence of the beam, i.e. at ambient temperature, and (dn/dT) is the thermo-optic coefficient, a material specific parameter characterising the thermal response of the medium. According to Eq. (1.10) the refractive index change varies linearly with the temperature change, and can be either positive or negative depending on the sign of the thermo-optic coefficient. It is worth to note that the strength of the thermal nonlinearity depends not only on the value of the thermo-optic coefficient, but also on the characteristics of the absorption mechanism and the heat diffusion properties of the material.

Virtually all optical materials can display strong thermal nonlinearity, even at moderate light intensities, especially if doped in order to increase absorption losses. For most liquids, including the castor oil used in our experiments [see Chapter 4], the thermo-optic coefficient is *negative*, leading to a decrease of the refractive index at high light intensity, i.e. a self-defocusing type nonlinearity [see Section 1.5]. The thermo-optic coefficient is particularly large in liquids, in most cases taking a value close to -4×10^{-4} K^{-1}, whereas in solids the thermo-optic coefficient is typically on the order of $\pm 3 \times 10^{-5}$ K^{-1} [3].

Like the photorefractive effect, thermal nonlinearity is an inherently strong, but rather slow process. Whereas the local heating can be almost instantaneous when the laser beam is turned on, it takes longer time for the heat to disperse throughout the medium and hence for re-thermalisation to happen when light is switched of. In the case of continuous-wave laser operation, heating in the beam cross section is followed by heat diffusion which continuously redistributes the thermal energy throughout the structure. In this case thermal equilibrium and a steady state nonlinear response can typically be reached on a time scale of microseconds to milliseconds. The resulting temperature profile depends on the dimensions, geometry, boundary conditions, and heat conductance of the system. Therefore, although the thermo-optic effect as described by Eq. (1.10) in itself is simple, the dynamics associated with thermal diffusion can be complicated. Furthermore, the nonlinear response is generally *nonlocal*, i.e. the temperature profile and the corresponding refractive index change in steady state extend beyond the beam profile itself due to thermal diffusion. Nonlocality can have important consequences for the nonlinear beam propagation effects occuring in such systems [9].

1.5 Self-focusing and self-defocusing

We now turn our attention to the nonlinear effects of self-focusing and self-defocusing. They are a fundamental consequence of the intensity dependent refrac-

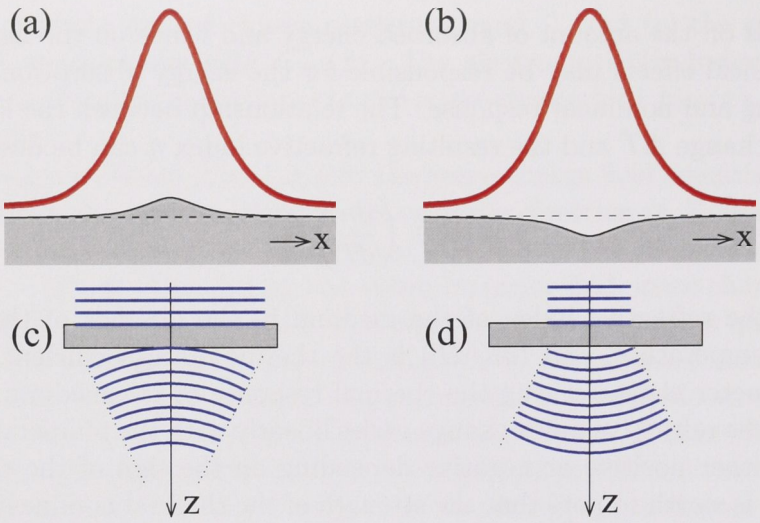

Figure 1.4: Schematic illustration of (a) self-focusing and (b) self-defocusing nonlinearity. In (a,b) the optical intensity profile is represented by the solid red curve, and the nonlinear refractive index profile by grey shading. Dashed line indicates the unperturbed linear index. (c,d) corresponding wavefront distortion induced by self-focusing and self-defocusing nonlinearity, respectively.

tive index introduced in Eq. (1.6) and constitute the conceptual basis for all spatial nonlinear effects studied in this thesis.

An optical wave of intensity I traveling through a nonlinear medium with an intensity dependent refractive index $n(I)$ experiences *self-phase modulation* according to $\Delta\phi = 2\pi/\lambda_0 Ln(I)$, where $\Delta\phi$ is the nonlinear phase shift acquired after a propagation distance L. The higher the intensity, the larger the induced change in refractive index and rate of phase accumulation.

A spatially finite laser beam with a non-uniform transverse intensity distribution $I(x, y)$ will experience uneven self-phase modulation over the beam cross section, and this strongly affects the evolution of the spatial beam profile upon propagation. For a bell shaped beam the nonlinear phase shift is largest in the beam centre and decreases away from the propagation axis in the wings of the beam, leading to a smooth distortion of the wavefront.

As illustrated in Fig. 1.4, this acts as to either *focus* or *defocus* the beam upon propagation, depending on the sign of the nonlinearity, i.e. whether the intensity induced change in refractive index is *positive* or *negative*. In the first case [Fig. 1.4(a,c)] a beam with an initially plane wave front will tend to focus since the phase velocity of the central high intensity region is decreased with respect to the wings of the beam. In the opposite case [Fig. 1.4(b,d)] self-phase modulation causes defocusing of the beam. In Fig. 1.4 the grey rectangles represent slabs of nonlinear material, and the blue lines illustrate the beam wavefronts before and after nonlinear self-

action inside the medium. The longitudinal propagation direction z is indicated by arrows.

1.6 Spatial optical solitons

Diffraction is a fundamental phenomenon leading to beam broadening upon propagation in linear media, and even in free space. In a nonlinear medium, self-focusing counteracts diffraction whereas self-defocusing on the other hand enhances the beam spreading.

In a situation where the nonlinear self-focusing exactly balances diffraction, the beam can propagate as a *spatial soliton*, i.e. a self-trapped beam preserving a constant, localised transverse profile upon propagation [4]. Figures 1.5(a,b) schematically illustrate (a) linear diffraction broadening in a homogeneous medium and (b) a nondiffracting spatial soliton propagating in a homogeneous medium with self-focusing nonlinearity. In this context a spatial soliton can be thought of as a nonlinear mode of a self-induced waveguide. Spatial solitons appear mathematically as solutions to the nonlinear Schrödinger equation [Eq. (1.8)], and in a bulk medium with Kerr like nonlinearity their one-dimensional transverse profile takes the form of a bell shaped hyperbolic-secant function which is independent of z.

In bulk media, self-defocusing nonlinearity clearly does not support the formation of *bright* solitons like the one sketched in Fig. 1.5(b). Self-defocusing, however, can be used to generate *dark* solitons, which are formed by the nonlinear localisation of a narrow dip in an otherwise uniform intensity background, as illustrated in Fig. 1.5(c). Experimentally bright solitons can be excited by shining a focused laser beam into a self-focusing material, and dark solitons can be observed in self-defocusing media by launching a broad beam with a zero intensity dip created e.g. by imprinting a π phase jump or a vortex phase singularity onto the beam.

The formation of spatial solitons by nonlinear compensation of diffraction is analog to the appearance of temporal (pulse) solitons in optical fibers, where self-phase modulation is used to balance dispersion such that the pulse shape is preserved upon propagation.

1.7 Periodic photonic structures

In homogeneous bulk media the refractive index is constant everywhere, except when locally modified by nonlinearity as discussed above. Periodic photonic structures, on the other hand, are optical media with an extended periodic refractive index modulation in either one, two, or three spatial dimensions. In this thesis we focus on one- and two-dimensional structures where periodicity appears in the transverse directions x and y, while we consider beam propagation along the z direction [see Fig. 1.6]. In Figs. 1.6(a,b) light and dark shading represents areas of low and high refractive index, respectively. The modulation period is d as shown in Fig. 1.6(a).

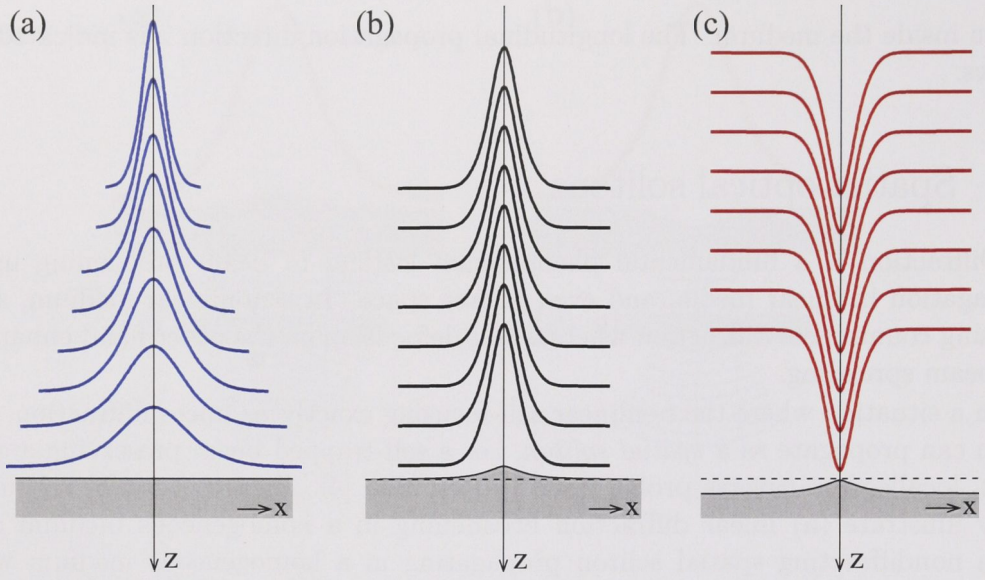

Figure 1.5: Schematic illustration of (a) linear diffraction broadening, (b) bright spatial soliton in a self-focusing nonlinear medium, and (c) dark spatial soliton in a self-defocusing medium. Grey shading indicates the refractive index profile.

For now, and in Chapters 2 and 3, we limit our discussions to the case of one-dimensional structures with one transverse direction of periodic modulation x, and a longitudinal propagation direction z [see Fig. 1.6(a)]. Many of the fundamental concepts introduced below can be extended to the two-dimensional case [Fig. 1.6(b)] which, in addition, offers the possibility of studying a range of diverse transverse geometries, including square and triangular (hexagonal) patterns. Chapter 4 is devoted to the study of two-dimensional structures.

As we shall see below the introduction of periodicity in a nonlinear optical medium greatly adds to the wealth of effects associated with self-focusing and self-defocusing, and the formation of spatial solitons. In addition periodicity and discreteness bring along a number of linear effects which are interesting in their own right in relation to their ability to spatially control light propagation.

1.7.1 Periodicity and discreteness

The periodic structures depicted in Figs. 1.6(a,b) may be seen as one- and two-dimensional arrays of individual slab and channel waveguides, respectively. The modal overlap between neighbouring waveguides determines to what extent guided light is able to redistribute throughout the structure by tunneling between individual sites through evanescent coupling. The coupling strength depends on waveguide spacing (d), refractive index contrast, and wavelength.

Light propagation in such periodic structures, or coupled waveguide arrays, may

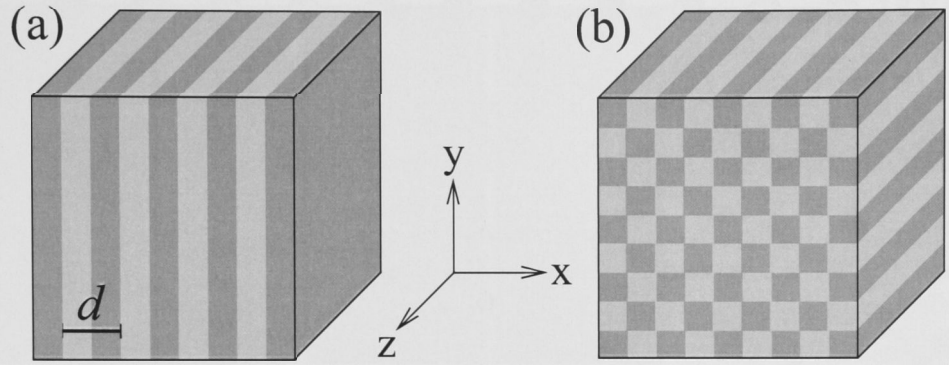

Figure 1.6: (a,b) Schematic illustration of a one-dimensional (a) and a two-dimensional (b) periodic photonic structure. Light and dark shading represent areas of low and high refractive index, respectively. d is the period of the refractive index modulation.

exhibit discrete behaviour [10] if the coupling between neighbouring waveguides is weak, i.e. if light is strongly confined to discrete points in space defined by well separated high index regions. Periodic photonic structures are often termed *photonic lattices* because of such discreteness. Fig. 1.7(a) schematically shows a one-dimensional discrete photonic lattice as a chain of coupled waveguide modes (circles). The corresponding refractive index profile may be step like, or it may be smooth as shown in Fig. 1.7(b). The maximum refractive index difference Δn, the lattice period d, and the waveguide geometry determines the strength of the inter-site coupling for light of a given wavelength, and hence the degree of discreteness exhibited by the system.

Theoretically light propagation in discrete nonlinear photonic lattices can be studied using the formalism of coupled-mode theory and the tight-binding approximation borrowed from solid state physics [11, 12]. In a one-dimensional waveguide array the discrete dynamics are then described by a differential equation,

$$i\frac{da_n}{dz} + \beta a_n + C(a_{n-1} + a_{n+1}) + \gamma|a_n|^2 a_n = 0, \tag{1.11}$$

where z is the propagation coordinate, $a_n(z)$ is the mode amplitude in the $n-$th waveguide [Fig. 1.7(a)], β is the propagation constant, and the coefficient C characterises the nearest-neighbour coupling between the waveguides. C is proportional to the mode overlap integral. The last term in Eq. (1.11) accounts for Kerr like nonlinear mode detuning through the intensity-dependent change of the refractive index. The coefficient γ characterises the nonlinear response which can be of either the self-focusing ($\gamma > 0$) or the self-defocusing ($\gamma < 0$) type. The continuous optical field profile can be approximately obtained by multiplying the individual waveguide mode profile by the corresponding discrete mode amplitude $a_n(z)$ for each site.

Historically, discrete models have been the preferred tool for analysing and modeling periodic systems, for the reason that they are computationally relatively easy

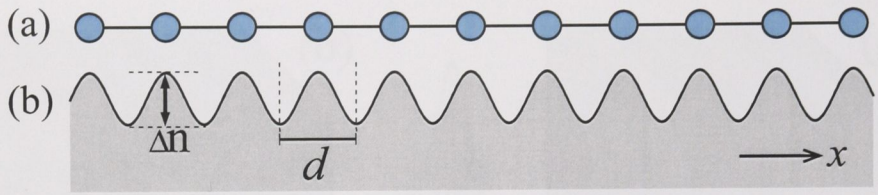

Figure 1.7: (a) Schematic representation of a one-dimensional discrete lattice and (b) the corresponding refractive index modulation. Δn indicates the effective modulation depth, and d is the lattice period.

to deal with, and in many cases give an accurate description of the physics of such systems.

1.7.2 Discrete diffraction and self-trapping

In bulk media a narrow Gaussian beam diffracts as illustrated in Fig. 1.5(a). The beam profile broadens in the transverse direction, but does not change its shape upon propagation. In discrete periodic media the picture is fundamentally different. When light is coupled into a single waveguide in a one-dimensional photonic lattice, it can experience *discrete diffraction* as shown in Fig. 1.8(a). Although light is guided in the waveguide by total internal reflection, energy can tunnel to adjacent waveguides by means of the evanescent coupling resulting from the nonzero overlap between the individual waveguide modes. As a result light is seen to oscillate back and forth between waveguides [Fig. 1.8(a)]. The effect resembles the periodic energy exchange in a directional coupler, i.e. the case of only two coupled waveguides [2]. In the extended array, however, the beam effectively broadens upon propagation, and energy is carried away from the beam centre in two dominant lobes in the wings of the beam [Fig. 1.8(a)]. In contrast to the case of bulk diffraction, the beam profile clearly changes qualitatively in the discrete system.

The rate at which the beam diffracts is related to the coupling coefficient C [Eq. (1.11)] such that the larger the waveguide coupling, the faster the energy is dispersed in the array. In a directional coupler consisting of two identical waveguides, the period of the energy exchange is π/C, and the so-called coupling length $L_C = \pi/(2C)$ thus determines the propagation distance required for all the beam energy to shift from one waveguide to the other [2]. In extended waveguide arrays, energy effectively disperses faster, and a characteristic discrete diffraction length L_D can therefore be defined as

$$L_D = \alpha \frac{2\pi}{C}, \tag{1.12}$$

where $\alpha < 1$ is a parameter chosen such that L_D corresponds to the propagation distance at which the intensity in the central waveguide first reaches a minimum [see Fig. 1.8(a)]. The total propagation distance in Fig. 1.8(a) corresponds to approximately three coupling lengths, and four discrete diffraction lengths.

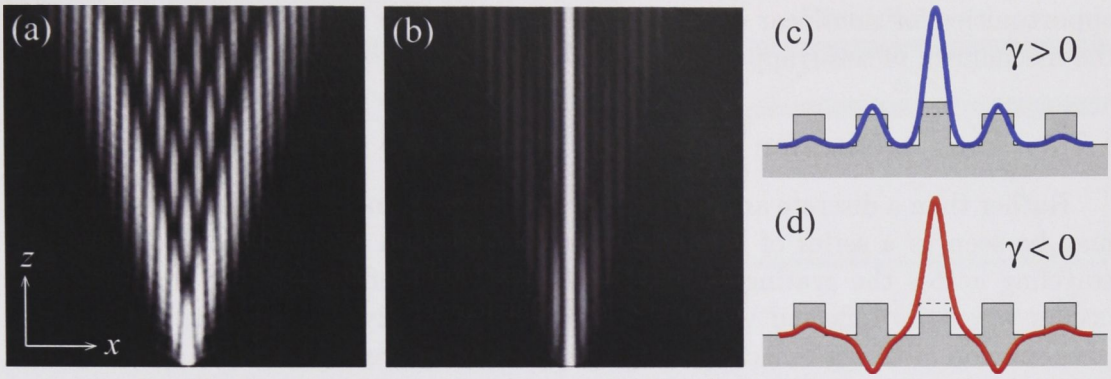

Figure 1.8: (a) Linear discrete diffraction and (b) nonlinear self-trapping in a one-dimensional photonic lattice. x and z are the transverse and propagation coordinates, respectively. Only one waveguide, in the centre of the array, is excited at the input. (c,d) schematic illustration of refractive index and corresponding spatial soliton profiles for self-focusing ($\gamma > 0$) and self-defocusing ($\gamma < 0$) nonlinearity, respectively.

In the nonlinear regime, for self-focusing nonlinearity ($\gamma > 0$), light can self-trap at high beam intensity and form a bright soliton in the lattice as shown in Fig. 1.8(b). This happens through the nonlinear mode detuning which decouples the central waveguide from the rest of the array [Fig. 1.8(c)]. The result is suppression of discrete diffraction, and the formation of a *discrete soliton* [12] which is locked to the input waveguide and its nearest neighbours [Fig. 1.8(c)].

In discrete lattices, surprisingly, the formation of bright solitons can also occur in case of self-defocusing nonlinearity ($\gamma < 0$). In this case nonlinear localisation happens at a negative type lattice defect, and the neighbouring mode amplitudes of the self-trapped beam are out of phase or *staggered* [13] [Fig. 1.8(c)]. This can be understood by noting that the form of Eq. (1.11) remains unchanged after the transformation: $a_n \rightarrow (-1)^n a_n^*$ and $\gamma \rightarrow -\gamma$, with the only difference being in the phase structure of the beam (i.e. the alternating sign of the mode amplitudes a_n). It follows that the nonlinear dynamics in the framework of Eq. (1.11) is fully equivalent for positive ($\gamma > 0$) and negative ($\gamma < 0$) nonlinearities, provided only a single lattice site is excited at the input, i.e. $a_n(z = 0) = 0$ for $n \neq 0$. In particular, when the input intensity is high enough, a soliton should form for either type of nonlinear response. In both cases [Figs. 1.8(c,d)] the discrete mode amplitudes of the self-trapped states can be found by numerically solving Eq. (1.11).

Nonlinear localisation at a positive type lattice defect [Fig. 1.8(d)] is somewhat similar to the effect of soliton formation in a bulk medium with self-focusing nonlinearity [Fig. 1.5(b)]. However, the possibility of achieving discrete self-trapping at a *negative* type lattice defect [Fig. 1.8(d)] stands in stark contrast to the case of bulk media, where self-defocusing nonlinearity does not support bright solitons. This is an important example of how periodicity and discreteness bring along new

opportunities for nonlinear control of light. In Chapter 3 we study in more detail the mechanism of self-trapping in self-defocusing waveguide arrays.

1.7.3 Bragg reflection in periodic structures

Rather than a discrete array of waveguides, a one-dimensional periodic structure may be seen as a series of Fresnel surfaces which each reflects part of the beams traveling across the grating. Strong scattering and reflection from the structure occurs when the reflected waves interfere constructively. This is the well known phenomenon of Bragg reflection which happens whenever

$$m\lambda/n_0 = 2d\sin(\theta), \tag{1.13}$$

where m is an integer, λ is the wavelength of light in vacuum, d is the period of the structure, n_0 is the average refractive index, and θ is the angle between the periodic grating and the initial propagation direction of the beam. To achieve Bragg reflection in a periodic structure one can tune the system to resonance by varying either the wavelength λ, the grating period d, the refractive index n_0, or the propagation direction θ. Here we will consider the latter case in which wavelength and the structural parameters are fixed, and the propagation direction (or spatial frequency) of the beam is changed.

1.7.4 Photonic bandgaps and Bloch waves

The discrete waveguiding model based on Eq. (1.11) succesfully describes phenomena such as discrete diffraction and discrete self-trapping, but its validity is limited to the regime of weak coupling and does not offer a comprehensive description of the effects of Bragg reflection. For a more complete understanding of linear and nonlinear wave propagation in periodic media, it is necessary to resort to a more general model based on the *continuous* description provided by the general wave equation (1.7).

In this case, periodicity can be accounted for by including a continuous refractive index modulation $n(x)$ in the wave equation. As dicussed in Section 1.2.6 a spatially varying linear refractive index $n(x)$ can be incorporated in the last term of the nonlinear Schrödinger equation (1.8). The function $n(x)$ is periodic such that $n(x) = n(x \pm pd)$, where p is an integer. Often the refractive index modulation can be well described by a cosine profile [cf. Fig 1.7(b)]

$$n(x) = n_0 + \frac{\Delta n}{2}\cos(2\pi x/d), \tag{1.14}$$

where n_0 is the average refractive index, Δn is the depth of the modulation, and it is assumed that $\Delta n \ll n_0$.

In the framework of the continuous model, beam propagation is governed by the properties of the spatially extended linear eigenmodes of the wave equation, and in particular the relationship between the propagation constant β and the transverse wave vector κ of these eigenmodes. The function $\beta(\kappa)$ is the linear dispersion

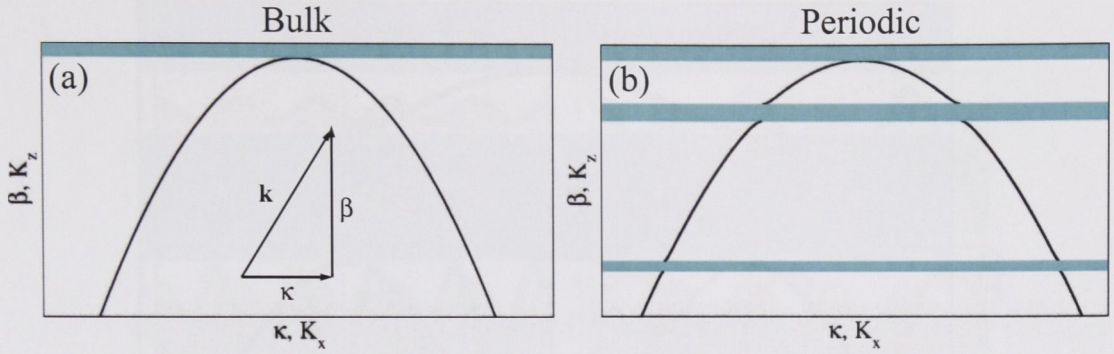

Figure 1.9: Linear diffraction relation $\beta(\kappa)$ for waves propagating in (a) a bulk medium and (b) a one-dimensional periodic structure. β is the propagation constant, and κ the transverse wave vector. The gaps appearing in (b) correspond to regions of resonant Bragg reflection where propagation at certain angles is prohibited.

relation which, for the purpose considered here, may be termed the linear *diffraction relation*. To understand the effects of Bragg reflection it is useful to consider how, compared to the case of bulk media, $\beta(\kappa)$ is modified in a periodic structure.

In homogeneous bulk media the linear eigenmode solutions to the wave equation (1.7) are the well known plane waves $E(\mathbf{r}) = E_0 \exp(i\mathbf{k} \cdot \mathbf{r})$ where in the case of only one transverse dimension $\mathbf{r} = (x, 0, z)$, $\mathbf{k} = (k_x, 0, k_z)$, and $|\mathbf{k}| = k = n_0 k_0 = 2\pi n/\lambda$. The relationship $k^2 = \kappa^2 + \beta^2$ determines the diffraction relation $\beta = \sqrt{k^2 + \kappa^2}$. That is, in this case κ and β are simply the x and z components of the constant plane wave vector $\mathbf{k}$. In the paraxial approximation where $\kappa \ll k$ the diffraction relation becomes $\beta = k - \kappa^2/2k$. This parabolic relationship is sketched in Fig. 1.9(a). To each point along the diffraction curve corresponds a plane wave solution whose $\mathbf{k}$-vector and propagation direction point along the normal to the curve.

In periodic media, no wave propagation is possible in the directions where strong Bragg reflections occur [Eq. (1.13)], and this leads to the appearence of *gaps* in the linear diffraction relation $\beta(\kappa)$ at $\kappa = \pm m\pi/d$. Figure 1.9(b) shows the modified diffraction relation (solid black) and the corresponding gaps (shaded) for a one-dimensional periodic structure. As a result of Bragg reflections the diffraction curve is divided into separate transmission *bands* which are numbered in succesive order from the top of the diagram. In Fig. 1.9(b) the first two bands and Bragg reflection gaps (or bandgaps) are visible, as well as part of the third band. The semi-infinite gap at the top of the first band is known as the *total internal reflection gap*, which is also present in the bulk medium [cf. Fig. 1.9(a)]. Note that higher order Bragg reflections ($m \geq 2$) are weaker than in the first order ($m = 1$), and that correspondingly the bandgap width succesively decreases for higher orders. Also, the strength, or spectral width, of the Bragg reflection depends on the depth of the refractive index modulation, so that higher Δn leads to wider bandgaps and

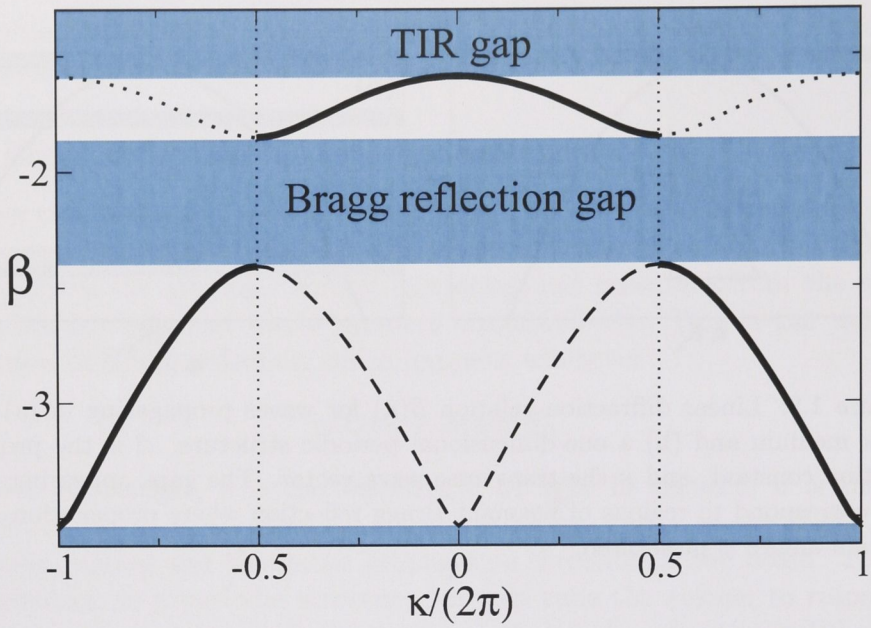

Figure 1.10: The periodic linear diffraction relation $\beta(\kappa) = \beta(\kappa \pm p2\pi)$ for waves propagating in a one-dimensional periodic structure. The diagram shows the total internal reflection (TIR) gap, the first Bragg reflection gap (both shaded), and the first and second transmission bands (solid black curves). All bands can be represented within the first Brillouin zone $-\pi < \kappa < \pi$ (dashed black curve for the second band). Ordinate units are arbitrary.

narrower bands [cf. Section 2.6.1].

In periodic media the linear eigenmodes are the optical Bloch waves (or Floquet-Bloch waves) which are the solutions to the linearised wave equation in the presence of a periodic refractive index modulation [Eq. (1.14)] [14]. Like plane waves the Bloch eigenmodes extend to infinity in space, and any beam propagating in the periodic structure can be decomposed into a superposition of Bloch waves. To each point along the linear dispersion curves [Fig. 1.9(b)] corresponds a particular Bloch wave solution,

$$\psi_{\kappa_n,\beta_n}(x,z) = u_{\kappa_n,\beta_n}(x)\exp(i\kappa x + i\beta z), \tag{1.15}$$

where $u_{\kappa_n,\beta_n}(x) = u_{\kappa_n,\beta_n}(x+d)$ is a periodic function with the same periodicity as the lattice, and the index $n = 1, 2$, etc. denotes the band number. The Bloch waves represent plane waves modulated by periodic functions, which in general are complex and have a complicated mode structure. The theory of optical Bloch waves makes use of the Bloch theorem in analogy with the description of charged particles (electrons) in periodic electronic potentials. Much of the theoretical tools and terminology including the band structure representation with bandgaps etc. is thus borrowed from the field of solid state physics [11, 14]. The linear diffraction

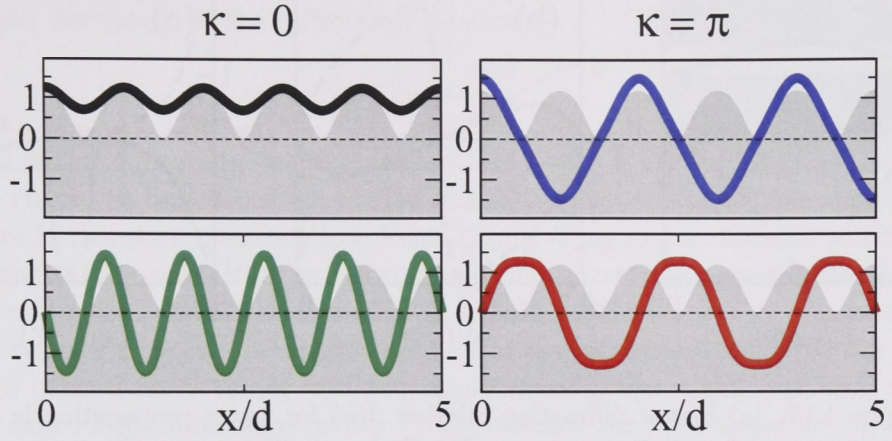

Figure 1.11: Amplitude profiles of Bloch waves associated with the edges of the first band (top) and the second band (bottom), at $\kappa = 0$ (left) and $\kappa = \pm\pi$ (right). Grey shading indicates the corresponding refractive index profile.

relation for each transmission band is periodic in k-space as shown in Fig. 1.10. Notice that in Fig. 1.10 and hereforth we normalise the transverse wave vector to the lattice period $\kappa \rightarrow \kappa d$ such that $\kappa = \pm m\pi$ defines the Bragg reflection points in the band diagram. The diffraction relation for periodic systems is commonly represented entirely within the first Brillouin zone ($-\pi < \kappa < \pi$) as marked by vertical dotted lines in Fig. 1.10. The higher order bands which lie beyond the first Bragg reflection gap are *folded* back into the first Brillouin zone and appear in succesive order with decreasing propagation constant below the first band. In Fig. 1.10 the second band is thus fully represented by the dashed black line in the region $-\pi < \kappa < \pi$.

Figure 1.11(a) shows the transverse Bloch wave profiles associated with the four edges of the first and the second band (at $\kappa = 0$ and $\kappa = \pm\pi$). At these spectral points the Bloch wave amplitude components are either purely real or imaginary, leading to modes with simple uniform or staggered phase structure. In Fig. 1.11 grey shading indicates the cosine shaped refractive index modulation. The Bloch wave profile at the top of the first band [Fig. 1.11, black] takes the form of a modulated plane wave, oscillating about a nonzero mean value with constant phase. The Bloch wave profiles at the edges of the Bragg reflection gaps, on the other hand, oscillate about zero with a staggered phase structure (π phase jump between adjacent peaks) [Fig. 1.11, blue, red, green]. At the bottom of the first band (blue) and the top of the second band (red) the amplitude peaks are aligned with the refractive index maxima and minima, respectively. At the bottom of the second band (green) the Bloch wave oscillation period is halfed, and the amplitude peaks are positioned on the slopes of the refractive index modulation.

Clearly the type of optical beams associated with Bloch waves in the second band [Fig. 1.11, red, green], which have their amplitude and intensity maxima

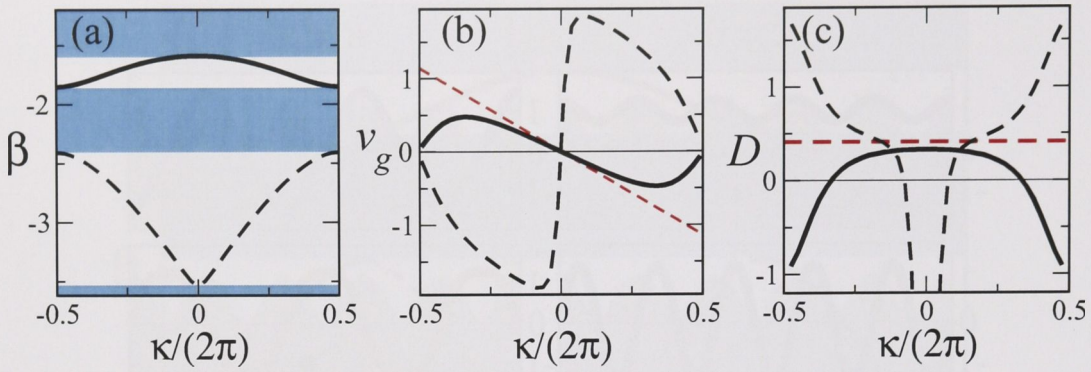

Figure 1.12: (a) Linear diffraction relation $\beta(\kappa)$ for waves propagating in a one-dimensional periodic structure. (b) Corresponding group velocity $v_g = \partial\beta/\partial\kappa$ and (c) diffraction coefficient $D = -\partial^2\beta/\partial\kappa^2$, for the first band (solid black), the second band (dashed black) and, for comparison, a bulk medium (dashed red). All ordinate units are arbitrary.

located outside the high index regions, cannot exist in the framework of the simple discrete waveguiding picture presented in Section 1.7.2, where light is expected to concentrate in the areas of high refractive index, and never between lattice sites.

1.7.5 Diffraction management

The linear diffraction relation $\beta(\kappa)$ determines how optical beams propagate and diffract in bulk and periodic media. The strong modification of $\beta(\kappa)$ and its derivatives caused by the effect of Bragg reflection are an indication of the wealth of unique opportunities for beam control offered by periodic structures [Fig. 1.12]. The group velocity v_g,

$$v_g = \frac{\partial\beta}{\partial\kappa}, \tag{1.16}$$

is directly related to the propagation direction of a wave associated with a narrow spectral region of the diffraction curve. Waves propagate along the normal to the slope of the dispersion curve at any given point, and the propagation angle with respect to the z axis is $\theta = \tan^{-1}(v_g)$. In periodic media beams centered at either $\kappa = 0$ or $\kappa = \pm\pi$ propagate straight along the lattice with zero transverse velocity because $\partial\beta/\partial\kappa = 0$ at the bandedges [see Fig. 1.12(b)]. In a bulk medium, on the other hand, beams propagate straight only for $\kappa = 0$.

Spatially finite beams are composed of a continuum of Bloch waves from within a certain spectral range $\Delta\kappa$ and $\Delta\beta$ along the diffraction curve. Linear diffraction broadening occurs as a result of the divergence in the group velocity [Eq. (1.16)] within the spectral extent of a finite beam. Diffraction is therefore characterised by

the second derivative of the diffraction relation,

$$D = -\frac{\partial^2 \beta}{\partial \kappa^2}, \tag{1.17}$$

where D is the *diffraction coefficient* associated with a particular point on the diffraction curve. In bulk isotropic media, the dispersion relation is parabolic and its curvature is therefore constant [see Fig.1.12(c)]. This means that an optical beam will diffract at the same rate no matter in which direction it propagates (for symmetry reasons this should be expected in a bulk medium). Furthermore, since the band curvature $\partial^2\beta/\partial\kappa^2$ is negative, spectral components located to the right of a beam's central wave vector will propagate more to the right, and vice versa on the left side. The minus sign in Eq. (1.17) ensures that the negative curvature of the diffraction relation in a bulk medium is associated with a *positive* diffraction coefficient ($D > 0$).

In periodic systems, the picture is dramatically different and beam diffraction exhibits a lot more variation than in the bulk case. A most peculiar effect of periodicity is the possibility of observing *anomalous* ($D < 0$) or *zero* ($D = 0$) beam diffraction, two effects that never occur in bulk media where $D > 0$ and diffraction is always *normal* (hence the name). Figure 1.12(c) reveals that in a periodic structure the value of the diffraction coefficient varies greatly as the transverse wave vector κ is scanned across the Brillouin zone, both in the first (solid black) and second (dashed black) bands, whereas D is constant in a bulk medium (dashed red).

The diffraction coefficient is strongly increased near all Bragg reflection gap edges, i.e. at $\kappa = \pm\pi$ for the first band, and at $\kappa = 0$ and $\kappa = \pm\pi$ for the second band [Fig. 1.12(c)]. This is a direct consequence of the appearence of bandgaps which locally modify and increase the band curvature near the gap edges [Fig. 1.12(a)]. In particular, the band curvature is inverted at the bottom of the bands, leading to the effect of anomalous diffraction near $\kappa = \pm\pi$ in the first band and $\kappa = 0$ in the second band [see Fig. 1.12(c)]. In regions of anomalous diffraction, the spectral components located to the right of a beam's central wave vector will propagate more to the left, and vice versa on the left side. On the other hand, the departure from bulk diffraction is relatively small at the top of the first band, near $\kappa = 0$ in Fig. 1.12(c).

Anomalous diffraction has interesting consequences for beam propagation in the nonlinear regime, and in structures with a broken lattice symmetry [see Section 1.8 and Chapter 2]. Between the regions of normal ($D > 0$) and anomalous ($D < 0$) diffraction, within each band, a region of *zero* diffraction exists where $D = 0$, corresponding to a locally linear dispersion relation. Intriguingly, a beam which is spectrally confined within this region will experience no linear diffraction broadening upon propagation.

1.8 Discrete and gap solitons

Section 1.6 discussed how self-focusing nonlinearity can balance beam diffraction and lead to the formation of bright spatial solitons in bulk media. In this case the

propagating beam effectively induces its own waveguide in a uniform background through the effect of self-phase modulation [Fig. 1.5(b)]. In the framework of the linear diffraction relation [Fig. 1.9(a)] such soliton formation can be seen as the result of nonlinearly *increasing* the propagation constant β, and thereby shifting it up into the total internal reflection gap at $\kappa = 0$. Inside the semi-infinite gap the beam is decoupled from the waves associated with the linear diffraction curve, and it propagates without diffraction in the form of a soliton. It is clear from this picture that in a bulk medium beam self-trapping can occur only when nonlinearity acts as to increase the refractive index and correspondingly the propagation constant β. Self-defocusing nonlinearity on the other hand *decreases* the refractive index and pushes β downwards, which leads to increased beam spreading or *self-defocusing* (hence the name).

Similar to bulk media, periodic structures allow for beam self-trapping to occur for self-focusing nonlinearity in the total internal reflection gap in the form of *discrete solitons*. This process is indicated by the black arrow at the top of the first band in Fig. 1.13(a). In addition, periodicity introduces the unique possibility of realising self-trapping in the Bragg reflection bandgaps in the form of *gap solitons*, for either self-focusing nonlinearity in regions of *normal* diffraction, or self-defocusing nonlinearity in regions of *anomalous* diffraction. In the former case, gap localisation can be achieved by shifting β upwards from the lower edges of the Bragg reflection gaps, e.g. at $\kappa = \pm\pi$ in the second band [Fig. 1.13(a)]. In the latter case gap localisation occurs when β is shifted downwards from the upper gap edges, e.g. at $\kappa = \pm\pi$ in the first band and $\kappa = 0$ in the second band [Fig. 1.13(b)].

In all cases the modal characteristics of the Bloch waves associated with the respective band edges [see Fig. 1.11] are preserved by the self-trapped waves inside the gaps. This is illustrated in Fig. 1.13(c) which shows the profiles of self-trapped waves originating from the first band (top row) and second band (bottom row), for self-focusing (left) and self-defocusing (right) nonlinearity. In Fig. 1.13(c) grey shading marks the positions of the high refractive index regions in the lattice.

The discrete waveguiding model described in Section 1.7.2 predicted two different self-trapping scenarios for self-focusing and self-defocusing nonlinearities, leading to in-phase [Fig. 1.8(c)] and out-of-phase [Fig. 1.8(d)] solutions, respectively. It is now clear that in the framework of continuous wave theory, the first case corresponds to self-trapping inside the total internal reflection gap of the in-phase (unstaggered) beam associated with the Bloch wave at the top of the first band [Fig. 1.13(c), top left], and that the second case corresponds to self-trapping inside the first Bragg reflection gap of the out-of-phase (staggered) beam associated with the Bloch wave at the bottom of the first band [Fig. 1.13(c), top right].

On the other hand, the existence of higher order gap solitons originating from the edges of the second band [Fig. 1.13(c), bottom left and right] is not accounted for by the discrete model. In the discrete waveguiding picture light is expected to concentrate in the areas of high refractive index, and never between lattice sites. The Bloch waves [Fig. 1.11, bottom left and right] and corresponding solitons [Fig. 1.13(c), bottom left and right] associated with the second band have their amplitude and intensity maxima located outside the high index regions of the lattice, and therefore

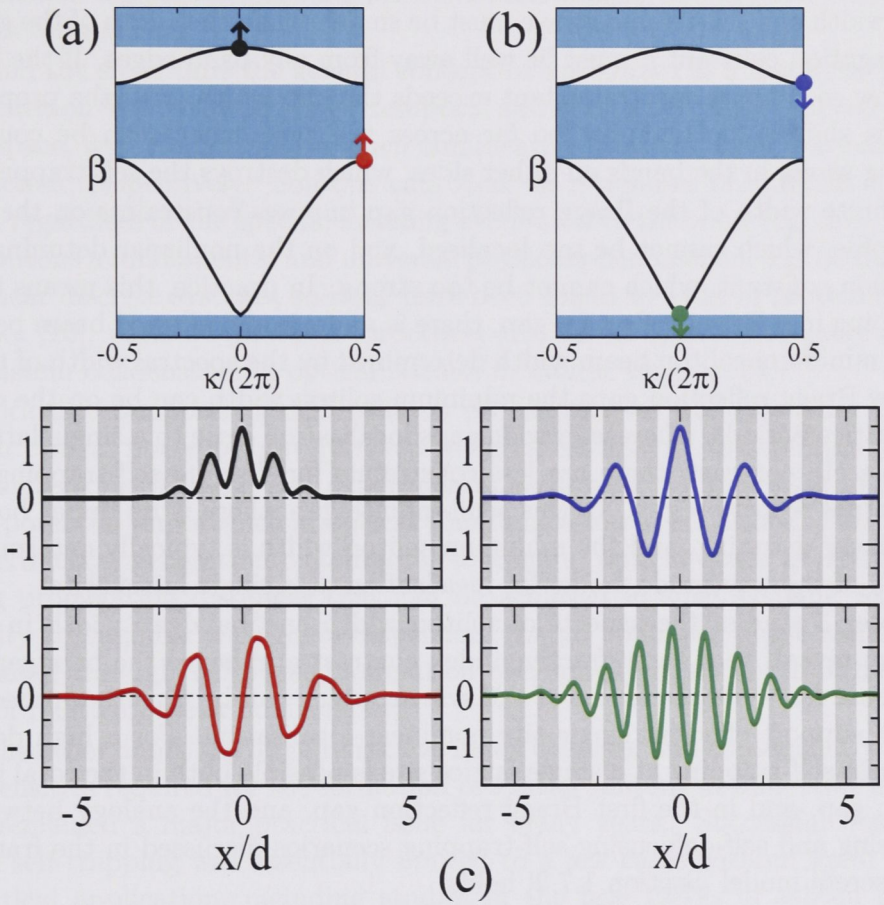

Figure 1.13: (a,b) Self-trapping in one-dimensional photonic lattices for (a) self-focusing and (b) self-defocusing nonlinearity. The arrows indicate the corresponding (a) increase and (b) decrease of the propagation constant β. (c) Schematic amplitude profiles of self-trapped waves originating from the edges of the first band (top row) and the second band (bottom row), at $\kappa = 0$ (left) and $\kappa = \pm\pi$ (right), corresponding to the points marked in (a,b). Grey shading in (c) indicates the high refractive index regions of the lattice.

cannot exist in the framework of the discrete waveguiding model.

The different physical origins of the total internal reflection gap and the Bragg reflection gaps lead to some fundamental differences with respect to the effect of self-trapping in the respective gaps. The total internal reflection gap is semi-infinite whereas the Bragg reflection gaps have a finite width (which decreases with the gap order). In order to be fully contained within a finite Bragg reflection gap, the spectral width of a self-trapped wave must be smaller than the width of the gap, and the propagation constant β must lie well away from any band edges. If the beam is too narrow so that its spectral extent exceeds the gap width, or if the propagation contant is shifted too little or too far across the gap, energy can be coupled to diffracting waves in the bands on either sides, which destroys the self-trapped state.

The finite width of the Bragg reflection gap imposes constraints on the spatial beam profile, which cannot be too localised, and on the nonlinear detuning of the propagation constant, which cannot be too strong. In practice, this means that for self-trapping in a Bragg reflection gap, there is a maximum allowed beam power, as well as a minimum soliton beam width determined by the spectral width of the gap. In narrow Bragg reflection gaps the minimum soliton width can be on the order of several lattice periods, whereas in wide gaps localisation close to a single lattice site is possible. In contrast, there are less constraints for discrete self-trapping in the total internal reflection gap. In this semi-infinite gap, there is no upper bound on the nonlinear detuning, and the minimum soliton width is typically determined by the width of the waveguide mode, for localisation at a single lattice site.

Chapter 3 studies the aspects of soliton width and bandgap width in further detail and reveals that the refractive index contrast and hence the bandgap width is a measure for the discreteness of the system which can be directly probed by its ability to support effecient single site nonlinear localisation. For a high degree of discreteness self-trapping at a single lattice site is possible both in the total internal reflection gap, and in the first Bragg reflection gap, and the analogy between the self-focusing and self-defocusing self-trapping scenarios discussed in the framework of the discrete model [Section 1.7.2] holds.

1.9 Historical perspectives

This Section aims at providing a brief summary of the background and early studies of beam self-trapping in nonlinear periodic photonic structures. Focusing on experimental work in the field, this short review provides some of the historical context and motivation for the research carried out in this thesis.

The first numerical study of nonlinear dynamics in discrete systems was performed by Fermi, Pasta, and Ulam in 1953. Their famous and pioneering work [15] considered the evolution of localised excitations in a discrete chain of anharmonic oscillators, representing nonlinearly coupled modes of a vibrating string. The dynamics of the coupling and energy distribution between different modes proved far more rich and complex than expected. As a result, the study sparked an intense interest in the dynamics of nonlinear discrete systems across several fields of physics.

Meanwhile the experimental study of self-trapping of light in bulk optical media was made possible by the invention of the laser and hence the access to high optical intensities and strong nonlinearity. Some of the first experimental evidence of beam self-trapping was reported as early as 1964 [16] in the form of filament damage in glass induced by an intense focused laser beam. Subsequent theoretical studies [17, 18] established the theoretical basis for the understanding of nonlinear self-trapping of light in bulk media.

Around the same time the general concept of the *soliton* as a nonlinear localised wave excitation was developed [19]. Temporal and spatial solitons, localised in either time or space, were found to form when nonlinearity balances linear wave dispersion or diffraction, respectively. Solitons can occur in a number of different nonlinear systems, regardless of the specific meaning attributed to the wave function, and this makes solitons a fundamental and universal physical phenomenon. In the framework of nonlinear discrete systems, solitons have been found to exist in protein chains in biophysics [20], periodic photonic structures [10, 12] in optics, and more recently, Bose-Einstein condensates in optical lattices in atomic physics [21].

Historically, temporal optical solitons propagating as nondispersing pulses in nonlinear optical fibers [5] have received the greatest amount of attention following their discovery in 1973 [22] and experimental verification in 1980 [23], in part due to their potential importance in optical communication applications. Furthermore, the experimental generation of temporal solitons in optical fibers is facilitated by the long propagation distances that can be achieved in such systems, as well as the ability to engineer waveguide dispersion. Large nonlinear phase shifts can be accumulated through self-phase modulation over an extended length of fiber, even in case of relatively weak nonlinearity.

On the other hand, the large refractive index changes, and consequently the high power densities required for the formation of spatial solitons in bulk Kerr nonlinear media, remained a major practical issue for many years. Successful observation of beam self-trapping was essentially limited to a few cases without great promise for practical application, including studies in the late 1980's of soliton propagation in highly nonlinear liquids [24, 25] and later on in silica glass [26]. Elliptical stripe beams [24] or slab waveguides [25, 26] were used to achieve an effective one-dimensional transverse geometry necessary for stable soliton propagation in bulk media [4], and both cases employed pulsed lasers with high peak power to achieve a sufficiently large nonlinear response.

In 1992 [27] it was suggested that the photorefractive nonlinearity [cf. Section 1.3] could be used to achieve beam self-trapping in bulk structures at much lower laser powers (microwatts) than required by the Kerr nonlinearity, making the use of continuous-wave lasers feasible in such experiments. This approach considerably widened the perspectives and opportunities for experimental research on spatial solitons [28]. Soon after, photorefractive self-trapping of light was observed experimentally [29, 30], and a number of different experimental settings were subsequently proposed and studied in detail [7, 8, 31], including solitons supported by screening nonlinearity in the presence of an external applied field [7] (as discussed in Section 1.3.1), and solitons in photovoltaic photorefractive media such as lithium

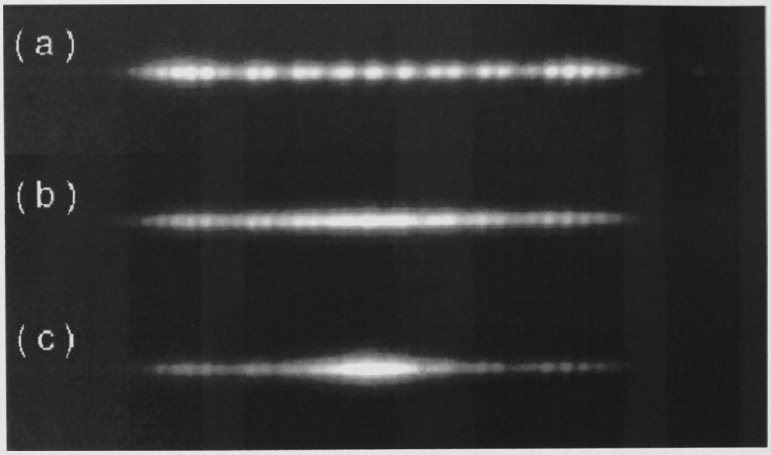

Figure 1.14: Pictures of the first experimental observation of a discrete soliton in an AlGaAs waveguide array (from Ref. [33]). (a) Discrete diffraction at low power; (b) partial self-trapping at intermediate power; (c) formation of discrete soliton at high power.

niobate [31].

Self-trapping of light in one-dimensional periodic structures was predicted in 1988 by Christodoulides and Joseph [12], who showed the possible existence of *discrete solitons* in extended planar arrays of coupled waveguides. Such structures represent the generalisation of the nonlinear directional coupler [32], and the optical analog of discrete atomic chains studied previously in e.g. biophysics [20]. A decade later the first experimental observation of one-dimensional discrete solitons was reported [33]. In this milestone experiment, the Kerr nonlinearity was used to achieve self-trapping of high peak power ($\sim$ 1kW) femtosecond laser pulses in planar AlGaAs waveguide arrays (see Fig. 1.14).

An important motivation for the study of nonlinear beam propagation in discrete optical media was that the linear diffraction can be modified and controlled by the strength of coupling between neighboring waveguides, resulting in lower power requirements for soliton formation. The use of periodic structures thus allowed for overcoming one of the fundamental limitiations encountered in bulk media, where diffraction can not easily be engineered. In addition, periodicity and discreteness increase the diversity of spatial nonlinear effects, e.g. by allowing for self-trapping in the form of out-of-phase solitons in self-defocusing media [13] [cf. Section 1.8].

In the years following the first observation of discrete solitons [33] a series of detailed experimental studies of discrete soliton dynamics [34] as well as linear diffraction management [35, 36], and discrete self-focusing and self-defocusing [37], were performed in planar self-focusing waveguide arrays. Pointing towards applications of the fundamental effects, novel possibilities for nonlinear beam steering and switching based on discrete periodic structures were extensively investigated in theoretical works [38–42], although experimental studies of such linear and nonlinear

effects were limited at this point in history [34, 43, 44].

The excitation of Bloch waves from higher order transmission bands demonstrated experimentally in 2003 [45] represented one of the next major steps forward, leading to the first observations of spatial *gap solitons* originating from the top of the second band [45–47]. Whereas all discrete solitons observed thus far had resided in the total internal reflection gap, as in the case of bulk solitons, gap solitons were found to be localised inside the Bragg reflection bandgap, therefore representing a phenomenon truly unique to periodic systems. Furthermore, nonlinear beam localisation in photonic bandgaps highlighted important links between spatial solitons in periodic structures and light confinement in photonic crystal structures [48–53], and temporal gap solitons [54–56] observed in nonlinear fiber Bragg gratings [57–59]. The observation of gap solitons in Bose-Einstein condensates [21] in 2004 further broadened the scientific scope and potential impact of studies of light propagation in nonlinear periodic systems. As a consequence, the observation of higher order Bloch waves and gap solitons [45–47] represented an important new development leading to enhanced research opportunities in discrete nonlinear optics.

Initially experimental works in the field had concentrated on the use of planar waveguide arrays. In 2002 Efremidis *et al.* suggested that discrete solitons could also exist in *optically induced* photonic lattices created by interference of ordinarily polarised coherent plane waves in biased photorefractive crystals such as strontium barium niobate (SBN) [60]. This novel approach offered a number of distinctive advantages: (i) higher dimensional periodic structures (e.g. square and triangular lattices) can be realised by interefering three or more plane waves; (ii) the induced structures are reconfigurable and dynamically tunable; and (iii) self-trapping can be observed at moderate (cw) laser powers due to the strong photorefractive nonlinearity.

The price paid for the increased flexibility and new opportunities was a complex and bulky experimental setup involving interferometric components and many external real-time parameters, as well as a slow nonlinear response on the order of seconds. However, optically induced lattices soon proved to be an ideal, versatile testbed for problems in discrete nonlinear optics, and since their introduction many fundamental effects were demonstrated, including discrete [61–63] and gap [47, 61, 64] solitons in one-dimensional [47, 61, 62] and two-dimensional [63, 64] lattices.

In addition to planar Kerr waveguide arrays and optically induced lattices, several other experimental platforms were suggested and found applicable in the study of discrete nonlinear light propagation, including one-dimensional waveguide arrays in nematic liquid crystal cells with patterned electrodes [65, 66], planar waveguide arrays with quadratic nonlinearity [67–69], and photonic lattices created by femtosecond laser writing in bulk glass [70–72]. The wide range of experimental realisations and studies of nonlinear periodic structures, as well as the rich physics associated with beam propagation in such systems, have resulted in a very active research field, which encompasses both studies of fundamental effects, and efforts oriented towards the application of nonlinear periodic structures in e.g. all-optical systems and active devices.

1.10 Scope and outline of the thesis

The nonlinear effects that can be observed in periodic structures strongly depend on available experimental platforms, and are often restricted by e.g. large optical power requirements, limited propagation distances, fabrication or stability issues, or structural irregularity. Trade-offs between system-specific advantages and drawbacks have to be considered in each experimental study. For example, early attempts to realise two-dimensional periodic photonic lattices based on multicore silica fibers [73] demonstrated the important role of fundamental technical fabrication challenges and tolerances, and the need to continuously consider alternative experimental schemes for the study of the interplay between periodicity and nonlinearity.

The development of new ideas and the discovery of new physical effects go hand in hand with the development of new experimental settings, which again rely increasingly on the advances in microfabrication technology. At the start of this thesis a solid experimental basis had already been established in the field of nonlinear beam propagation in discrete periodic structures [10]. Relevant research challenges therefore included: (i) the demonstration and detailed study of novel effects, reaching beyond the results of the first pioneering studies in the field, and (ii) the development of new experimental platforms allowing for further progress, in particular towards the application of fundamental effects in microphotonic devices.

The aim of the research carried out in this work is therefore two-fold. First, we use an established experimental platform, namely optically induced lattices in SBN crystals, for carrying out elaborate studies of beam propagation in nonlinear periodic structures, exploring complex nonlinear beam interactions, and new lattice configurations and geometries. Then we study new opportunities offered by high quality *fabricated* photonic microstructures. We demonstrate discrete self-trapping of light in waveguide systems based on planar $LiNbO_3$ wafers, and develop a novel experimental platform for discrete nonlinear optics based on two-dimensional tunable lattices in microstructured fibers infiltrated with nonlinear liquids.

The structure of the thesis and the relation between the researched areas, with respect to the involved lattices geometries and types of nonlinearity, are shown graphically in Fig. 1.15. The diagram illustrates the progression from optically induced lattices with self-focusing nonlinearity [Fig. 1.15(a,c)] to fabricated photonic structures with self-defocusing nonlinearity [Fig. 1.15(b,d)], and from one-dimensional systems [Fig. 1.15(a,b)] to two-dimensional systems [Fig. 1.15(c,d)]. In all cases we study linear and nonlinear transverse beam propagation effects associated with the interplay between periodicity and nonlinearity, focusing in particular on effects that can be used to achieve nonlinear or dynamically tunable control of the beam evolution. The introduction of compact, fabricated periodic structures such as waveguide arrays [Fig. 1.15(b)] and microstructured optical fibers [Fig. 1.15(d)] represents an important step from fundamental research in the field towards the implementation of demonstrated effects in applications in e.g. integrated microphotonic systems.

The work described in Chapter 2 represents an extension to the first pioneering experiments on linear and nonlinear light propagation in one-dimensional optically

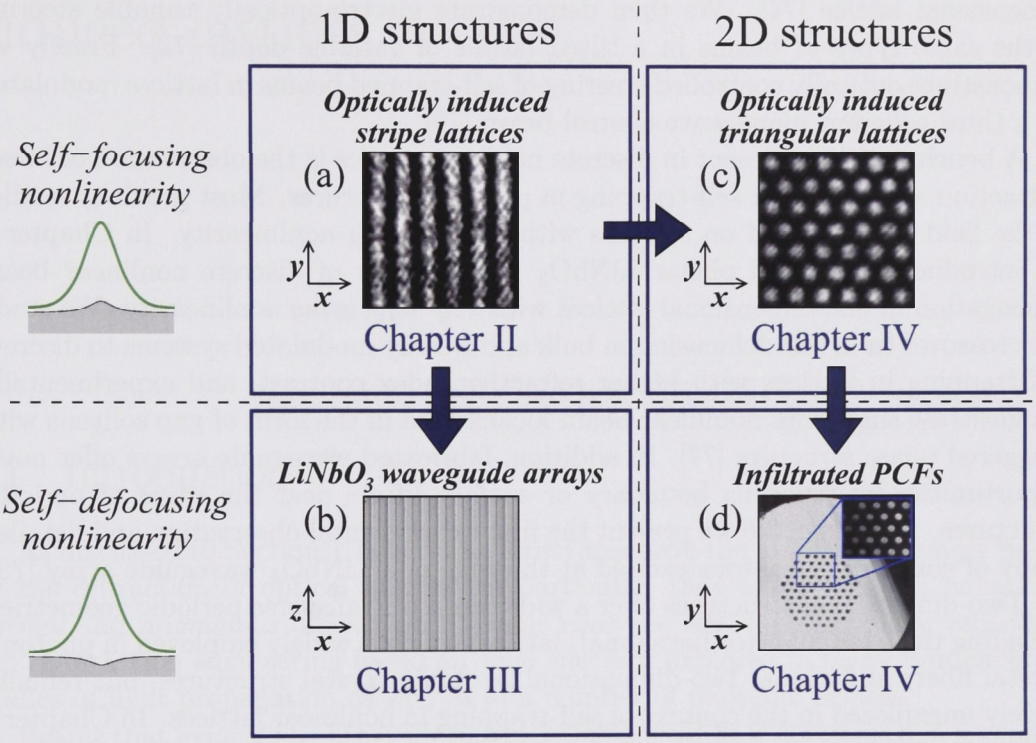

Figure 1.15: Graphical overview of the structure of the thesis, and the relation between individual research topics. The investigated experimental systems are (a) one-dimensional optically induced lattices (Refs. [74–76]); (b) planar $LiNbO_3$ waveguide arrays (Refs. [77, 78]); (c) triangular optically induced lattices (Ref. [79]); and (d) infiltrated photonic crystal fibers (PCFs) (Ref. [80]). The work covers studies of beam propagation in one-dimensional (1D) and two-dimensional (2D) periodic structures (left and right column), with self-focusing and self-defocusing nonlinearity (top and bottom row). The large arrows indicate the progression from (i) optically induced to fabricated photonic structures (vertical direction), and (ii) one-dimensional to two-dimensional lattice geometries (horizontal direction).

induced lattices in photorefractive crystals [47, 61, 62]. We employ a flexible and reconfigurable setup to study a range of novel effects aimed at tunable and nonlinear spatial beam control in one-dimensional photonic lattices. In particular we focus on demonstrating experimental schemes with potential in dynamic *beam manipulation* and *beam steering*. We study effects resulting from nonlinear interaction of beams associated with the edges of the first and second transmission bands of a one-dimensional lattice [74]. We then demonstrate electro-optically tunable steering of the same types of beams in a tilted lattice of variable depth [75]. Finally we demonstrate optically controlled steering of self-trapped beams in lattices modulated by a third coherent plane wave control beam [76].

A benchmark experiment in discrete nonlinear optics is the observation of linear diffraction and nonlinear self-trapping in periodic structures. Most previous studies in the field have focused on systems with self-focusing nonlinearity. In Chapter 3 we introduce the use of planar $LiNbO_3$ in the study of discrete nonlinear beam propagation in one-dimensional lattices with *self-defocusing* nonlinearity. We study the crossover from self-defocusing in bulk and weakly modulated systems to discrete self-trapping in lattices with higher refractive index contrast, and experimentally demonstrate single-site nonlinear beam localisation in the form of gap solitons with staggered phase structure [77]. In addition, fabricated waveguide arrays offer novel opportunities for studying boundary or *surface* effects near the edges of periodic structures. In Section 3.6 we present the first experimental observation and detailed study of surface gap solitons excited at the edge of a $LiNbO_3$ waveguide array [78].

Two-dimensional structures offer a wide range of transverse periodic geometries, including the triangular (or hexagonal) lattice, which is widely employed in photonic crystal fibers and planar two-dimensional photonic crystal structures, but remains largely unexplored in the context of self-trapping in nonlinear lattices. In Chapter 4 we study the fundamental effect of self-trapping in triangular optically induced lattices created by three wave interference in a biased SBN crystal. Self-trapping of beams associated with the first and second transmission bands, in the total internal reflection and Bragg reflection gaps, respectively, is demonstrated for self-focusing nonlinearity [79]. Finally, infiltrating the cladding region of a photonic crystal fiber (PCF) and using the structure as a nonlinear triangular lattice, we experimentally demonstrate highly tunable beam diffraction and thermal self-defocusing and, based on these effects, realise a compact all-optical power limiter [80].

CHAPTER 2

Beam interaction and steering in optically induced lattices

2.1 Introduction

As discussed in Section 1.7, periodic structures have the ability to strongly modify the diffraction of optical beams. In particular, they allow for both enhanced *normal* and *anomalous* diffraction to occur near the edges of the Bragg reflection gap. Diffraction engineering based on such effects is explored in many fundamental studies of light propagation as well as in a number of photonic devices.

Beams that experience either normal or anomalous diffraction spread in a similar manner upon linear propagation in a straight photonic lattice, despite the fundamental differences in e.g. their spatial profile. However, dramatic differences between the two regimes of diffraction manifest themselves when either nonlinearity comes into play, or when the symmetry of the lattice with respect to the direction of light propagation is broken.

This Chapter aims at exploring such interplay between nonlinearity, diffraction and lattice symmetry in one-dimensional photonic lattices. We study in detail the *nonlinear coupling* of beams associated with different Bloch waves in the first and second transmission bands (Section 2.5), their *refraction* in tilted lattices (Section 2.6), and optically controlled beam steering in *modulated* lattices (Section 2.7). We demonstrate a number of fundamental effects which are unique to systems that display nonlinearity, periodicity and tunability, and which enable novel experimental approaches to achieving dynamic spatial control of light with potential applications in all-optical switching and beam steering.

Optically induced lattices in a photorefractive strontium barium niobate (SBN) crystal are employed as the experimental platform for our studies. Because of their great flexibility, optically induced lattices represent an ideal testbed for the search for and demonstration of novel effects associated with light propagation in nonlinear periodic systems.

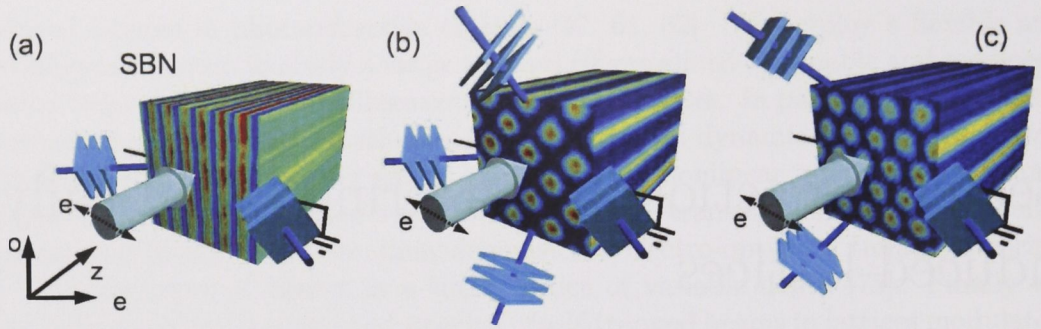

Figure 2.1: Schematic of the optical induction of (a) one-dimensional, (b) two-dimensional square, and (c) two-dimensional triangular photonic lattices by plane wave interference in a biased photorefractive crystal (SBN). Lattice beams are ordinarily polarised while probe beams are extraordinarily polarised and propagate along the longitudinal lattice direction as indicated by the arrows.

2.2 Optically induced lattices in photorefractive crystals

In 2002 Efremidis *et al.* [60] introduced the idea of using plane wave interference inside a biased photorefractive crystal to achieve reconfigurable and tunable periodic photonic structures with access to strong nonlinearity at microwatt power levels. Since its discovery the technique has proved to be extremely useful for many fundamental studies of nonlinear periodic systems, as discussed in Section 1.9.

The optical induction technique relies on the fact that photorefractive crystals such as strontium barium niobate (SBN) have highly anisotropic properties [cf. Section 1.2.2], and that in particular the electro-optic coefficient is much larger for light extraordinarily polarised along the crystalline c-axis (optic axis) than for light of the orthogonal (ordinary) polarisation [60]. In an SBN crystal biased externally along the c-axis, extraordinarily polarised light is thus subject to strong photorefractive screening nonlinearity [cf. Section 1.3.1], whereas ordinarily polarised light propagates essentially linearly at similar power levels.

The process of photo-excitation of mobile charge carriers and the generation of strong space-charge fields underlying the electro-optic refractive index modification, however, is itself independent of the light polarisation. Optical lattices created by the interference of *ordinarily* polarised plane waves (broad beams) can therefore be used to write a refractive index modulation in the photorefractive crystal without themselves being scattered by it, or subjected to strong nonlinearity. *Extraordinarily* polarised probe beams, on the other hand, will feel the induced photonic lattice, as well as a strong photorefractive screening nonlinearity.

The depth of the refractive index modulation achieved for the extraordinary polarisation is typically on the order of a few times 10^{-4} [60] which allows for many discreteness and periodicity effects to occur in optically induced lattices. Furthermore, the lattice contrast and hence the bandgap structure associated with the

periodic refractive index modulation can be varied by changing the strength of the applied bias field. Optically induced lattices are thus an example of externally *tunable* structures. The tunable lattice contrast allows for adjustment of experimental parameters for optimal performance in a given situation, or for implementing dynamic functionality such as demonstrated in Section 2.6.

Figure 2.1 shows schematically the optical induction of (a) a one-dimensional lattice, (b) a two-dimensional square lattice, and (c) a two-dimensional triangular (or hexagonal) lattice, created by the interference of two, four, and three ordinarily polarised plane waves, respectively. Probe beams are extraordinarily polarised and propagate along the lattices as indicated by the arrows in Fig. 2.1. The experiments described throughout this Chapter are concerned with linear and nonlinear beam propagation in *one-dimensional* optically induced lattices [Fig. 2.1(a)], whereas Section 4.2 in Chapter 4 is devoted to the study of the two-dimensional triangular geometry [Fig. 2.1(c)].

In addition to the plane wave interference technique employed in our experiments, nondiffracting nonlinear (solitonic) propagation of amplitude modulated, partially coherent lattice writing beams has also proven an attractive approach for realising nonlinear optically induced lattices of various geometries [63, 81–83]. This method has a number of distinctive advantages, including in particular the possibility of incorporating defects into different lattice structures [84, 85], and of studying effects arising from nonlinear interaction between lattice and probe beams [86, 87]. The stability of this type of nonlinear lattices, however, can be an issue.

2.3 Experimental setup

In our experiments we use a $15 \times 5 \times 5$ mm photorefractive $Sr_{0.6}Ba_{0.4}Nb_5O_{15}$ (SBN:60) crystal which is biased along its crystalline c-axis with a polarity resulting in a self-focusing type screening nonlinearity [7] [cf. Section 1.3.1]. In the uniaxial SBN crystal the relevant Pockels coefficients are approximately $r_{333} = 280pm/V$ for extraordinarily polarised light and $r_{113} = 13pm/V$ for ordinarily polarised light at visible wavelengths [88, 89].

A one-dimensional optically induced lattice is created inside the crystal by interfering two ordinarily polarised broad beams from a frequency-doubled Nd:YVO_4 laser at 532 nm. The beam width is on the order of several millimeters to ensure near diffractionless propagation of the lattice writing beams inside the 15 mm long crystal. The lattice is modulated in the horizontal direction, and invariantly extended in the vertical and longitudinal directions [cf. Fig. 2.1(a)]. The modulation period can be adjusted over a wide range by changing the angle between the interfering beams. In most of the experiments described here the period is 19 μm.

By varying the externally applied bias voltage (typically in the range 1.5−2.5 kV) it is possible to tune the amplitude of the refractive index modulation of the induced lattice, as well as the strength of the nonlinearity experienced by the extraordinarily polarised probe beams. The crystal is homogeneously illuminated with a variable white light source in order to control the saturation of the photorefractive nonlin-

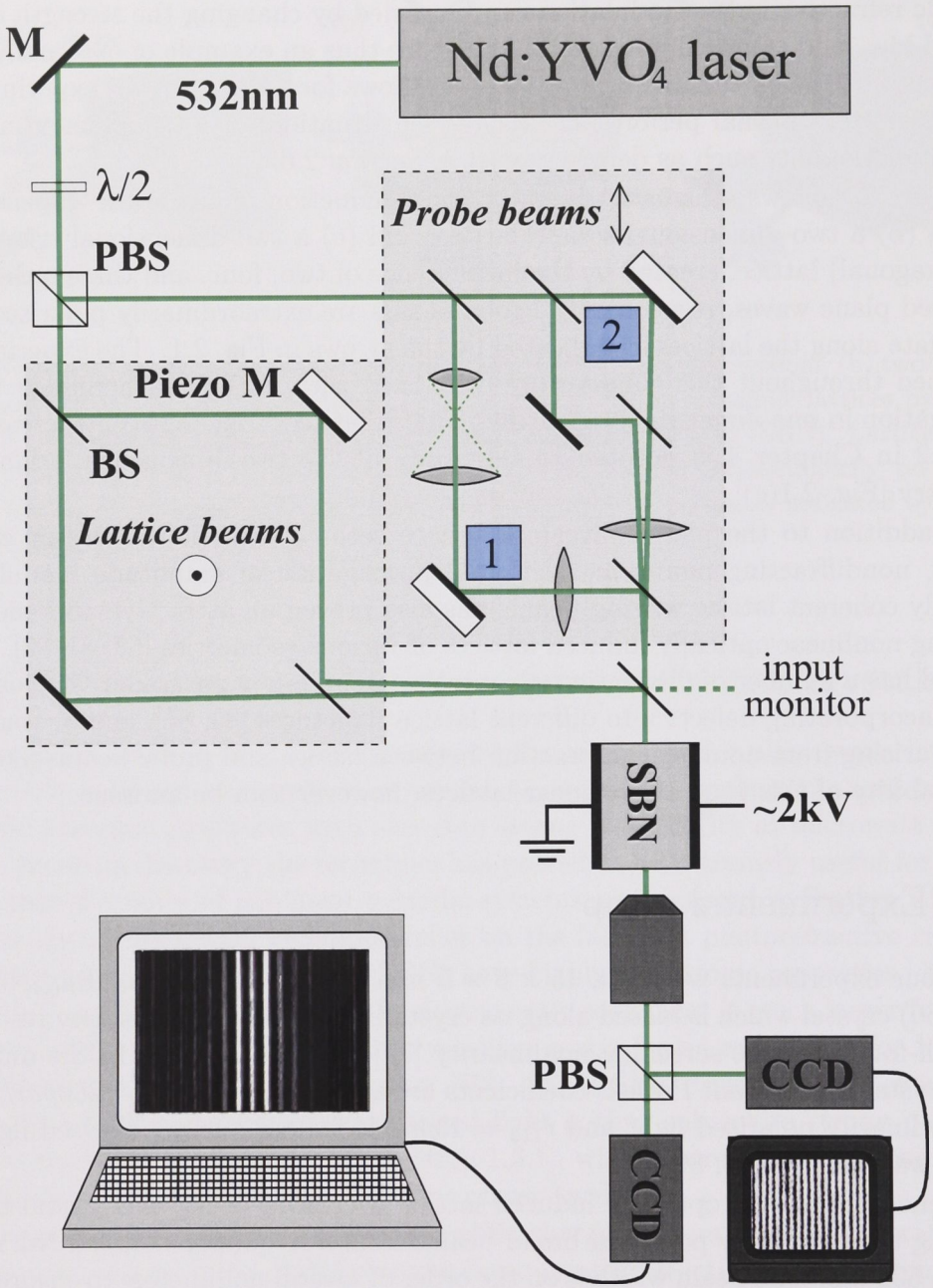

Figure 2.2: Experimental setup for the study of Bloch wave propagation in one-dimensional optically induced lattices in a photorefractive SBN:60 crystal. M – *mirror*, $\lambda/2$ – *half-wave plate*, PBS – *polarising beam splitter*, BS – *beam splitter*, Piezo M – *piezoelectrically actuated mirror*. Shaded rectangles mark the ordinarily polarised lattice beam arm (left), and extraordinarily polarised probe beam arm (right). Crystal bias voltage and background illumination are externally controlled.

earity.

A schematic illustration showing the essential features of the experimental setup is shown in Fig. 2.2. The linearly polarised cw beam emitted by the laser is attenuated and split into two arms by a polarising beam splitter (PBS) cube. The shaded rectangles outlined with dashed lines in Fig. 2.2 provide a visual distinction between the two main beam arms containing the ordinarily polarised lattice beams (left) and the extraordinarily polarised probe beams (right). A half-wave plate in front of the PBS allows for controlling the relative power carried by each of the arms, and additional half-wave plates, polarisers, and neutral density filters (not shown) allow for controlling the attenuation of all lattice and probe beams separately.

The ordinarily polarised beam is split into two individual lattice beams in a Mach-Zehnder interferometer and recombined such that they propagate through the crystal at a small angle relative to each other, which defines the transverse period of the plane wave interference pattern. The beams cross inside the crystal in order to maximise the region of overlap and hence the extent of the induced lattice. For a beam diameter of 2.5 mm and a modulation period of 19 μm, the induced lattice contains well over 100 sites.

The total power of the lattice writing beams is $0.3 - 0.6$ mW, and the relative intensity of the two beams can be adjusted. If the beams carry uneven power, the contrast of the interference fringes is reduced, resulting in a constant background illumination which provides an additional means to control the photorefractive saturation. The optical path difference and hence the relative phase between the two interfering lattice beams is controlled by reflecting one beam off a mirror which can be displaced by a piezoelectric actuator. This allows for dynamically adjusting the transverse position of the maxima of the induced refractive index modulation.

The extraordinarily polarised beam is split into two separate probe beam arms, which are used to excite different types of Bloch waves in the lattice, as described in Section 2.4 below. After passing through the crystal lattice and probe beams are separated by a polarising beam splitter cube. The intensity distributions at the crystal output face are imaged onto individual CCD cameras (Pulnix) which are interfaced to monitors and computers for data acquisition.

The input probe and lattice beams can be imaged behind the beam splitter placed immediately in front of the crystal, as indicated by the green dashed line in Fig. 2.2. This allows for monitoring the position of the probe beams and the lattice fringes at the crystal input face, even when the bias voltage is turned on and imaging through the crystal is impossible. Furthermore, rotating this beam splitter allows for controlling the tilt of the optical lattice with respect to the direction of propagation of the probe beams. These two features are important for general alignment purposes and in particular for the experiment on beam propagation in tilted lattices described in Section 2.6 below.

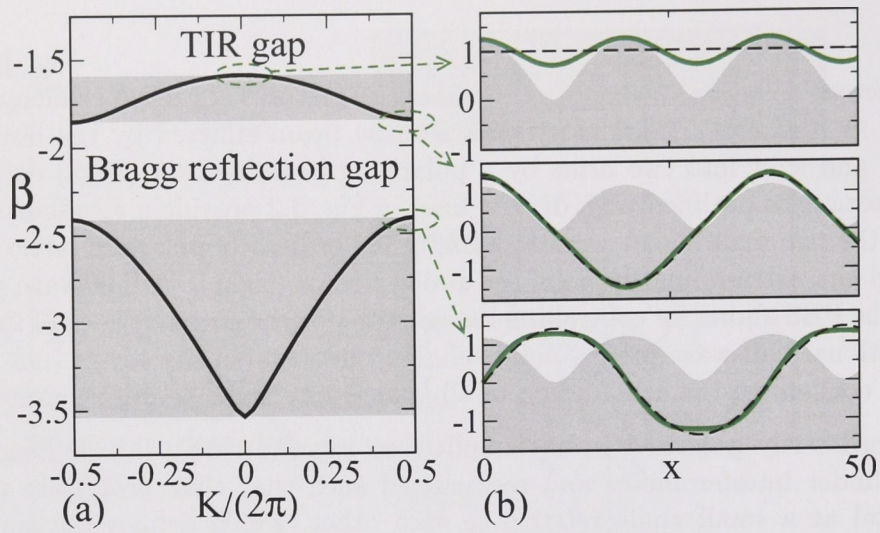

Figure 2.3: (a) Dispersion of Bloch waves in a one-dimensional optically induced lattice; the bands are shaded. (b) Bloch wave amplitude profiles at the gap edges (solid) and their leading-order Fourier components (dashed), superimposed on the normalised refractive index profile (shaded). The wavelength is $\lambda = 532$ nm, the lattice period 19 μm, the refractive index modulation 1×10^{-4}, and the normalised background and grating intensity parameters I_b and I_g are assumed to be unity.

2.4 Selective excitation of Bloch waves

In this Section we demonstrate how to experimentally generate beams with specific diffractive properties associated with different regions of the photonic bandgap diagram. As discussed in Section 1.7.4 light propagates in periodic structures in the form of Bloch waves. To experimentally study a specific point in the bandgap diagram [Fig. 1.10] energy must be selectively coupled into the Bloch wave associated with that particular spectral region. The amount of light coupled into a given Bloch wave depends on its mode field overlap with the input beam, and it is therefore important to know the exact profile of the different Bloch waves in play.

Let us consider the three regions of interest marked in Fig. 2.3(a), namely the top and bottom of the first band, and the top of the second band. Figures 2.3(a,b) show the calculated bandgap diagram along with the Bloch wave profiles at the band edges, respectively, for a typical one-dimensional optically induced lattice with a refractive index modulation of 1×10^{-4}, for the wavelength $\lambda = 0.532$ μm, and a lattice period of 19 μm. At the top of the two bands diffraction is normal, whereas at the bottom of the first band diffraction is anomalous.

The Bloch wave at the top of the first band takes the form of a modulated plane wave [Fig. 2.3(b) top], i.e. its amplitude oscillates around a nonzero value, with the period of the underlying lattice. The position of Bloch wave and index maxima

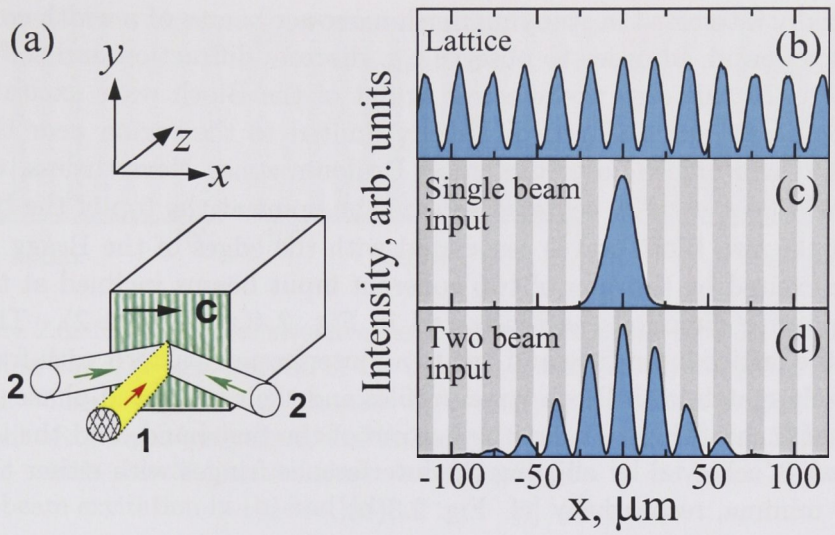

Figure 2.4: (a) Schematic of the excitation of Bloch waves with (1) a single beam and (2) a pair of beams inclined at the Bragg angle in opposite directions. (b-d) Experimental intensity profiles of (b) the optical lattice, (c) the single input beam, and (d) the two-component input beam. The lattice period is 19 μm.

coincide, and the phase is uniform like that of the plane wave. Of all Bloch waves this is the one that most resemble the plane wave eigenmode of free space and bulk media, and indeed it can be well approximated by a plane wave (its leading order Fourier component is the nonzero constant about which it oscillates) [Fig. 2.3(b) top, dashed].

The Bloch waves associated with the edges of the Bragg reflection gap have a more complex symmetry. They correspond to pairs of counterpropagating waves which are near resonant with the lattice Bragg grating. Their amplitudes oscillate around zero such that each peak is π out of phase with its neighbours, i.e. the phase structure is *staggered*. At the bottom of the first band the peaks are aligned with the index maxima of the lattice [Fig. 2.3(b), middle], whereas at the top of the second band they are aligned with the index minima [Fig. 2.3(b), bottom]. For larger index modulation the profile of the second band wave develops a double peak structure with a local minimum at the points of lowest index contrast [47] (this is not evident in the case shown in Fig. 2.3(b) bottom). To the first order, both Bloch waves at the edges of the Bragg reflection gap can be approximated by a sinusoidal field distribution aligned with either the maxima (bottom of first band) or minima (top of second band) of the refractive index modulation.

Experimentally the Bloch wave associated with the top of the first band can be excited by a single Gaussian input beam propagating straight into the lattice as illustrated in Fig. 2.4(a) (beam 1). A spectrally pure excitation of Bloch waves in principle requires broad input beams extending over many lattice periods. However,

we are typically interested in studying much narrower beams of a width comparable to the lattice period, in order to observe e.g. discrete diffraction and self-trapping in the lattice. In this case the spectral extent of the Bloch wave excitation by a focused Gaussian beam will not be strictly limited to the region near the top of the band, but can indeed cover the whole Brillouin zone. Nevertheless, the linear excitation will be spectrally centered around the point at the top of the band.

Each of the two Bloch waves associated with the edges of the Bragg reflection gap can be excited by the sum of two coherent input beams inclined at the Bragg angle in opposite directions as illustrated in Fig. 2.4(a) (beams 2). The beams overlap at the lattice input face and create an interference pattern with fringes that approximately match both Bloch wave profiles and their staggered phase structure. Excitation of each of the waves at the bottom of the first band, and the top of the second band, is achieved by aligning the interference fringes with either the lattice maxima or minima, respectively [cf. Fig. 2.3(b)].

Figure 2.2 shows how the single Gaussian and the two-component input beams are generated experimentally in the extraordinarily polarised probe beam arm of the setup. A beam expanding telescope is used to decrease the width of the Gaussian beam waist in the focal point to the desired value for excitation at the top of the first band. Similar to the lattice beams, the staggered input beams are created in an interferometer that allow for adjusting the relative angle between the beams and hence the period of the interference fringes. One interferometer arm is reflected of a piezoelectrically actuated mirror which allows for controlling the relative phase between the beams and hence the horizontal alignment of the interference fringes at the lattice input.

Cylindrical lenses of 20 cm focal length are used to focus the probe beams in the horizontal direction at the crystal input face. The beams thus propagate through the crystal as vertically extended stripe beams. The single Gaussian beam is focused to a full width at half maximum (FWHM) comparable to the lattice period, i.e. 15 to 30 μm, depending on the particular experiment. The inclined input beams are spectrally located near the edge of the first Brillouin zone [Fig. 2.3(a)] where the band curvature and hence linear diffraction is greatly enhanced. Therefore they are focused to a FWHM of 70 μm, a factor of two or three wider than the single Gaussian, in order to achieve a comparable degree of spreading of all probe beams upon linear propagation through the lattice. The lattice period is typically 19 or 20 μm.

The right hand part of Fig. 2.4 shows the experimental intensity profiles at the crystal front face of (b) the optical lattice, (c) the single Gaussian input beam, and (d) the two-beam interference pattern when aligned with the lattice maxima for excitation of the Bloch wave at the bottom of the first band. White and grey shading schematically represent the areas of low and high refractive index, respectively [cf. Fig. 2.4(b)]. It is not possible to excite both types of staggered Bloch waves simultaneously in the experiment, but varying the relative phase of the input beams provides an experimentally convenient way to switch between excitation of each of them. It is worth to note that the beam envelope remains unchanged as the interference fringes are shifted, and that the possible asymmetry resulting from this

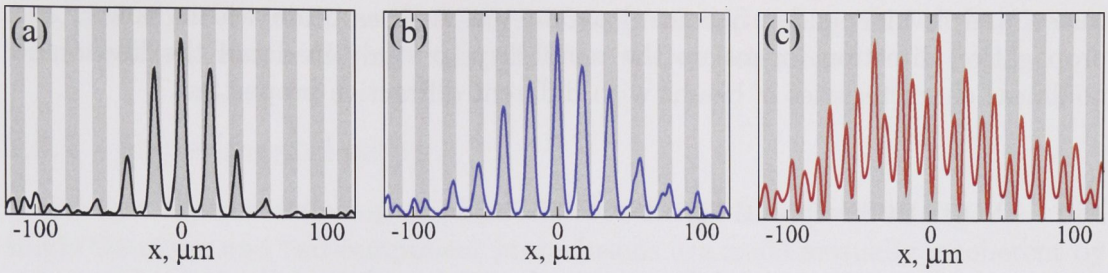

Figure 2.5: Experimental selective excitation of Bloch waves at (a) the top of the first band, (b) the bottom of the first band, and (c) the top of the second band. The plots show the measured intensity distribution at the crystal output after linear propagation of the probe beams in the lattice. The input beam width was 30 μm for single-beam excitation in (a), and 70 μm for two-beam excitation in (b) and (c).

is minimal since the beams are broad compared to the fringe period.

Figure 2.5 presents the experimentally observed selective excitation of linear Bloch waves at (a) the top of the first band, (b) the bottom of the first band, and (c) the top of the second band. The plots show the transverse (horizontal) intensity distribution measured at the crystal output for a bias voltage of 2kV. The output beams possess the unique characteristics of the three considered Bloch waves. The Gaussian beam evolves into the modulated wave with uniform phase structure at the top of the first band [Fig. 2.5(a)]. The two-component beams excite either the first or second band staggered Bloch wave, depending on the alignment with the lattice. All excitations are exceptionally pure with negligible beam asymmetry and only minor mixed excitation visible in the tails of the beams. The phase structure of the excited waves can be measured by interfering the output beams with a reference plane wave [see Chapter 3]. The characteristic double peak structure of the second band beam appears at higher lattice contrast for bias voltages above $\sim$ 1.5 kV. All excited Bloch waves propagate straight down the lattice with zero transverse velocity, and for all three beams the output width is about a factor of two larger than the input width due to linear diffraction.

The two-beam excitation method provides efficient and fully controlled excitation of immobile staggered Bloch waves [46, 47, 90, 91]. The majority of the input power is coupled directly into the desired Bloch wave which propagates straight down the lattice with zero transverse momentum thanks to an exact power balance between the two inclined input beams. In comparison, simple excitation by a single inclined input beam [45, 92] leads to far less efficient excitation due to strong Bragg reflections from the periodic structure, and the excited waves propagate across the lattice with nonzero transverse momentum. An alternative prism coupling method allowing for specific Bloch wave excitation in planar waveguide arrays was demonstrated in a recent work [93].

The ability demonstrated in our experiment to selectively excite specific Bloch

waves, and to independently control parameters such as beam width, power, and propagation direction, opens up the possibility to study in detail the linear and nonlinear characteristics of beams with different diffractive properties.

2.5 Nonlinear beam interactions

Despite the fundamental differences in their nature, beams that experience normal and anomalous diffraction spread in a similar manner upon linear propagation in a straight photonic lattice [cf. Fig. 2.5]. However, dramatic differences between the two types of diffraction manifest themselves when nonlinearity comes into play. In the case of self-focusing nonlinearity, self-trapping of light is possible in the normal diffraction regime, whereas the opposite effect, i.e. increased beam spreading, occurs in the anomalous diffraction regime [cf. Section 1.8].

Nonlinearity thus provides a means of probing and studying the diffractive properties of beams in periodic structures.

In addition nonlinearity introduces the possibility to study *nonlinear interaction* of waves through the effect of cross-phase modulation, i.e. the fact that a nonlinear index change induced by one beam is experienced simultaneously by other co-propagating beams. In this Section we study in detail such nonlinear coupling of beams associated with different Bloch waves in a photonic lattice and, among other effects, experimentally demonstrate *mutual focusing* of first and second band beams in the normal diffraction regime [74].

Mutual beam focusing is a fundamental nonlinear effect which is closely related to the existence of multi-component spatial solitons that are mutually trapped through cross-phase modulation. Mutual focusing indeed represents the experimental precursor for the formation of such *vector solitons* which exist even in homogeneous dielectric media [4]. In periodic systems, vector solitons consisting of mutually coupled components localised in different bandgaps have been predicted theoretically [94–97]. Previously it has been demonstrated experimentally that partially coherent beams can excite modes in several gaps that experience mutual trapping in media with slow photorefractive nonlinearity [98]. Also, mutual focusing of orthogonally polarised waves excited in different bands, as well as formation of single-polarisation multiband breathers, was observed in AlGaAs waveguide arrays [99, 100]. Coherently coupled multiband vector breathers were also observed in liquid crystal waveguide arrays [101].

The setup described in Section 2.3 above is designed to allow for simultaneous excitation of *mutually incoherent* waves associated with the edges of the first and second transmission bands, and for independent control over the beam width and amplitude of these waves. This flexibility enables us to reveal novel multiband beam interaction effects in regimes that were not accessed in other experimental studies of interband mutual coupling [98–101]. In particular, we demonstrate an inherent modal asymmetry in the effect of discrete mutual focusing of beams generated at the upper edges of the first two transmission bands. In addition, we study in detail the complex interaction of waves exhibiting diffraction of different magnitude and

sign, and observe simultaneous beam focusing and defocusing, as well as discrete beam break-up and reshaping within the first transmission band.

2.5.1 Experimental setup

We use the generic setup described in Section 2.3 and shown in Fig. 2.2. The single Gaussian and two-component probe beams are made mutually incoherent by vibrating a piezoelectrically controlled mirror placed in the single-beam arm [cf. Fig. 2.2] at high frequency (a few hundred Hz). Unless otherwise stated, the two single beam and the two-component probe beams have an input full width at half maximum (FWHM) of 17 ± 3 μm and 70 ± 3 μm, respectively. Since the nonlinear response time of the crystal is on the order of a few seconds, each probe beam output can be recorded separately by blocking the other probe and lattice beams immediately (<1 s) before taking a snapshot image of the intensity distribution.

2.5.2 Interband mutual focusing

We first study discrete *interband* coupling of the two beams associated with the Bloch waves at the top of the first and the second band [Fig. 2.5(a) and (c)]. Both exhibit *normal* diffraction and can therefore become self-trapped at higher powers by the self-focusing nonlinearity. This leads to the possibility of observing mutual focusing since each beam is capable of inducing a local lattice defect that traps the other component. In order to form true vector solitons the power of each component must be smaller than the nonlinear threshold required for soliton formation, such that only the combined beam power allows for mutual focusing and trapping of both beams. However, the effect of mutual focusing itself can occur for a wide range of different relative and absolute beam powers.

Here we investigate the extreme cases in which the power of the two probe beams are strongly imbalanced, i.e. only one component at a time propagates nonlinearly. We initially set the power of both beams at a low (nW) level so that they propagate in a linear regime. Then the power of one of the components is increased and the nonlinear effect on both beams is studied. Finally the roles of the beams are switched, and the effect of the nonlinear propagation of the second component is studied.

This approach facilitates clear experimental observation of the individual nonlinear coupling effects, and in addition allows for studying the possible *asymmetry* of the interactions, resulting from the fact that co-propagating beams of different nature may produce fundamentally different self-action effects and therefore influence each other differently when coupled nonlinearly. As we shall see this is the case for all the Bloch waves considered here.

Figure 2.6 shows the result of increasing the power of the fundamental first band beam (black). Transition from discrete diffraction of this beam in the linear regime [Fig. 2.6(a), top] to self-focusing at higher power [Fig. 2.6(b), top] is accompanied by a decrease in the FWHM of the broader co-propagating second band beam (red) by almost a factor of two [Fig. 2.6(a,b), bottom]. The width of the second band

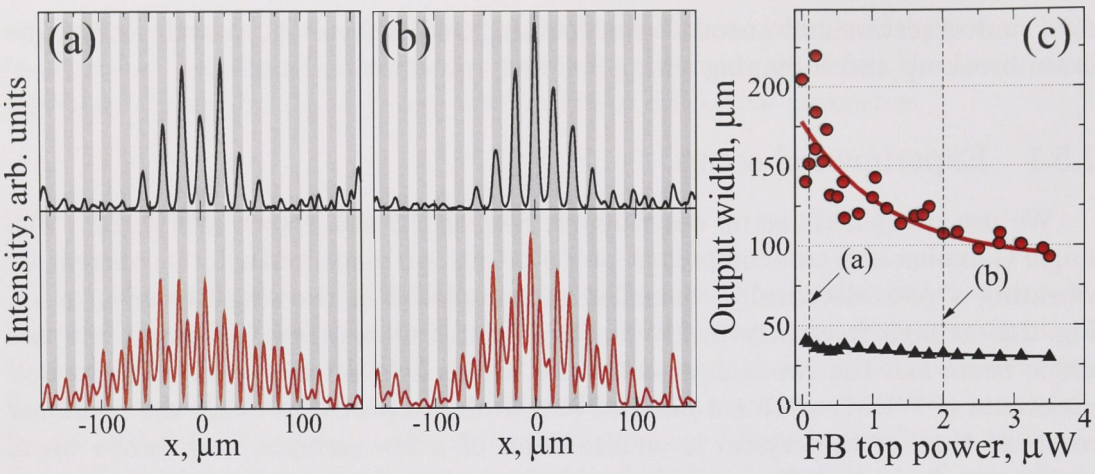

Figure 2.6: Experimental results for interband mutual focusing of the beams generated at the top of the second band (red) and top of the first band (black). (a) Both components at low power. (b) First band beam at high power and second band beam at low power (70 nW). (c) Beam width vs. power of the first band beam. Solid curves are exponential fits to the data points.

beam is estimated by a Gaussian envelope fitting, whereas we describe the width of the first band beam by the discrete second order central moment of the three central lattice sites, calculated as $w^2 = d^2(2P_{-1} + P_0 + 2P_1)/(P_{-1} + P_0 + P_1)$, where d is the lattice period and P_n the intensity of the $n-$th site. The beam width is then characterised by $2w$. To investigate the effect in further detail, we measure the degree of focusing of both components as a function of power of the first band beam. The result is shown in Fig. 2.6(c), and we notice that the width of the passive second band beam asymptotically shrinks from $\sim 180\mu$m to $\sim 90\mu$m, whereas the focusing effect is relatively small for the first band beam itself. In all experiments described here beam powers are measured as the total output from the crystal back face.

Interband focusing is also observed if, conversely, the power of the first band component is maintained at a low level and that of the second band beam is increased [Fig. 2.7]. However, the nonlinear defect induced by the second band beam is rather broad and weak, and therefore a less pronounced focusing of the first band beam is observed in this case. In fact, it was necessary to slightly increase the input width of the first band beam to 20 μm in order to reduce diffraction and thereby facilitate focusing. This is why in this case no clear discrete diffraction is observed for linear propagation of the first band beam in Fig. 2.7(a). Figure 2.7(c) maps the observed beam profiles as a function of the second band beam power in a two-dimensional plot, and the gradual focusing of both beams is clearly visible.

The observed asymmetry in the strength of the coupling between the bands reflects the fact that the physics of light localisation in the total internal reflection gap (first band) and in the Bragg reflection gap (second band) is quite different.

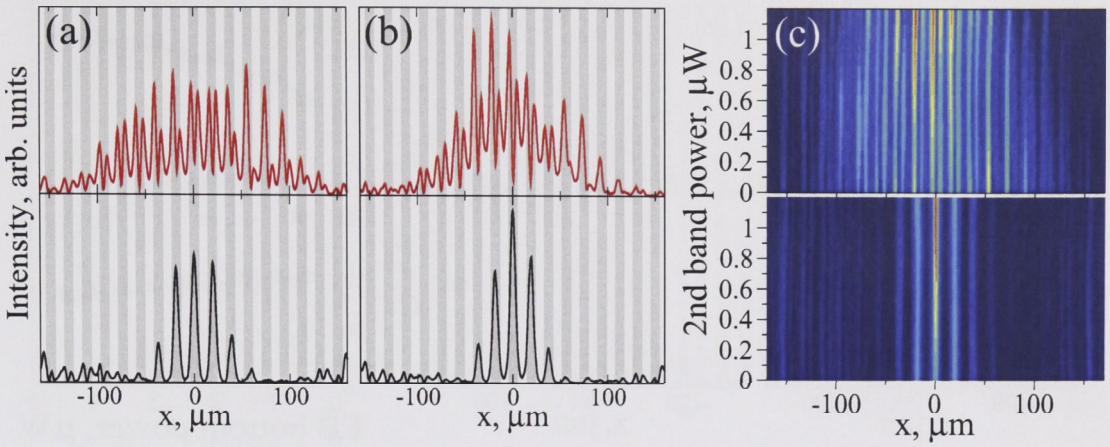

Figure 2.7: Experimental results for interband mutual focusing of the beams generated at the top of the first band (black) and top of the second band (red). (a) Both components at low power. (b) Second band beam at high power (900 nW) and first band beam at low power (100 nW). (c) Two-dimensional visualisation of output profiles for increasing power of the second band beam.

Indeed, a discrete soliton in the total internal reflection gap creates a narrow and strongly localised defect, whereas both the minimum width and the maximum intensity of a Bragg gap soliton are limited due to the finite spectral width of the Bragg reflection gap. This means that there is also a limit to the trapping strength of the self-induced second band defect. The generic features of these different light trapping mechanisms may well account for the saturating focusing of the second band beam [Fig. 2.6(c)], and the observed interband coupling asymmetry, i.e. the fact that the two beams are not equally capable of trapping each other. The above observations together represent the demonstration of mutual focusing of two mutually incoherent beams originating from different bands. This effect is responsible for the formation of multigap vector solitons as predicted theoretically [94–97].

2.5.3 Interaction of beams with normal and anomalous diffraction

Whereas mutual focusing of coupled beams is expected to occur in the normal diffraction regime, it is not obvious what will happen if several beams from regimes of different diffraction are allowed to interact nonlinearly. Here we study the *intraband* coupling of the two waves associated with the top and the bottom of the first band [Fig. 2.5(a) and (b)]. These waves exhibit *normal* and *anomalous* diffraction, respectively, and therefore the first self-focuses while the second experiences defocusing as a result of the self-focusing nonlinearity. However, the picture is more complicated when the two waves interact via the nonlinear medium.

We show that in this case nonlinear beam coupling can lead to simultaneous focusing and defocusing and to complex effects such as discrete beam-breakup or reshaping. Indeed, when the power of the beam associated with the bottom of the

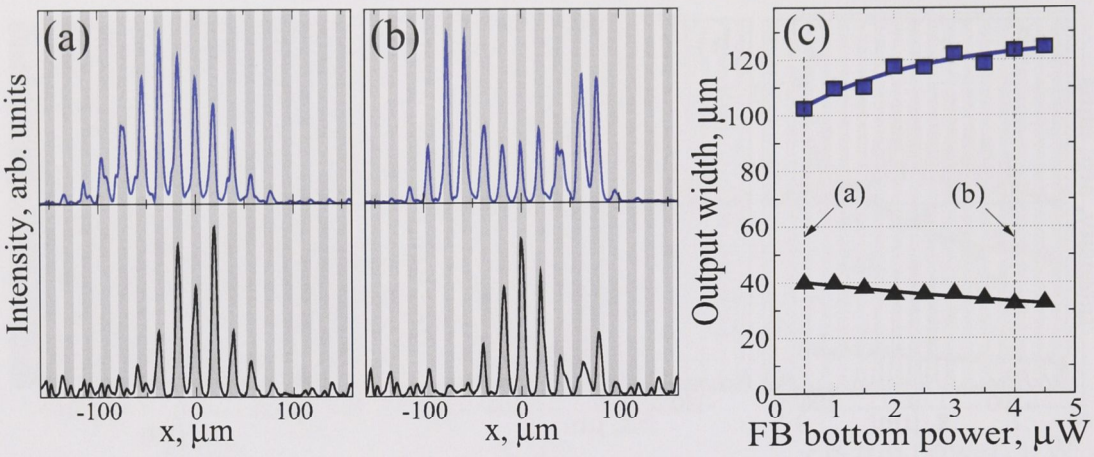

Figure 2.8: Experimental results for coupling of beams at the top (black) and bottom (blue) of the first band. (a) Both components at low power. (b) Bottom of first band at high power and top of first band at low power (100 nW). (c) Beam width vs. power of the beam at the bottom of the first band.

band is increased [Fig. 2.8] it does spread out stronger due to self-defocusing (blue). However, it still induces a lattice defect that causes the beam at the top of the band (black) to focus, thus leading to *simultaneous* focusing and defocusing of beams belonging to different parts of the bandgap spectrum. Figure 2.8(c) shows that the corresponding beam widths respectively decrease and increase almost linearly as a function of the power of the beam at the top of the band.

It is important, though, to point out that whereas the interband mutual focusing discussed in Section 2.5.2 above can lead to the formation of stable multi-gap vector solitons, the intraband coupling effects responsible for the observed simultaneous focusing and defocusing [Fig. 2.8] are inherently *transient* in nature since the two beams will eventually decouple from each other at longer propagation distances. However, from the point of view of applications in spatial beam control, soliton formation is not necessarily required. Even spatially transient effects may be sufficient for achieving effective beam manipulation functionalities such as beam steering, switching, or reshaping.

In the opposite case [see Fig. 2.9], the beam at the top of the band self-focuses at high powers, but induces a repelling defect for the defocusing beam at the bottom of the band. We observe that as the power of the fundamental beam is increased, the beam at the bottom of the band undergoes a complex spatial reshaping. The two lattice sites next to the central one are increasingly depleted as the power increases [Fig. 2.9(b) and Fig. 2.9(c)]. Eventually, at high power [Fig. 2.9(c)], the output profile is composed of a single centrally localised peak and two discretely repelled outer lobes. Clearly, this complex beam reshaping cannot be described by a simple envelope approximation and calls for further investigations.

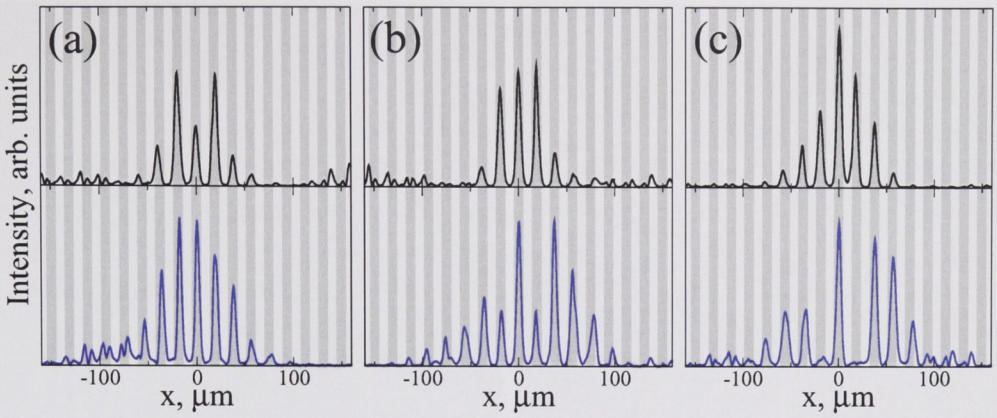

Figure 2.9: Experimental results for coupling of beams at the bottom (blue) and top (black) of the first band. (a) Both components at low power (50 nW). (b) Top of first band at intermediate power (1.5 μW) and bottom of first band at low power. (c) Top of first band at high power (4.0 μW) and bottom of first band at low power.

2.5.4 Numerical simulations

To support our experimental results and to more closely examine the features associated with discrete localisation and beam shaping effects for waves with opposite diffraction properties within the first band, a series of extended numerical simulations were performed.

Propagation of several mutually incoherent beams in an optically induced lattice is described by a system of coupled nonlinear Schrödinger equations for the normalised beam envelopes $\psi_n(x, z)$ [cf. Section 1.2.6],

$$i\frac{\partial \psi_n}{\partial z} + D\frac{\partial^2 \psi_n}{\partial x^2} + \mathcal{F}(x, I)\psi_n = 0, \tag{2.1}$$

where $I = \sum_n |\psi_n|^2$ is the total beam intensity, x and z are the transverse and propagation coordinates normalised to the characteristic values x_0 and z_0, respectively, $D = z_0\lambda/(4\pi n_0 x_0^2)$ is the beam diffraction coefficient, n_0 is the average refractive index of the medium, and λ is the wavelength in vacuum. The total refractive index change induced by (i) the lattice beams and (ii) the nonlinear self-action of the probe beam is characterised by the function

$$\mathcal{F}(x, |\psi|^2) = -\frac{\gamma}{I_b + I_p(x) + |\psi|^2}, \tag{2.2}$$

where I_b is the constant dark irradiance (background illumination), $I_p(x) = I_g \cos^2(\pi x/d)$ is the interference pattern which induces a one-dimensional lattice with period d, and γ is a nonlinear coefficient proportional to the applied DC field [28, 61, 62]. Equation (2.2) takes into account the saturable nature of the photorefractive nonlinearity, and the sign of the expression ensures a self-focusing

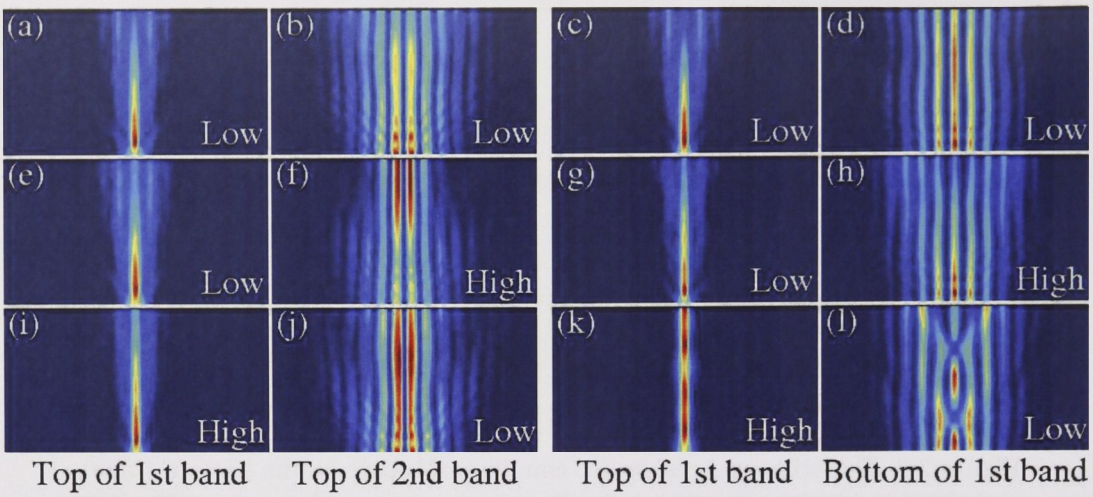

Figure 2.10: Beam propagation method simulations of interband focusing (left columns) and focusing-defocusing interactions within the first band (right columns). The beam at top of the first band is paired with either the beam at the top of the second band (left columns), or the beam at the bottom of the first band (right columns). Each plot window is 320 μm and 15 mm in the transverse (x) and propagation (z) directions, respectively. The refractive index modulation of the latice is 2×10^{-4}. In (a,b) and (c,d) each pair of co-propagating probe beams experience linear diffraction at low power. In (e,f) the power of the beam at the top of the second band is increased and, conversely, in (i,j) the power of the beam at the top of the first band is increased. In both cases simultaneous focusing of the two beam components is observed. In (g,h) the beam at the bottom of the first band experiences self-defocusing at increasing power, while the beam at the top of the first band is focused. In (k,l) the beam at the top of the band self-focuses at high power, while the low power beam at the bottom of the band experiences complex reshaping and interference effects upon propagation.

type nonlinear response provided $\gamma > 0$. To match our experimental conditions, we use the following parameters: $\lambda = 0.532$ μm, $n_0 = 2.4$, $x_0 = 1$ μm, $z_0 = 1$mm, $d = 19$, $I_b = 1$ and $I_g = 1$. Then, the refractive index modulation of the lattice is $\Delta n = \gamma\lambda/(4\pi z_0)$, which evaluates to 2×10^{-4} for $\gamma = 4.72$. The crystal length is $L = 15$ mm.

Numerical simulations confirm all essential aspects of our experimental observations, including the asymmetric interband coupling, the transitional mutual focusing and defocusing, and the discreteness-induced reshaping of the anomalously diffracting beam at the bottom of the first band. Fig. 2.10 shows examples of simulations representing the experimentally studied cases of mutual interband focusing [cf. Fig. 2.6 and Fig. 2.7], and focusing-defocusing interactions within the first band [cf. Fig. 2.8 and Fig. 2.9]. The labels 'low' and 'high' in Fig. 2.10 refer to low and high input power, i.e. to the regimes of linear and nonlinear propagation, respec-

tively. In each simulation the input beam profile and width was chosen to match the corresponding experimental cases.

The left half of Fig. 2.10 shows the propagation of the beams associated with the top of the first band (first picture coloumn) and the top of the second band (second picture coloumn). At low power the beams experience linear diffraction broadening upon propagation [Fig. 2.10(a,b)]. Mutual focusing is readily observed when increasing the power of either the second band beam [Fig. 2.10(e,f)] or the first band beam [Fig. 2.10(i,j)]. As observed in the experiment a clear asymmetry in the nonlinear coupling is manifested by the fact that the passive trapping is much less pronounced for the first band beam [Fig. 2.10(e)] than for the second band beam [Fig. 2.10(j)].

The right half of Fig. 2.10 shows the propagation of the beams associated with the top of the first band (third picture coloumn) and the bottom of the first band (fourth picture coloumn). At low power the beams experience linear diffraction broadening upon propagation [Fig. 2.10(c,d)]. As in the experiment, simultaneous focusing and defocusing is observed when the power of the beam at the bottom of the band is increased [Fig. 2.10(g,h)]. The transitory nature of this effect and consequently the ultimate delocalisation of both beams was verified by numerically extending the propagation distance.

The complex reshaping of the beam at the bottom of the first band is observed numerically when the beam at the top of the band self-focuses at higher power [Fig. 2.10(k,l)]. At the crystal output the beam is comprised of a central peak, two almost depleted lattice sites, and two separated outer lobes, as observed experimentally [Fig. 2.9(c)]. Furthermore, the insight into the longitudinal propagation dynamics offered by the simulation reveals a periodic interference effect, which indicates beating between beam components with different longitudinal propagation constants: power seems to oscillate back and forth between the central lattice site and its two adjacent neighbours upon propagation [Fig. 2.10(l)]. This would suggest that in the presence of the nonlinearly induced lattice defect the power of the passive beam is redistributed in different spectral regions of the bandgap diagram, whereas the initial input beam was located at the edge of the first Brillouin zone, at the bottom of the first band.

The idea of spectral redistribution of energy is supported by simulations for longer propagation distances (50 mm) presented in Fig. 2.11. The results show that the two outer lobes of the reshaped beam eventually propagate away from the centre in opposite directions, i.e. in the lower parts of the band, and that the central peak remains trapped at the nonlinear defect, i.e. inside the total internal reflection gap. Indeed this interpretation would imply a difference in longitudinal propagation constant of about 0.28 mm^{-1} [the width of the first band in Fig. 2.3], corresponding to a beat length of 22 mm. This is consistent with the beating period on the order of several millimeters observed in simulations. The beat length will depend strongly on (i) the lattice contrast which determines the width of the bands and the gaps, and (ii) the power of the defect writing beam which determines how far the propagation constant at the central lattice site is pushed upwards into the total internal reflection gap.

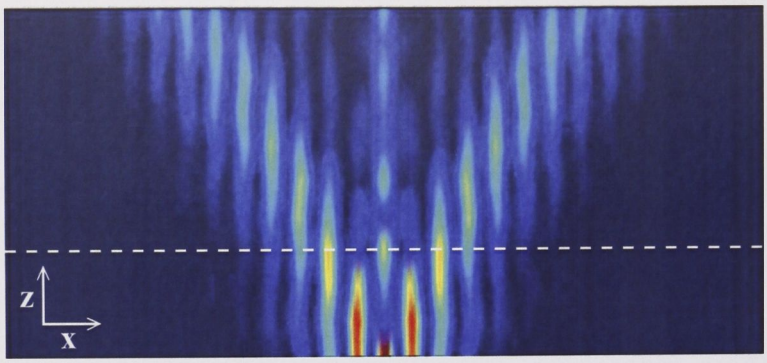

Figure 2.11: Beam propagation method simulation of the coupling of beams associated with the top and bottom of the first band. The plot shows the extended linear propagation of the beam at the bottom of the first band *only*, when the beam at the top of the first band (not shown) induces a centrally localised nonlinear lattice defect at high power (normalised peak intensity is 1). The plot window is 560 μm and 50 mm in the transverse (x) and propagation (z) directions, respectively. For comparison the length of the crystal, i.e. the propagation distance in the experiment, is marked with a dashed white line. In this simulation the refractive index modulation of the latice is 1.5×10^{-4}.

The FWHMs of the single Gaussian and the two-component input beams were 15 μm [20 μm in Figs. 2.10 (a) and (e)] and 70 μm, respectively. In the simulations presented in Fig 2.10 the peak intensity of the high power components (normalised to a constant dark irradiance I_b) were 0.25 in (e,f) and (i,j), 1.69 in (g,h), and 3.24 in (k,l). The simulations correctly account for all the experimentally observed effects. Only minor discrepancies are observed in the simulations: the second band beam does not display the double peak structure observed experimentally for the given parameters [see e.g. Fig. 2.6], and in the case presented in Fig. 2.10(k,l) the beam associated with the top of the first band experiences stronger self-focusing than observed experimentally. Nevertheless we conclude a qualitatively good agreement between theory and experiment.

2.6 Tunable beam steering in tilted lattices

So far we have been concerned with beams propagating straight along the optically induced photonic lattice with zero transverse momentum. The balanced two-component excitation technique makes it possible to realise such immobile propagation even for Bloch waves at the edges of the Bragg reflection gap. We have seen that beams associated with different Bloch waves diffract in a similar manner in the linear regime [cf. Fig. 2.5], but that they behave and interact very differently in the nonlinear regime.

In this Section we show that even in the linear regime strong differences in the

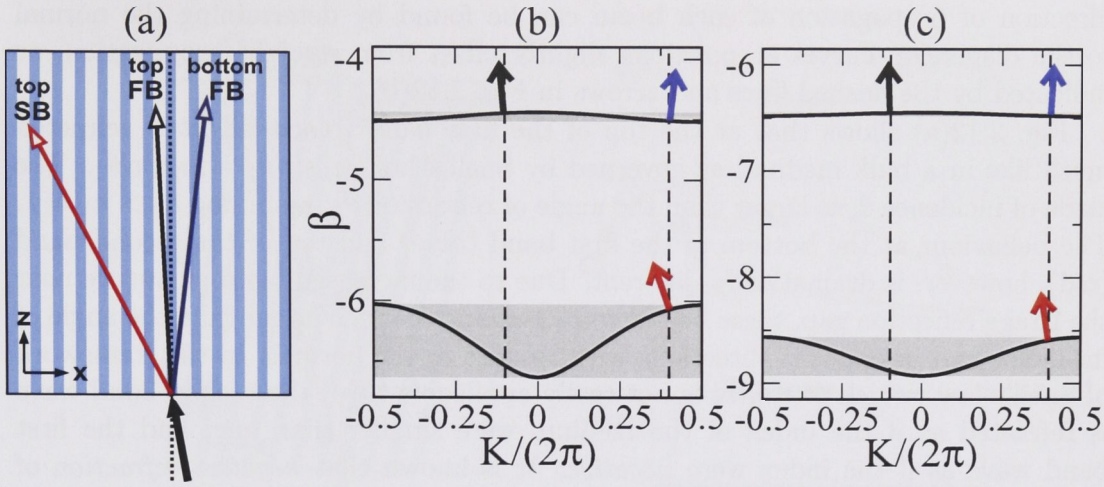

Figure 2.12: (a) Schematic of a one-dimensional photonic lattice, and the refraction of inclined beams associated with Bloch waves at the top and bottom of the first band (FB) and top of second band (SB). The beams are incident at a small angle with respect to the normal to the crystal front face. (b,c) Bloch wave diffraction curves in (b) shallow ($\Delta n = 0.3 \times 10^{-3}$) and (c) deeper ($\Delta n = 0.45 \times 10^{-3}$) lattices. The lattice period is 19 μm. Arrows schematically indicate the propagation direction of individual Bloch waves excited by inclined input beams.

diffractive properties of Bloch waves can be experimentally observed, and exploited for beam steering purposes. We consider beam propagation in a *tilted* lattice and show that Bloch waves refract or *steer* in different directions inside the crystal because of their unique diffractive properties.

We demonstrate that in optically induced lattices the beam steering can be dynamically tuned by varying the applied bias voltage and hence the contrast of the refractive index modulation [75]. In addition, for waves with normal diffraction at the top of the bands, the beam steering can be combined with nonlinear self-focusing in the nonlinear regime to suppress beam broadening due to diffraction.

2.6.1 Bloch wave refraction and beam steering

The diffraction of waves in a periodic structure is governed by the magnitude and sign of the local *curvature* of the linear transmission bands, and similarly, the direction of propagation is related to the local *slope* of the bands at a given point in the bandgap diagram [see Section 1.7]. At normal incidence beams associated with Bloch waves at the bandedges propagate straight along the lattice because the slope of the dispersion curves is zero, and the normal points along the z direction. However, if the input beams are incident at a small angle with respect to the lattice, they will refract - or steer - in different directions, as illustrated in Fig. 2.12(a). The

direction of propagation of each beam can be found by determining the normal to the dispersion curves at positions slightly offset from straight propagation, as indicated by the dashed lines and arrows in Fig. 2.12(b).

Fig. 2.12(a) shows that at the top of the first band (black), light is refracted much like in a bulk medium as governed by Snell's law, $n_1 \sin\theta_1 = n_2 \sin\theta_2$. The angle of incidence θ_1 is larger than the angle of refraction θ_2, assuming $n_2 > n_1 = 1$. The behaviour at the bottom of the first band (blue) and top of the second band (red), however, is dramatically different. Due to the increased band curvature near the Bragg reflection gap, these beams refract at angles much larger than the angle of incidence and in opposite directions with respect to the normal. In the framework of Snell's law (which of course is not really applicable here) the second band wave is refracted as if the index of the medium were smaller than one, and the first band wave as if the index were *negative*. It is known that *negative refraction* of electromagnetic waves is possible as a result of the modified dispersion relations in periodic structures, and it has been previously observed in photonic crystals [102], and even in weakly modulated one-dimensional photonic lattices [14]. We note, however, that negative refraction in such structures is different from the case of truly left-handed *metamaterials* where the refractive index is indeed negative due to simultaneously negative permeability and permittivity [103, 104].

In this work we demonstrate how the Bloch wave refraction and beam steering can be dynamically controlled in tunable periodic structures such as optically induced lattices.

The local slope and curvature of the linear transmission bands depend strongly on the refractive index contrast of the photonic lattice. Increasing the index modulation leads to stronger Bragg reflection from the periodic structure. This translates into wider bandgaps which squeeze and flatten the transmission bands as shown in Figs. 2.12(b,c). As a result of this both the curvature and slope of the bands are reduced, leading to decreased diffraction and refraction of the incident beams. In an optically induced lattice, the refractive index contrast can be modified dynamically by tuning the crystal bias voltage [cf. Section 2.2], and combined with the unique diffractive and refractive properties of Bloch waves in periodic structures, this provides a novel mechanism for realising tunable beam steering.

Apart from optically induced lattices, a number of different physical systems offer the possibility of realising photonic lattices with variable index contrast for dynamic beam steering, including thermo-optically tuned polymer waveguide arrays [43, 44, 105] and voltage-controlled nematic liquid crystal cells with patterned electrodes [66, 106].

2.6.2 Numerical simulations

When studying Bloch wave refraction and beam steering experimentally, it is convenient to rotate the optical lattice inside the crystal rather than inclining the probe beams [cf. Section 2.3]. Hereforth we therefore consider the case of a *tilted lattice* where input beams, as previously, propagate at normal incidence to the crystal front face. We define a lattice tilt angle, α, and a beam steering angle, θ,

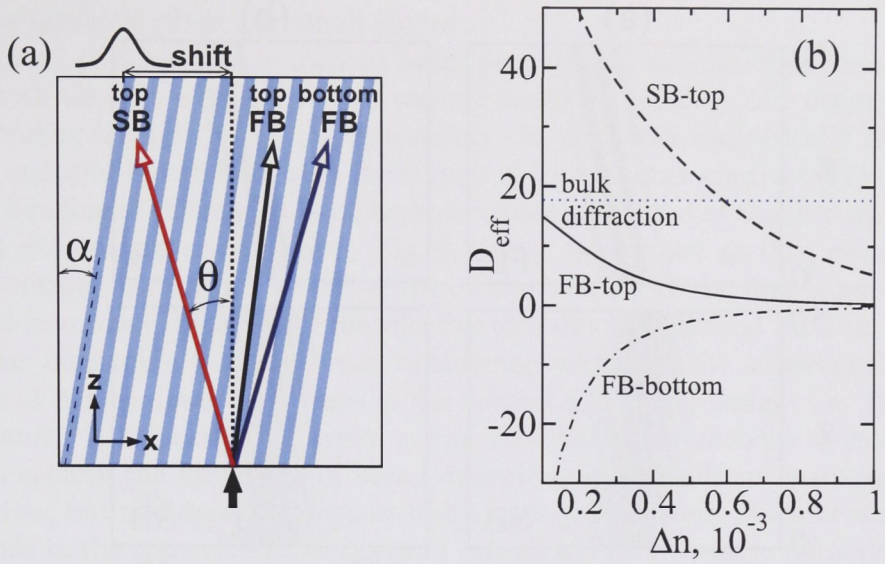

Figure 2.13: (a) Schematic of the Bloch wave steering in a tilted photonic lattice for normal beam incidence. (b) Effective diffraction coefficients at the three band edges vs. the refractive index modulation of the lattice Δn, compared with the bulk diffraction D (dotted line).

corresponding to the shift of the beam centre at the crystal output, as illustrated in Fig. 2.13(a).

Propagation of extraordinarily polarised beams with amplitude $\psi(x, z)$ is then described by the equation

$$i\frac{\partial\psi}{\partial z} + D\frac{\partial^2\psi}{\partial x^2} + \mathcal{F}(x - \alpha z, I)\psi = 0, \tag{2.3}$$

where α is the angle of the lattice tilt, x and z are the transverse and propagation coordinates normalised to the characteristic values x_0 and z_0, respectively, I is the normalised beam intensity, $D = z_0\lambda/(4\pi n_0 x_0^2)$ is the beam diffraction coefficient, n_0 is the average refractive index of the medium, λ is the wavelength in vacuum, $\mathcal{F}(x, I) = -\gamma\left[I_b + I_g\cos^2(\pi x/d) + I\right]^{-1}$, I_b is the constant dark irradiance, I_g is the peak intensity of the interference pattern of period d, and γ is a nonlinear coefficient directly proportional to the applied DC field. To match our experimental conditions, we use the following parameters: $\lambda = 0.532$ μm, $n_0 = 2.4$, $x_0 = 1$ μm, $z_0 = 1$mm, $d = 19$, $I_b = 1$, $I_g = 1$, and the crystal length $L = 15$ mm. Then, the refractive index contrast in the lattice is $\Delta n = \gamma\lambda/(4\pi z_0)$.

In a *tilted lattice*, the Bloch wave dispersion can be written as $\widetilde{\beta}[\kappa] = \beta[\kappa - \alpha d/(2D)] - \kappa\alpha/d + \alpha^2/(4D)$, where $\beta(\kappa)$ is the dispersion relation in a straight lattice ($\alpha = 0$) [cf. Section 1.7]. The modified dispersion relation indicates that in a tilted lattice the dispersion curves are simultaneously *translated* and *tilted* with α. When an input beam excites Bloch waves from a particular spectral band, its

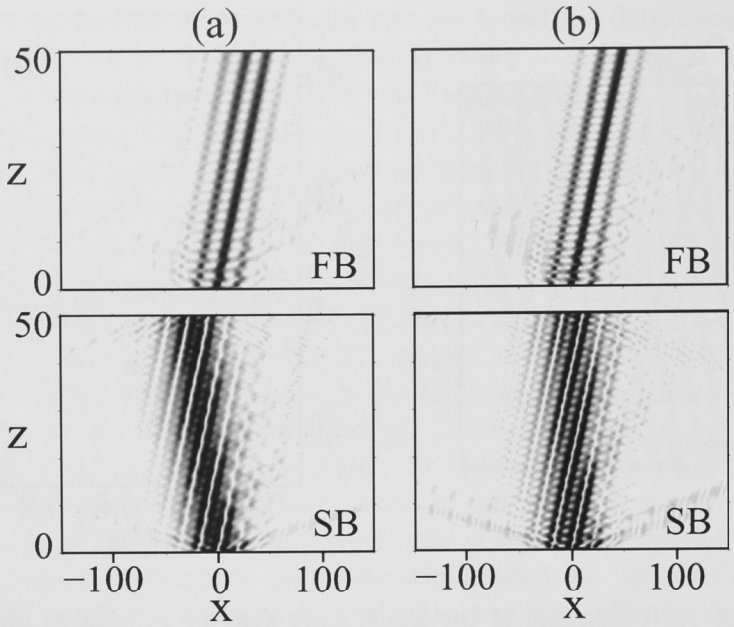

Figure 2.14: Numerical beam propagation simulation showing the refraction of self-trapped beams associated with the top of the first band (FB) and the top of the second band (SB), for (a) weak and (b) strong lattice contrast, corresponding to Figs. 2.12(b) and 2.12(c), respectively. The lattice tilt angle is $\alpha = 1$ mrad.

normalised propagation angle inside the lattice can be found as $\theta = -d\widetilde{\beta}/d\kappa$. As discussed above waves corresponding to the middle ($\kappa = 0$) or edge ($\kappa = \pm\pi$) of the Brillouin zone always propagate straight if the lattice is not tilted ($\alpha = 0$), since $\theta = 0$ at all band edges [see e.g. Fig. 2.3(a)]. However, in a tilted lattice the same waves refract at an angle $\theta = -d\partial\beta[\kappa - \alpha d/(2D)]/\partial\kappa + \alpha \simeq \alpha(D - D_{\text{eff}})/D + O(\alpha^2)$, where $D_{\text{eff}} = -(d^2/2)\partial^2\beta/\partial\kappa^2$ is the effective diffraction coefficient of the Bloch waves. Thus, the beam refraction induced by the lattice tilt is proportional to the difference of the diffraction coefficients in a bulk crystal and in the lattice at the corresponding κ.

Results of calculations presented in Fig. 2.13(b) show that at the top of the first band $0 < D_{\text{eff}} < D$, and therefore the beam is refracted in the direction of the lattice tilt [cf. Fig. 2.13(a)]. At the bottom of the first band, $D_{\text{eff}} < 0$, and the beam is refracted even stronger in the same direction. At the top of the second band, D_{eff} crosses the value of the bulk diffraction D at a critical value of the refractive index modulation Δn_{cr}, defining two different regimes of refraction of the second band wave. In shallow lattices, when $\Delta n < \Delta n_{\text{cr}}$, $D_{\text{eff}} > D$ and the beam experiences refraction in the direction *opposite* to the lattice tilt [cf. Fig. 2.13(a)], whereas $D_{\text{eff}} < D$ and refraction in the direction along the lattice tilt should occur in deeper lattices, when $\Delta n > \Delta n_{\text{cr}}$. Remarkably, in the critical case when $\Delta n \simeq \Delta n_{\text{cr}}$ and $D_{\text{eff}} \simeq D$, the second band beam will propagate straight through the crystal even

when the lattice is tilted (for small angles).

Figures 2.14(a,b) show numerical beam propagation simulations of beams associated with the top of the first and second bands, in shallow and deeper lattices corresponding to Figs. 2.12(b,c), respectively. As predicted theoretically the beams steer in opposite directions inside the crystal at lower lattice contrast [Fig. 2.14(a)], and the bending of the second band beam is strongly reduced at the increased lattice contrast close to the critical value [Fig. 2.14(b)]. In contrast to this, changing the lattice contrast has a much weaker effect on the steering of the first band beam, as expected from the calculation of the effective diffraction coefficient [cf. Fig. 2.13(b)].

Linear diffraction leads to beam broadening which can be suppressed by self-focusing at higher power for beams in the normal diffraction regime, i.e. at the top of the bands. In the examples shown in Fig. 2.14, the beam intensity is increased in order to achieve the formation of broad discrete and gap solitons spanning several lattice sites, but maintaining constant width upon propagation. Such broad solitons are mobile in the transverse direction and exhibit the same generic refraction as the corresponding linear beams [45].

2.6.3 Experimental characterisation of Bloch wave steering

The Bloch wave steering is expected to strongly depend on the lattice tilt angle, as the latter changes the effective diffraction coefficient of the Bloch waves by scanning along the diffraction curves [Fig. 2.12(b,c)]. It is therefore interesting to experimentally characterise how the Bloch wave steering depends on the lattice tilt angle.

In the experiment we use the same setup as described in Section 2.3 above [see Fig. 2.2]. The beam splitter cube placed immediately in front of the SBN crystal is used to rotate the optical lattice without changing the initial propagation direction of the probe beams [as illustrated in Fig. 2.13(a)]. The variable transverse shift of the probe beams caused by refraction in the beam splitter cube is accounted for by calibration of the input beam positions on the crystal front face. The lattice tilt angle is measured by reflecting a narrow HeNe laser beam off the beam splitter cube. The laser beam is projected onto a screen at a distance l from the beam splitter, where its transverse deflection Δx is measured ($\Delta x \ll l$). The tilt angle of the lattice inside the crystal is smaller than the angle measured in air (Δ/l) by a factor of n_0 (the refractive index of the crystal).

Figure 2.15(a) shows the change of the beam position at the output face of the crystal as a function of the lattice tilt angle α inside the crystal [cf. Fig. 2.13(a)]. The corresponding shift of the lattice at the crystal output is indicated by a dashed line. The three beams are observed to steer exactly as predicted theoretically and illustrated in Fig. 2.13(a). That is, the beam at the top of the first band is shifted by a relatively small amount at the output, following the direction of the lattice tilt. The beam at the bottom of the first band is shifted strongly in the same direction, at an angle exceeding the lattice tilt angle by a factor of about two. Finally, the beam at the top of the second band shifts equally strongly in the direction opposit to the lattice tilt.

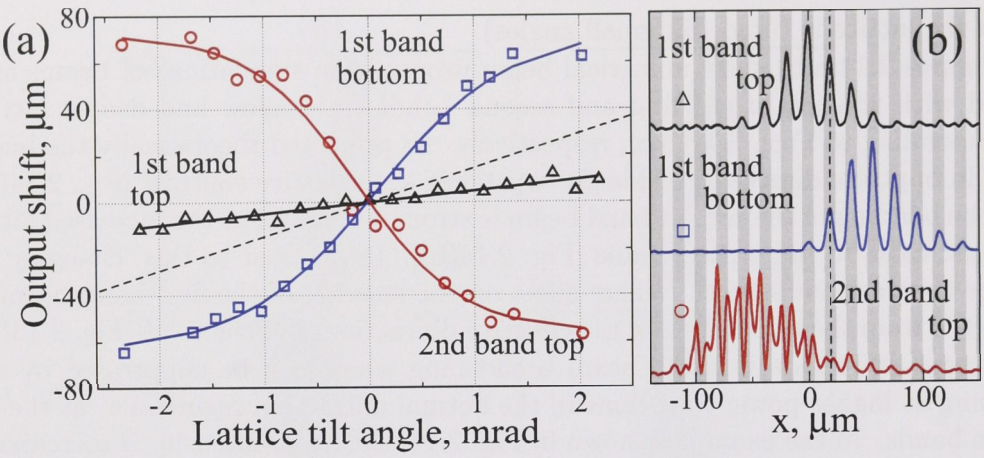

Figure 2.15: (a) Shift of the output position of beams associated with three different Bloch waves vs. the lattice tilt. (b) Characteristic beam profiles for a tilt of 1.25 mrad. In (a,b) the dashed line corresponds to the shift of the lattice. The bias voltage is 1.5 kV.

For small tilt angles ($\alpha < 1$ mrad) the output shift of all three beams depends approximately linearly on the tilt angle [Fig. 2.15(a)]. As the lattice tilt is increased, the steering of the two beams associated with the edges of the Bragg reflection gap eventually experiences saturation, as the probe beams approach propagation at the Bragg angle in the lattice (corresponding to an output shift of 76 μm). Fig. 2.15(b) shows the corresponding measured output intensity profiles of the three beams for a lattice tilt of 1.25 mrad. It is clearly seen that the selective excitation of each Bloch wave is extremely pure, and that the characteristic beam profiles [see Fig. 2.5] are preserved in the tilted lattice.

2.6.4 Tunable beam steering

In order to demonstrate tunability of the beam steering in a tilted lattice, we measure the change of the beam position at the crystal output face as a function of the crystal bias voltage. Figure 2.16(a) shows the output beam shift for the three different Bloch waves vs. the externally applied voltage, when the lattice is tilted 0.83 mrad inside the crystal. At low voltages (shallow lattice) beams corresponding to the bottom of the first band and the top of the second band experience strong steering in opposite directions, in agreement with the above findings [Fig. 2.15]. Increasing the voltage results in a monotonical decrease of the output shift for both beams, indicating a reduced beam mobility as a result of the stronger lattice and flattened transmission bands [cf. Fig. 2.12(b,c)].

The beam deflection can be almost entirely suppressed in a deep lattice, corresponding to voltages higher than 2.5 kV. For voltages lower than 1 kV, the lattice is too shallow and the Bragg reflection gap hence too narrow to allow for pure Bloch

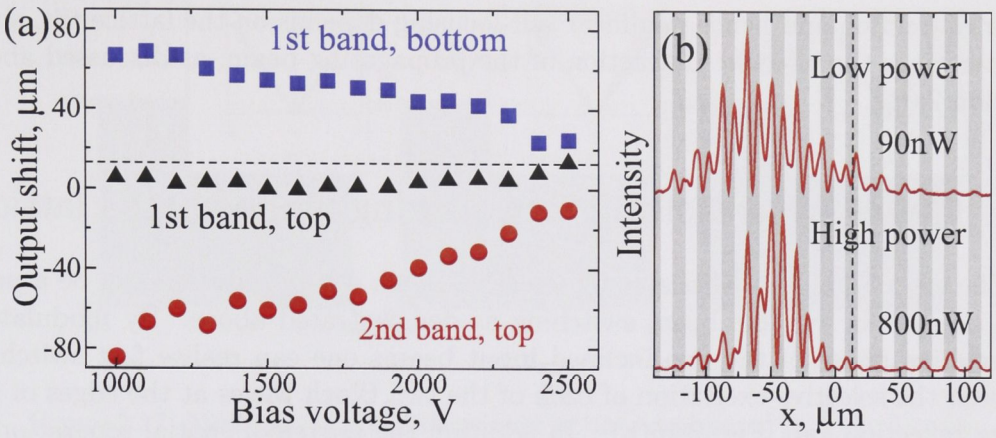

Figure 2.16: (a) Measured output shift vs. bias voltage at low power for beams corresponding to three different Bloch modes. The lattice tilt is 0.83 mrad inside the crystal. (b) Output beam intensity profiles (at 1.8 kV) corresponding to the top of the second band for low (top) and high (bottom) power. While preserving a strong beam steering, the FWHM of the beam is decreased from 81 μm in the linear regime (top) to 46 μm in the nonlinear regime (bottom) due to self-focusing. In (a,b) the dashed line indicates the shift of the lattice.

wave excitation at the two bandedges, given the spectral width of the finite beams. In contrast to the strongly voltage dependent steering of beams belonging to the edges of the Bragg reflection gap, the beam associated with the top of the first band is seen to be deflected less than the lattice itself, and this deflection does not change significantly with the voltage [Fig. 2.16(a), triangles].

In our experiment the probe beams experience only limited linear diffraction broadening upon propagation through the lattice, and the two strongly deflected beams associated with the edges of the Bragg reflection gap are spatially well separated at the crystal output, as shown in Fig. 2.15(b). As discussed above, self-focusing nonlinearity allows for self-trapping of the beams associated with the top of the first and second bands where diffraction is normal. The ability to steer nonlinear *self-trapped* beams could be important for practical beam switching applications where a high spatial resolution is required for extended propagation distances. It is therefore important to investigate experimentally whether beam steering is preserved in the nonlinear regime of propagation.

In Fig. 2.16(b) we show the experimental output intensity profiles of the deflected beam associated with the top of the second band, measured at low (90 nW) and high power (800 nW). The lattice tilt is 0.83 mrad and the bias voltage 1.8 kV. At higher laser power the beam self-focuses from an initial output FWHM of 81 μm in the linear regime to 46 μm in the nonlinear regime, with only a small decrease of the deflection angle (10 μm at the output) resulting from the beam self-action. We thus conclude that the strong steering of the second band beam is preserved in the nonlinear regime where self-trapping occurs. Finally we note that the degree of

linear diffraction and hence nonlinear self-focusing depends on the lattice tilt, since it determines the effective diffraction of the propagating beam, as discussed above [Section 2.6.2].

2.7 Optically controlled beam steering in modulated lattices

The steering of optical beams by selective Bloch wave excitation can be a powerful scheme for tunable beam switching as demonstrated above. By modulating the relative phase of the two inclined input beams one can realise fast switching between the selective excitation of each of the two Bloch waves at the edges of the Bragg reflection gap [Fig. 2.15(b)]. In addition the degree of spatial separation of the beams can be dynamically tuned by changing the bias voltage [Fig. 2.16(a)]. The tunable beam steering, however, is not effective for the beam associated with the Bloch wave at the top of the first band [cf. Fig. 2.16(a)], and it is therefore desirable to explore different ways of dynamically steering such beams.

In this Section we demonstrate a way to steer optical beams effectively in lattices which are *modulated* in the transverse and propagation directions by the introduction of a third lattice writing control beam [76]. This third beam propagating at a small angle with respect to one of the two lattice writing beams introduces a lattice asymmetry which can transfer transverse momentum to a simple Gaussian type probe beam. We present a detailed experimental study of optically controlled beam steering in such modulated lattices, and identify and characterise the key physical parameters governing the effect. We demonstrate that the beam steering can be tuned all-optically by varying the power of the third modulating lattice beam. Furthermore we observe that nonlinear self-focusing can compensate for diffraction while preserving the beam steering, thus allowing for increased spatial resolution of the effect for practical applications.

The transverse mobility of self-trapped beams in modulated lattices contrasts with the behaviour of strongly localised solitons in conventional lattices which tend to lock to straight propagation in a single waveguide due to the effect of the Peierls-Nabarro potential associated with the energy difference between on-site and off-site soliton states [34, 38]. Such effects, on the other hand, can be exploited in alternative schemes for realising power dependent beam steering in nonlinear lattices [34, 39, 107].

2.7.1 Three-wave modulated lattices

One-dimensional optical lattices created by two interfering plane waves are inherently symmetric in the transverse direction (x) and invariant in the propagation direction (z). Recent theoretical studies [108, 109] suggested a novel beam steering technique by considering the introduction of a third interfering wave which breaks the lattice symmetry and induces modulation along both x and z directions [see Fig. 2.17]. It was predicted that weak lattice modulation can induce a drift of broad solitons [108], and that binary switching can be obtained for strongly lo-

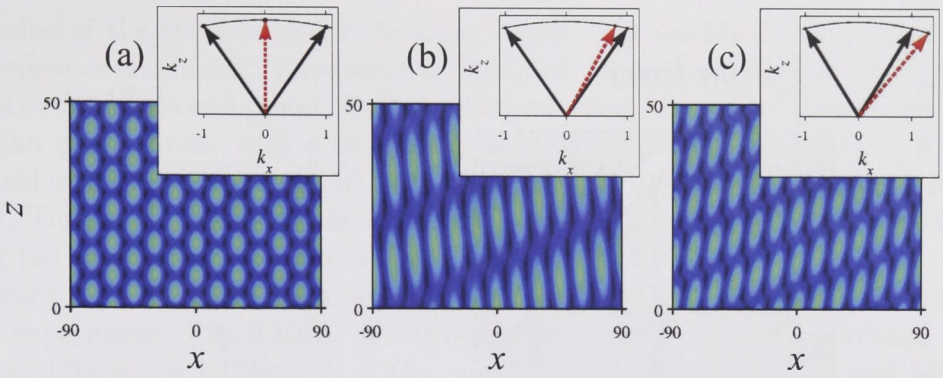

Figure 2.17: Examples of one-dimensional lattices modulated by a third beam with transverse wave number k_{3x} [from Ref. [109]]: (a) $k_{3x} = 0$, (b) $k_{3x} = 0.8k_{12x}$, and (c) $k_{3x} = 1.3k_{12x}$. Insets show the wave vectors of the two lattice beams (black) and the third modulating beam (red, dashed). Parameters are $A_{12} = 0.25$, $A_3 = 0.66A_{12}$ and the propagation length is 50 mm.

calised discrete solitons [109]. In this work we study an experimentally accessible case of moderate lattice strength and modulation, where a probe beam extends over a few lattice sites.

Similar to Refs. [108, 109], we consider a modulated lattice created by two waves with equal amplitudes A_{12} and opposite inclination angles defined by the transverse wavenumbers k_{12x} and $-k_{12x}$, and an additional third wave with amplitude A_3 and wavenumber k_{3x} [see Fig. 2.17]. In numerical simulations, we normalise the transverse x and propagation z coordinates to the characteristic scales x_0 and z_0, respectively. Then, the three-wave interference pattern is $I_p(x,z) = |A_L|^2$, where

$$A_L = A_3 \exp[i\beta_3 z + ik_{3x}x - i\varphi] + 2A_{12}\exp(i\beta_{12}z)\cos(k_{12x}x), \tag{2.4}$$

φ is the relative phase between the third wave and the two other waves, and the propagation constants $\beta_j = Dk_j^2$ define the longitudinal wavevector components. Here $D = z_0\lambda/(4\pi n_0 x_0^2)$ is the diffraction coefficient, n_0 is the average refractive index of the medium, and λ is the wavelength in vacuum.

As previously we model the propagation of an extraordinarily polarised probe beam by a parabolic equation for the normalised beam envelope $\psi(x,z)$, $i\partial\psi/\partial z + D\partial^2\psi/\partial x^2 + \mathcal{F}(x,z,I)\psi = 0$, where $\mathcal{F}(x,z,I) = -\gamma(I_b + I_p(x,z) + I)^{-1}$, I is the normalised probe beam intensity, I_b is the constant dark irradiance, $I_p(x,z)$ is the lattice interference pattern given by Eq. (2.4), and γ is the nonlinear coefficient proportional to the applied DC field. To match our experiments, we use the following parameters: $\lambda = 0.532\mu$m, $n_0 = 2.4$, $x_0 = 1\mu$m, $z_0 = 1$mm, $I_b = 1$, $\gamma = 2.36$, and $d = 20\mu$m is the period of the non-modulated lattice (for $A_3 = 0$). The crystal length is $L = 15$mm.

The experimental setup is similar to that used in the previous experiments [see Fig. 2.2] with an extension to the ordinarily polarised beam arm allowing for the

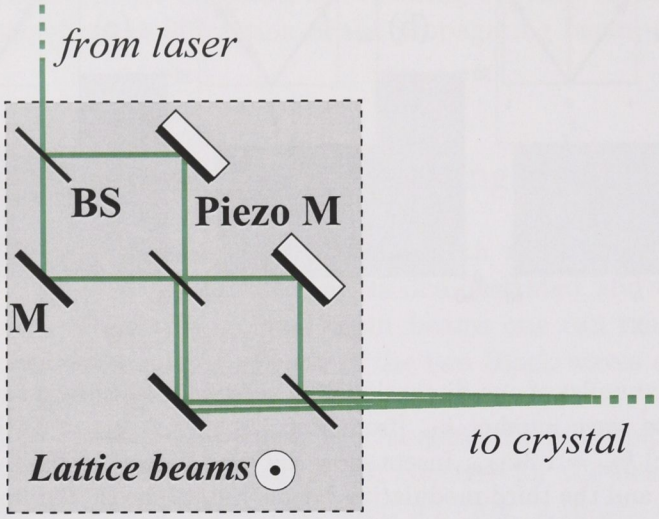

Figure 2.18: Schematic of the generation of three independent lattice beams in the modified interferometer arm of the experimental setup [cf. Fig 2.2].

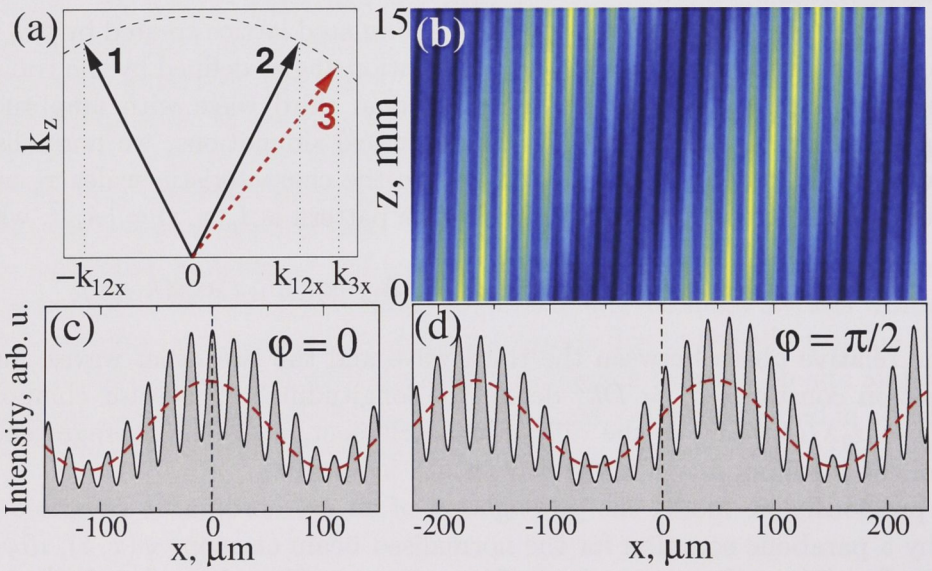

Figure 2.19: (a) Schematic k-vector configuration, and (b) two-dimensional plot of modulated lattice for $k_{3x} = 1.18k_{12x}$ and $I_3 = 4I_{12}$. Bottom: corresponding experimental lattice profiles measured at the crystal input ($z = 0$), when maximum of the broad transverse modulation (red-dashed) is (c) aligned with probe beam input ($x = 0$), and (d) offset by a quarter period.

generation of the third lattice modulating beam. The modified three beam lattice interferometer is schematically shown in Fig. 2.18. The setup allows for independent control of the phase and power of all the lattice beams. An extraordinarily polarised Gaussian probe beam with a full width at half maximum (FWHM) of 25μm is launched into the crystal, parallel to the z axis ($k_x = 0$). The crystal bias voltage is 2.2 kV. The input positions of lattice fringes and probe beam is carefully monitored during the experiment, and the latter is fixed at $x = 0$.

Figure 2.19 shows an example of the geometry of the modulated lattice used in the experiment. Fig. 2.19(b) is a two-dimensional plot of the modulated lattice calculated for $k_{3x} = 1.18k_{12x}$, $I_3 = 4I_{12}$, and $\varphi = \pi/2$. Figures 2.19(c) and (d) show the experimentally measured transverse lattice intensity profiles at the input for $\varphi = 0$ and $\varphi = \pi/2$, respectively. Changing the phase of the third beam φ causes the whole lattice pattern to shift in both transverse and longitudinal directions. The lattice geometry also depends on the inclination angle and power of the third beam, characterised by the parameters k_{3x}/k_{12x}, and I_3/I_{12}, where $I_3 = |A_3|^2$ and $I_{12} = |A_{12}|^2$ are the normalised intensities of the lattice beams.

A transverse lattice symmetry is recovered when $k_{3x} = 0$ or $k_{3x} = \pm k_{12x}$. In all other cases, the modulation is asymmetric, and steering of the normally incident probe beam becomes possible. We determine experimentally that, due to the finite trapping strength of the lattice, steering without strong beam reshaping or break-up is possible for a limited parameter range $0.8 < k_{3x}/k_{12x} < 1.2$. Below we discuss in further detail the case $k_{3x} > k_{12x}$, noting that the steering behavior in the complementary regime $k_{3x} < k_{12x}$ is similar.

2.7.2 Influence of phase and angle of the modulating wave

First we characterise the effect of the modulated lattice geometry on the propagation of a low power ($\sim 25nW$) probe beam in the linear regime for three different angles of the modulating beam, in the case of strong lattice modulation, $I_3 = 4I_{12}$. In Fig. 2.20(a) we plot the shift of the beam center of mass vs. the modulating beam phase φ [see Fig. 2.19(c,d)]. Solid lines represent smoothing spline fitting to the data points [experimental uncertainty in the vertical direction is approximately 10μm in Fig. 2.20(a), and up to 20μm in Fig. 2.20(b)]. For $k_{3x} = 1.01k_{12x}$ the beam shift is virtually zero throughout the entire phase scan [stars in Fig. 2.20(a)]. The insensitivity to φ results from the lattice being fully symmetric when beams 2 and 3 in Fig. 2.19(a) are parallel ($k_{3x} = k_{12x}$).

On the other hand, as the angle of the third lattice-forming wave is increased, the lattice becomes asymmetrically modulated, and the beam shifts to one or the other side [squares and circles in Fig. 2.20(a)], depending strongly on the value of φ (similar behavior was observed for $k_{3x} < k_{12}$). The observed features were confirmed by numerical simulations (not shown), and they prove that not only the local asymmetric distortion of the lattice, which in this case tends to shift the beam towards positive x [see Fig. 2.19(b)], but also the broader effective modulation geometry plays an important role for the beam propagation dynamics. We further note that in Fig. 2.20(a) the beam shift is not symmetric with respect to $x = 0$, and

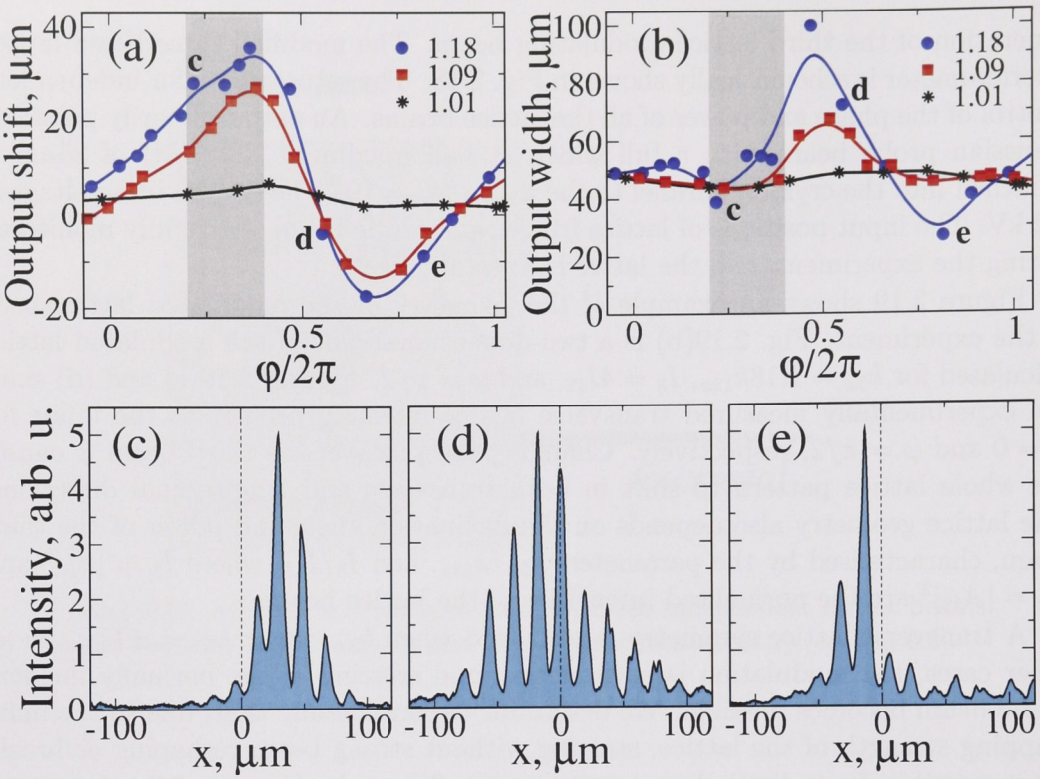

Figure 2.20: (a,b) Measured shift and width of a linear probe beam output vs. the phase of the modulating lattice beam for three different values of k_{3x}/k_{12x}, for $I_3 = 4I_{12}$. Shading marks the region in which the figure of merit is maximised. (c-e) Examples of measured output profiles corresponding to the points (c,d,e) in the plots (a,b).

it is strongest in the region $0 < \varphi < \pi$ where the effects of local and broad lattice modulation pull the beam in the same direction.

Figure 2.20(b) maps the corresponding output beam width (FWHM of Gaussian fit) as a function of φ. Again, the case $k_{3x} = 1.01k_{12x}$ proves to be relatively insensitive to the phase shift, whereas for larger angles, substantial beam broadening is observed close to $\varphi = \pi$. For $k_{3x} = 1.18k_{12x}$, the maximum output beam width greatly exceeds that of a diffracting beam in the absence of a lattice (57μm), and the observed broadening is attributed to the geometry of the modulated lattice, and not solely to the decreased contrast of the lattice at $\varphi = \pi$ [see Fig. 2.19]. We note that when the phase φ is scanned from zero to 2π, the local input beam excitation symmetry changes from on-site to off-site and back, and this may in principle lead to additional beam steering [34]. However, we verified that under our experimental conditions the contributions to center of mass shift as well as beam broadening due to this effect are negligible ($< 3\mu$m in both cases). Examples of output beam profiles corresponding to points c, d and e in Figs. 2.20(a,b) are shown in Figs. 2.20(c-e).

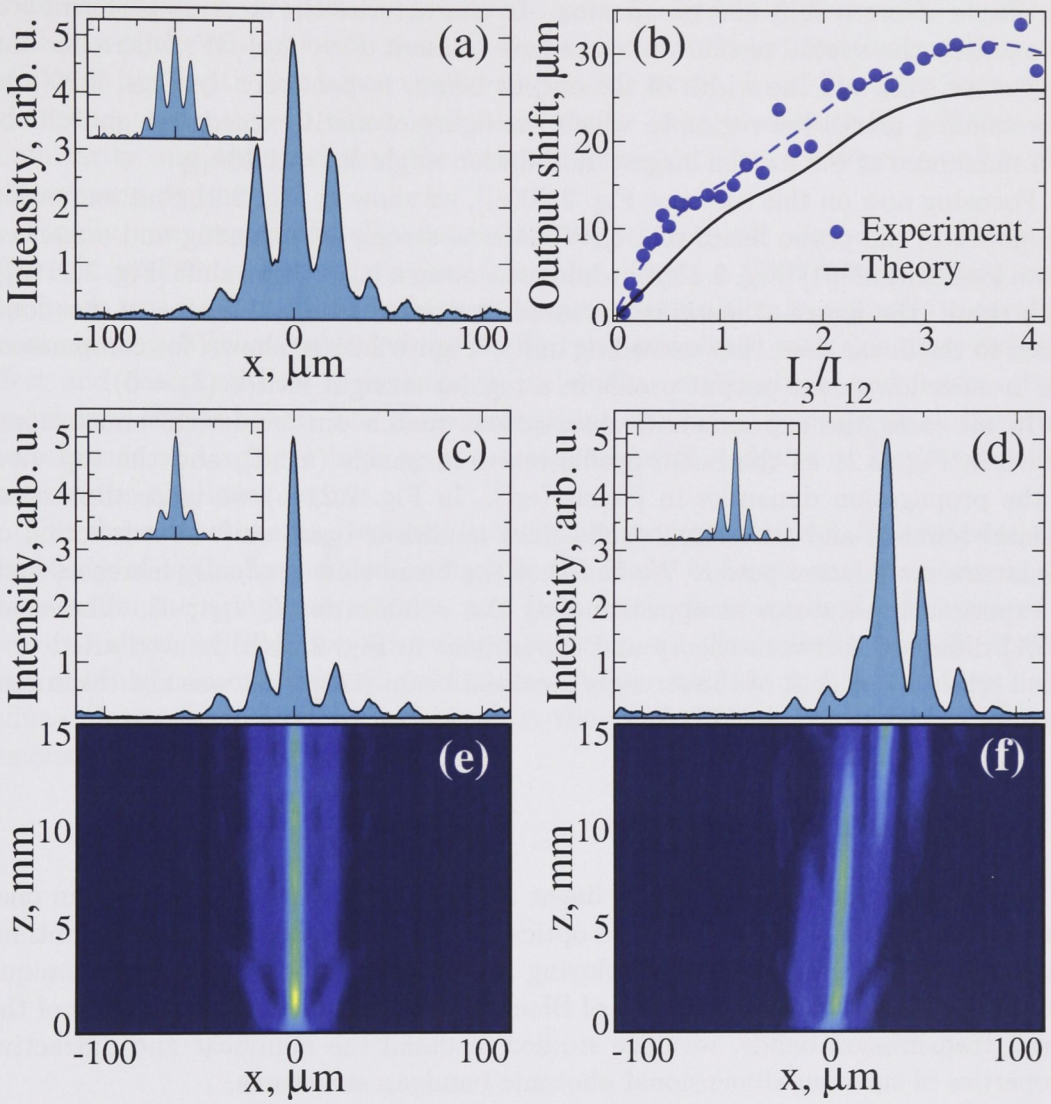

Figure 2.21: (a) Experimental and theoretical (inset) linear output in a straight lattice ($I_3 = 0$). (b) Shift of the nonlinear probe beam output vs. the modulating beam power for $k_{3x} = 1.18k_{12x}$ and $\varphi/2\pi = 0.22$. (c,d) Experimental and theoretical (inset) nonlinear output in straight and modulated lattices for $I_3 = 0$ and $I_3 = 4I_{12}$, respectively, and $k_{3x} = 1.18k_{12x}$. (e,f) Numerical simulations of the longitudinal propagation.

2.7.3 Steering of self-trapped beams

The angle and phase of the modulating beam are important control parameters, and for practical applications it is necessary to realise an optimal balance between the effects of beam shift and broadening. To characterise the steering performance, we quantify the spatial resolution by a figure of merit $F = |\Delta x| / W$, where Δx and W are the shift and the width of the output beam, respectively. In Figs. 2.20(a,b) grey shading marks the region in which the figure of merit exceeds 0.5 and climbs to a maximum of 0.6 for the largest modulation angle $k_{3x} = 1.18 k_{12x}$.

Focusing now on this case [see Fig. 2.20(c)], we show in Fig. 2.21 that increasing the power of the probe beam to 1.5μW leads to strong self-focusing and enhanced beam localisation [61] [Fig. 2.21(c)] while preserving a large beam shift [Fig. 2.21(d)]. As a result, the figure of merit is increased by approximately a factor of two compared to the linear case, thus exceeding unity. Figure 2.21(a) shows, for comparison, the broader low power output profile in a regular straight lattice ($I_3 = 0$).

In all cases the experimental observations match our numerical simulations, shown in Fig. 2.21 as the beam profile insets in panels (a,c,d), and the top view of the propagation dynamics in panels (e,f). In Fig. 2.21(b) we trace the experimental (circles) and theoretical (solid line) nonlinear beam shift as a function of the lattice modulation power. We find that the beam shift gradually increases and, in experiment, saturates at approximately $\Delta x = 30\mu$m for $I_3/I_{12} > 3$. The small (15%) difference between theory and experiment in Fig. 2.21(b) is attributed to a small self-induced drift of the strongly localised beam [110], that was not taken into account in simulations.

2.8 Summary

In this Chapter we have studied linear and nonlinear beam propagation in one-dimensional photonic lattices induced optically in a biased photorefractive strontium barium niobate (SBN) crystal. Employing a multiple beam experimental technique which allows for selective excitation of Bloch waves associated with the edges of the linear transmission bands, we have studied in detail the nonlinear and diffractive properties of such one-dimensional photonic bandgap structures.

We have studied the *nonlinear interaction* of mutually incoherent co-propagating beams originating from different spectral bands, in a straight lattice with self-focusing nonlinearity. We have demonstrated experimentally how lattice defects induced by nonlinear propagation can trap simultaneously beams from different transmission bands, leading to discrete interband mutual focusing, which is a fundamental effect and a key physical mechanism for the generation of multi-gap vector solitons. We have observed a fundamental asymmetry in the mutual focusing effect due to the generically different physics and localisation mechanisms of the involved Bloch waves. We also demonstrated an interplay between waves with diffraction coefficients of opposite sign that leads to complex beam reshaping, and simultaneous focusing and defocusing of beams within the first transmission band.

We have studied theoretically and demonstrated experimentally strong beam

steering in *tilted* optically induced lattices, where selective Bloch wave excitation allows for switching between spatially separated output beams which refract in different directions in the structure. The origin of the beam steering is the strongly modified diffractive properties of waves in periodic bandgap structures. Dynamic tunability of the output beam position was demonstrated by electro-optically varying the lattice depth and hence the linear bandstructure. In addition we have studied beam propagation in tilted lattices at higher laser intensities for self-focusing nonlinearity and observed that the beam steering properties are preserved in the self-trapping regime.

Finally, we experimentally demonstrated steering of nonlinear self-trapped beams in *modulated* optically induced lattices, where a third lattice writing control beam was used to induce a lattice asymmetry resulting in optically controlled beam steering. We have revealed the key features associated with this beam steering effect and described how it depends on inclination angle, phase, and power of the modulating lattice beam. The characterisations allowed us to optimise the steering performance and achieve high spatial resolution with a figure of merit exceeding unity in the nonlinear regime.

The three experiments described in this Chapter together have demonstrated the versatility of optically induced lattices in the study of linear and nonlinear beam propagation in periodic structures, and have furthermore realised and explored a series of novel schemes for achieving nonlinear and dynamically tunable spatial control of light in one-dimensional lattices. As we shall see in Chapter 4 optically induced lattices can also be employed in the study of light propagation in two-dimensional periodic structures.

CHAPTER 3

Discrete self-trapping in defocusing waveguide arrays

3.1 Introduction

The optically induced lattices discussed in the previous Chapter constitute a powerful experimental platform for fundamental studies of linear and nonlinear light propagation in periodic structures. The dynamic tunability and possibility for structural reconfiguration offered by this type of system, as well as the access to strong nonlinearity at continuous-wave laser powers, represent invaluable and unique experimental advantages. However, the price paid for this is a complex and bulky experimental setup which is sensitive to mechanical disturbances, and which makes transfer of acquired fundamental knowledge to applied technologies a major challenge.

On the other hand, *fabricated* nonlinear periodic structures based on planar integrated optics hold greater promise for practical application in e.g. optical signal processing microphotonic circuits and devices for optical communication systems. Fabricated structures provide minituarisation of the experimental setup, better stability, and potentially easier integration in optical systems. A host of mature technologies exist for the fabrication of high quality photonic structures on planar wafer substrates, in a number of different optical material systems including glasses, semiconductors, and polymers.

One-dimensional arrays of evanescently coupled waveguides are prime examples of periodic structures fabricated in planar geometries, and they have already been succesfully used in many pioneering experimental studies of both linear and nonlinear discrete phenomena (see e.g. Ref. [10]). Indeed, the capabilities of planar waveguide fabrication technology was an important inspirational factor leading to the theoretical prediction [12] and the first observation [33] of discrete spatial solitons one and two decades ago, respectively [cf. Section 1.9].

From a general point of view, planar waveguide arrays and one-dimensional optically induced lattices represent equivalent physical systems, and they can therefore

be used in similar experimental studies of fundamental wave propagation effects in periodic structures, including linear and nonlinear spatial light control through e.g. diffraction management and self-trapping. In many cases, however, fabricated structures do not offer tunability and nonlinearity at moderate optical intensities. The latter limitation in particular represents a major practical issue. It is therefore interesting to identify experimental systems that allow to combine high quality fabricated structures with tunability and a strong nonlinear response.

In this Chapter we study linear and nonlinear light propagation in one-dimensional waveguide arrays fabricated in lithium niobate ($LiNbO_3$) crystals. The $LiNbO_3$ crystal exhibits a strong photorefractive nonlinearity which, as in the case of optically induced lattices, allows for the observation of nonlinear effects such as beam self-trapping at sub-milliwatt power levels at visible wavelengths. Although not exploited in this work, the $LiNbO_3$ material system offers the additional possibility of external electro-optic tuning of the integrated photonic structures by incorporation of electrodes on top of the planar wafers.

The nonlinearity in $LiNbO_3$ exploited here is of the *self-defocusing* type, and this brings novel opportunities for the study of nonlinear beam localisation. In particular, self-trapping inside the Bragg reflection gap of beams originating from the first transmission band can be studied in this experimental setting [cf. Section 1.8]. Beam self-trapping in self-defocusing nonlinear media is a highly nontrivial effect, which indeed is counter-intuitive from the point of view of light propagation in bulk materials [cf. Sections 1.5 and 1.6]. It is therefore interesting to study in further detail the regime of validity of the self-trapping scenario predicted for discrete systems with self-defocusing nonlinearity [see Section 1.7.2], and to link it with the comprehensive description of continuous systems based on the nonlinear Schrödinger equation [Eq. (1.8)] and the Bloch wave formalism [see Section 1.7.4].

In Section 3.3 we study the crossover from self-defocusing in continuous and weakly modulated systems to discrete self-trapping in photonic lattices with self-defocusing nonlinearity [13], and demonstrate experimentally that strongly localised gap solitons can be excited by a single narrow Gaussian beam in waveguide arrays exhibiting a high degree of discreteness [77]. Our study offers new insight into the physics of discrete nonlinear light localisation, and furthermore provides a new experimental scheme for excitation of staggered solitons which is efficient and more practical than e.g. the two-beam Bloch wave matching method used above in Chapter 2.

In addition, fabricated waveguide arrays offer novel opportunities for studying boundary or *surface* effects near the edges of periodic structures. This area of research recently experienced a considerable surge of interest sparked by the theoretical prediction [111] and first experimental observation [112] of discrete surface solitons, i.e. self-trapped beams located at photonic lattice interfaces. Similar to the case of extended periodic structures, in-phase surface solitons exist in waveguide arrays with self-focusing nonlinearity. In Section 3.6 we present the experimental observation and detailed study of out-of-phase surface gap solitons at the edge of a semi-infinite $LiNbO_3$ waveguide array with self-defocusing nonlinearity [78].

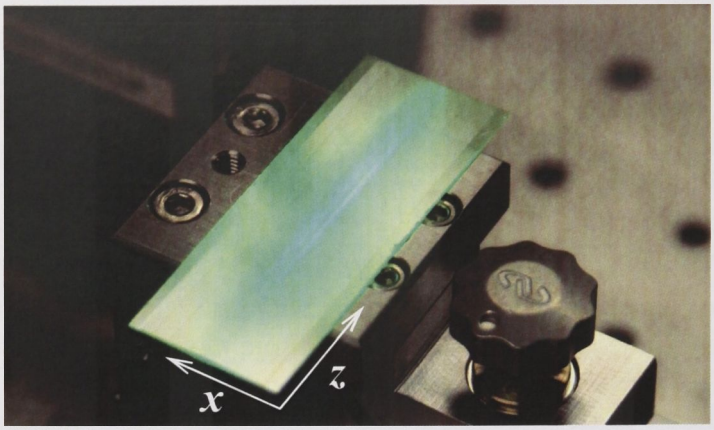

Figure 3.1: Photograph of a mono-crystal $LiNbO_3$ sample with waveguide arrays produced by titanium in-diffusion. The transverse direction x and the longitudinal propagation direction z are indicated by arrows.

3.2 Lithium niobate waveguide arrays

The waveguide arrays used in our studies are produced by a common technique based on titanium in-diffusion into a mono-crystal lithium niobate wafer. In the fabrication process, 100Å of Ti is deposited on an X-cut $LiNbO_3$ wafer using electron beam evaporation. The Ti layer is photolithographically patterned and etched in a buffered hydrofluoric acid solution. The diffusion is conducted at 1050°C for 3 hours in a wet oxygen environment. The produced waveguides are single mode, which is verified using a prism coupling technique. Finally the samples are diced to a length of 50 mm and both facets mechanically polished.

The fabrication process results in a structure containing a number of high quality waveguide arrays with a total of 100 waveguides in each. Figure 3.1 shows a photograph of a sample illuminated with green laser light. The waveguide spacing (lattice period) is $d = 19\,\mu$m and $d = 9\,\mu$m in the two particular arrays used in Section 3.3 and Section 3.6, respectively. The depth of the refractive index modulation is approximately $\Delta n = 3 \times 10^{-4}$, in both of the above cases exceeding the threshold required for discrete self-trapping by single-site excitation [cf. Section 3.3 below].

In $LiNbO_3$ strong internal drift associated with the *photovoltaic* effect leads to a *self-defocusing* type photorefractive nonlinearity [31]. In this case large space-charge fields and a strong electro-optic response can be achieved for extraordinarily polarised light even without an externally applied field [cf. Section 1.3], and in the experiments described in this Chapter we thus operate with an unbiased $LiNbO_3$ crystal. Asymmetry effects associated with the internal drift nonlinearity are strongly limited by the discreteness of the fabricated waveguide structure which effectively prevents beam self-bending in the periodic potential.

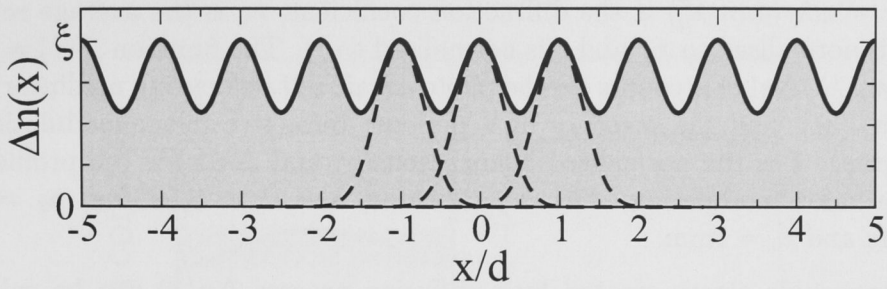

Figure 3.2: Refractive index change, normalised to the modulation depth ξ, vs. transverse position in $LiNbO_3$ waveguide array, normalised to the lattice period d. The sum of individual diffusion profiles (dashed) result in an effective sinusoidal refractive index modulation (solid).

3.3 Crossover from defocusing to discrete self-trapping

In homogeneous bulk media self-defocusing nonlinearity always leads to enhanced beam broadening, as discussed in Section 1.5. In the framework of the discrete waveguiding model introduced in Section 1.7.1, on the other hand, self-defocusing nonlinearity allows for self-trapping of light to occur in periodic structures in the form of out-of-phase or *staggered* solitons. In Section 1.8 it was shown that in a more comprehensive continuous description such staggered solutions appear as gap solitons residing in the first Bragg reflection gap of the linear transmission spectrum.

The discrete waveguiding model [Eq. (1.11)] predicting a universal self-trapping scenario for both self-focusing and self-defocusing nonlinearities is valid when the optical field can be represented as a superposition of weakly overlapping modes of the individual lattice sites. This condition is generally satisfied when the refractive index contrast in the periodic structure is sufficiently large [113]. However, in the case of self-defocusing nonlinearity the nonlinear dynamics changes dramatically for smaller index contrast. Indeed, if the lattice modulation is absent or very weak, beams are expected to experience self-defocusing rather than self-trapping, i.e. the exact opposite behaviour. It is therefore interesting to study the crossover between the two qualitatively different regimes of self-defocusing in the bulk and in weak lattices, and discrete self-trapping in stronger lattices.

3.3.1 Numerical simulations

In order to study the crossover between beam self-defocusing and discrete self-trapping we model the beam propagation using a normalised continuous nonlinear Schrödinger equation for the slowly varying field envelope $\psi(x, z)$ [see Section 1.2.6],

$$i\frac{\partial\psi}{\partial z} + D\frac{\partial^2\psi}{\partial x^2} + \mathcal{F}(x, I)\psi = 0, \tag{3.1}$$

where $D = z_0\lambda/(4\pi n_0 x_0^2)$ is the diffraction coefficient, n_0 is the average refractive index, x is normalised to x_0, and z is normalised to z_0. The function $\mathcal{F}(I) = 1.5(1+I)^{-1}+(2\pi z_0/\lambda)\Delta n(x)$ accounts for the photovoltaic self-defocusing nonlinearity (the first term) [31], and the presence of a periodic refractive index modulation (the second term). I is the normalised beam intensity, and $\Delta n(x)$ is the profile of the refractive index modulation. Other parameters are: $\lambda = 0.532\mu$m, $n_0 = 2.234$, $x_0 = 1\mu$m, and $z_0 = 1$mm.

For waveguide arrays created by a diffusion process $\Delta n(x)$ can be calculated as $\Delta n(x) = \xi \sum_m \exp[-(x - m\ d)^2/w^2]$, i.e. a sum of Gaussian contributions from individual sites, where $m = 0, \pm 1, \pm 2$, etc. denotes the waveguide number, ξ defines the modulation depth, d is the waveguide spacing (lattice period), and w is a characteristic width defined by the diffusion process and the window in the photolithographic mask. If the individual diffusion profiles overlap as shown in Fig. 3.2 the combined refractive index modulation $\Delta n(x)$ is essentially sinusoidal with an effective modulation depth smaller than ξ. Here we take the values of characteristic diffusion width $w = 8\mu$m and waveguide spacing $d = 19\mu$m, and then the effective depth of the refractive index modulation is $\Delta n = 0.442\ \xi$. We note that the results presented below are general and do not depend on the particular refractive index profile defined by the experimental system.

Figures 3.3(a,b) present the calculated bandgap spectrum for the waveguide array for two values of the refractive index contrast. The calculations confirm that increasing the lattice contrast leads to wider bandgaps due to stronger Bragg reflections [cd. Section 1.7.4]. As discussed in Section 1.8 the finite width of the Bragg reflection gap limits the minimum width of self-trapped beams. Figures 3.3(c,d) show the profiles of the gap solitons of minimum width corresponding to the cases in Figs. 3.3(a,b). The width of the gap is smaller for weaker refractive index contrast, and correspondingly the minimum soliton width is larger. The calculated minimal width of the gap soliton, $W = 3\int |x||\psi|^2 dx / \int |\psi|^2 dx$, is plotted in Fig. 3.3(e) versus the refractive index contrast. In the case of small refractive index modulation and a narrow bandgap, the narrowest soliton spans several waveguides. On the other hand, when the lattice contrast increases, the bandgap widens, and the narrowest soliton is localised at a single waveguide.

We study the crossover to discrete self-trapping by modeling the linear and nonlinear propagation of an input Gaussian beam of a width equal to the size of a single waveguide, or lattice site. To characterise the self-trapping efficiency for different lattice depths, we calculate the relative power that remains in the central section of the array after propagation over a distance of many diffraction lengths (1000mm) as a function of the depth of the refractive index modulation. The result is shown in Fig. 3.4, where the central section of the array is defined as the region containing 20 waveguides (implemented with absorbing boundary conditions). We investigate the effect of nonlinear self-action (solid curve) on the propagation dynamics with respect to linear diffraction (dashed curve). In the calculation represented by the solid curve in Fig. 3.4, the power of the input beam is optimised in order to maximise the power fraction which remains in the central region of the array.

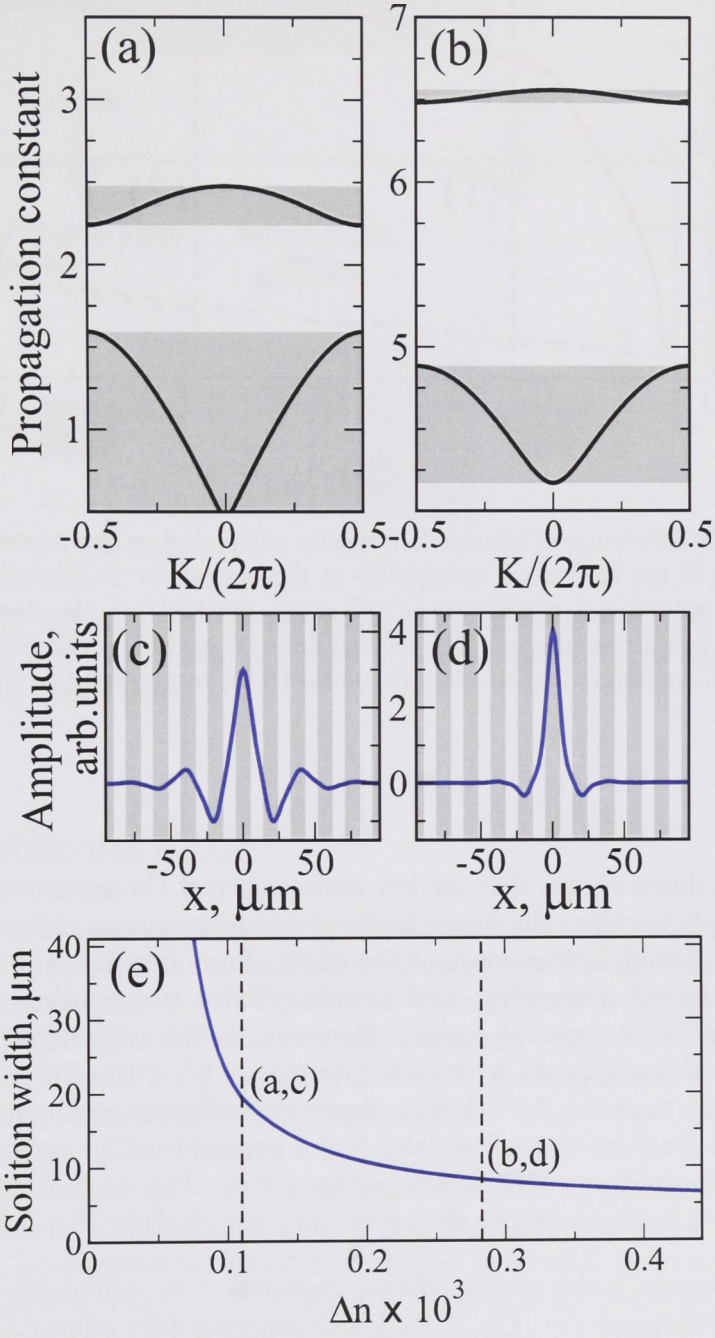

Figure 3.3: (a,b) Bandgap spectrum of linear waves for a refractive index modulation depth Δn of 1.1×10^{-4} and 2.8×10^{-4}, respectively. (c,d) Profiles of staggered gap solitons having the minimum width for cases (a,b), respectively. Shading marks index maxima. (e) Minimum width of the gap soliton vs. the depth of the refractive index modulation.

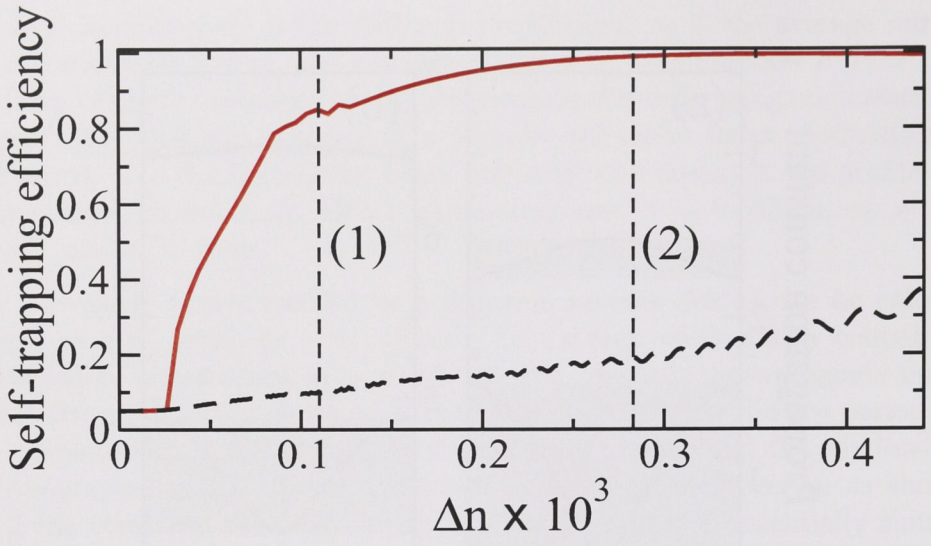

Figure 3.4: Efficiency of beam self-trapping calculated as the power fraction remaining in the 20 central waveguides at the output for an optimised input power (solid) compared with linear diffraction (dashed) vs. the depth of the refractive index modulation. The dashed lines (1) and (2) mark the modulation depth corresponding to cases (a,c) and (b,d), respectively, in Fig. 3.3.

The results demonstrate that for low index contrast the optimisation of the input power simply matches the linear limit, and the two curves coincide in Fig. 3.4. In this regime of weak lattice contrast the effect of nonlinearity is to increase beam spreading due to self-defocusing, and therefore linear propagation maximises the amount of light in the central region. However, as the refractive index modulation increases, there appears a sudden bifurcation from the linear regime. The abrupt transition occuring for a lattice depth exceeding approximately 0.3×10^{-4} corresponds to the formation of initially broad gap solitons, in agreement with the limitation on the soliton width shown in Fig. 3.3(e). The vertical dashed lines (1) and (2) in Fig. 3.4 correspond to the cases (a,c) and (b,d) in Fig. 3.3, respectively.

As the minimum width of the soliton decreases and approaches that of a single waveguide for larger Δn [Fig. 3.3(e)], self-trapping with almost 100% efficiency becomes possible [Fig. 3.4], as predicted by the discrete model [Eq. (1.11)]. The features shown in Fig. 3.4 represent a comprehensive picture of the qualitative crossover from self-defocusing to discrete self-trapping as the index contrast exceeds a certain threshold. In the region where single-site localisation is possible, and the self-trapping efficiency approaches unity, the system effectively behaves as a discrete system. Note that linear diffraction is gradually reduced due to waveguiding and decreasing inter-site coupling in an increasingly stronger lattice, resulting in a steady rise of the dashed curve in Fig. 3.4 for larger Δn.

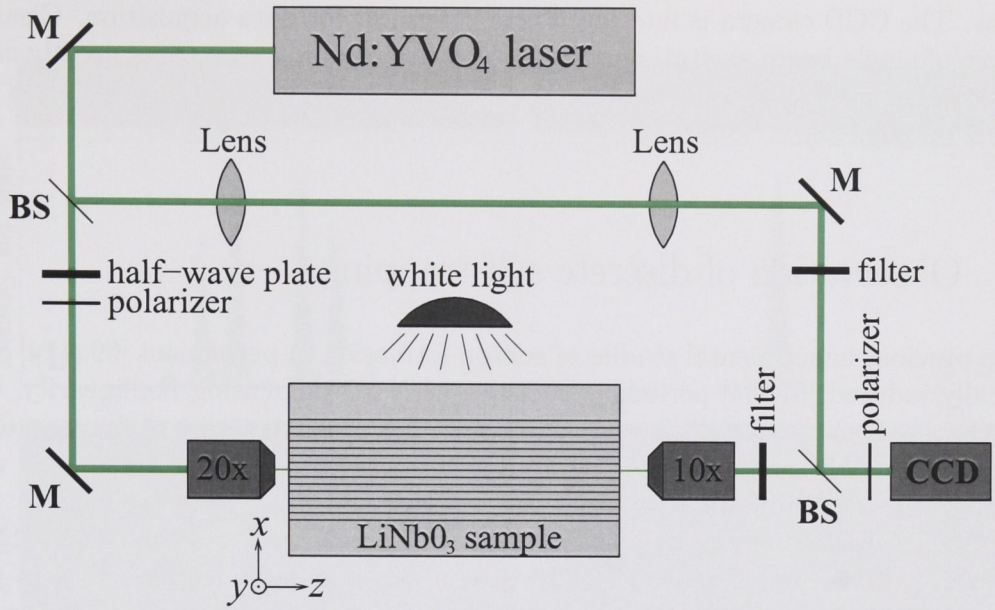

Figure 3.5: Schematic of the experimental setup for the study of discrete diffraction and gap soliton formation in a $LiNbO_3$ waveguide array. M - *mirror*, BS - *beam splitter*.

3.4 Experimental setup

The setup used in the experiments described throughout this Chapter is schematically shown in Fig. 3.5. An extraordinarily polarised laser beam from a frequency-doubled continuous-wave Nd:YVO_4 laser at $\lambda = 532\,\text{nm}$ is tightly focused by a microscope objective ($20\times$) and injected into a single channel of a planar $LiNbO_3$ waveguide array. The $LiNbO_3$ sample is mounted on a three-axis translation stage which allows for precise alignment in the transverse (x), vertical (y), and longitudinal (z) directions. The c-axis of the crystal is parallel to the transverse beam direction x. The full width at half maximum (FWHM) of the input beam is $3\,\mu\text{m}$ which provides a good match to the individual waveguide modes. At the output of the sample the propagated wavepacket is imaged onto a CCD camera by a second microscope objective ($10\times$). The charge mobility and hence the response time associated with the photovoltaic nonlinearity is controlled by a variable intensity white light illumination above the $LiNbO_3$ sample.

In order to perform interferometric measurements of the phase structure of the output probe beam, a plane wave reference beam is split off from the main beam and passed through a pair of lenses which allow for adjusting the beam divergence to match that of the output probe beam. The reference beam is recombined with the probe beam using a beam splitter and the two beams are imaged together onto the CCD camera. A half-wave plate and a polariser, as well as a number of neutral density filters throughout the setup, allow for adjusting the power of the individual

beams. The CCD camera is interfaced to a computer for data acquisition. Clearly, the use of single beam excitation and fabricated waveguide structures greatly simplifies the experimental setup compared to the case of optically induced lattices [cf. Fig 2.2 on page 38].

3.5 Observation of discrete self-trapping

In previous experimental studies of soliton formation in permanent [69, 114] and optically induced [61, 64] periodic structures with self-defocusing nonlinearity, the input excitation was specially prepared to reflect the phase structure of the staggered solitons, where the neighboring sites are out-of-phase [see Figs. 3.3(c,d)]. This was achieved either by illuminating the structure with a single beam inclined at the Bragg angle [61, 64, 69] or by spatial phase modulation of the initial beam [114]. However, observation of soliton localisation close to a single lattice site was not reported. In this Section we demonstrate experimentally discrete self-trapping by single-site excitation, which as shown in the numerical study above is possible in lattices exhibiting a high degree of discreteness.

At low laser power (~10 nW) the propagating beam experiences typical discrete diffraction, where at the array output most of the power is transferred into the neighboring waveguides and almost no light remains in the central guide [Fig. 3.6(a)]. The resulting intensity profile shown in Fig. 3.6(b, solid curve) matches the results of numerical simulations performed using the discrete model [Eq. (1.11)] (crosses) and the continuous model with periodic refractive index modulation [Eq. (3.1)] (green shading) with excellent accuracy. The corresponding calculated propagation inside the array is depicted in Fig. 3.6(c). When the laser power is increased (1 mW) the self-defocusing nonlinearity leads to strong beam localisation at a single waveguide [Fig. 3.6(d-f)], in a similar way as in self-focusing waveguide arrays, due to the universal nature of discrete self-trapping. In this case the localisation time is less than ten seconds.

In order to confirm that the self-trapped wave is indeed localised inside the Bragg reflection gap, and not in the total internal reflection gap, it is important to verify its staggered phase structure. The alternating phase of the field lobes of the localised beam reflects the fact that the in the nonlinear regime the propagation constant lies within the photonic bandgap at the edge of the first Brillouin zone. For the purpose of verifying this we allowed for saturation of the camera in order to detect the small but nonzero amount of light in the neighboring waveguides [cf. Fig. 3.3(d)]. The corresponding images are shown in Fig. 3.7 where the two neighboring satellites are clearly visible. They are separated from the central waveguide by vertical lines of strictly zero intensity [Fig. 3.7(a)], which is an indication of their staggered phase structure. To further confirm this observation, we interfere the output beam with an inclined broad reference beam. The corresponding interferogram is shown in Fig. 3.7(b), where a half period shift of the interference fringes at the zero intensity lines, corresponding to a π phase jump in the probe beam, is clearly observed.

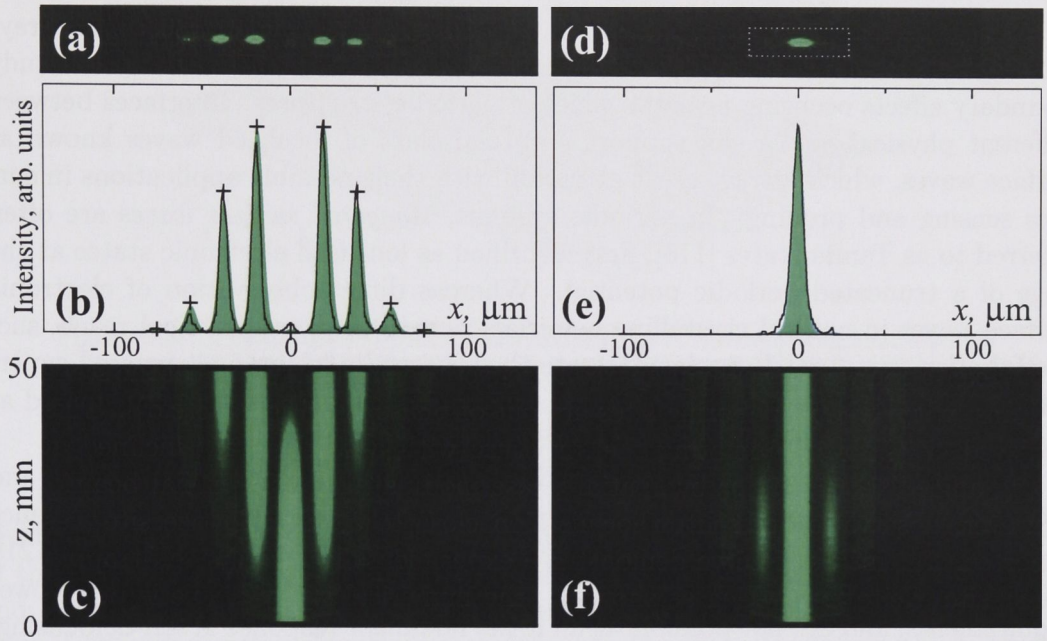

Figure 3.6: (a) Intensity distribution at the output facet of a $LiNbO_3$ waveguide array for linear propagation at low laser power (10 nW). Only the central waveguide is excited at the input. (b) Corresponding intensity profiles: Solid – experimental measurement; shading – numerical solution of the continuous model [Eq. (3.1)]; crosses – lattice site amplitudes calculated from the discrete model [Eq. (1.11)]. (c) Evolution of the beam intensity along the sample for a low input power simulated with Eq. (3.1). (d-f) Same as (a-c) for nonlinear propagation at high laser power (1 mW).

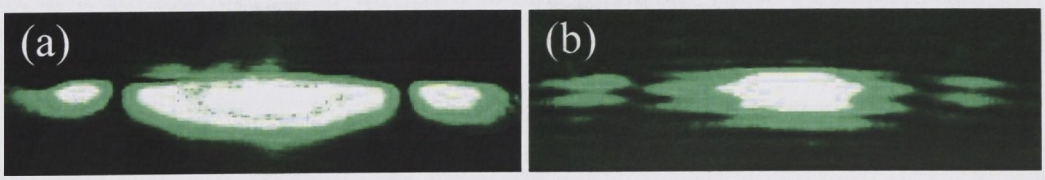

Figure 3.7: (a) Saturated camera image of the single channel localised state at the output of the array, zoomed at the dashed rectangle in Fig. 3.6(d). White areas correspond to saturated pixels. (b) Interferogram confirming the staggered phase structure of the output beam [cf. Fig. 3.3(d)].

3.6 Nonlinear surface waves

As mentioned in the introduction to this Chapter, fabricated waveguide arrays with finite extent in the transverse direction introduce the opportunity to study boundary effects occuring near the edges of periodic structures. Interfaces between different physical media can support a special class of localised waves known as surface waves, which attract great attention with their possible applications in surface sensing and probing. In periodic systems, *staggered surface waves* are often referred to as Tamm states [115], first identified as localised electronic states at the edge of a truncated periodic potential. Whereas direct observation of electronic surface waves in natural crystalline materials remains beyond practical reach, successful efforts were made to demonstrate their existence in nano-engineered superlattices [116]. In optics, linear staggered surface modes have been demonstrated at surfaces separating periodic and homogeneous dielectric media [117, 118].

Nonlinear surface waves have been widely studied in different fields of physics and most extensively in optics. A self-focusing optical nonlinearity enables the existence of self-trapped waves at interfaces between homogeneous dielectric media [119–121]. However, such nonlinear surface waves are typically associated with high power requirements, and are not possible at all if the nonlinear response is self-defocusing. The combination of periodicity and nonlinearity allows to overcome both of these limitations due to the ability of periodic structures to dramatically modify beam diffraction. This leads to a wealth of different types of modes localised at and near the surface [122].

Self-trapping of light near the boundary of a *self-focusing* photonic lattice was recently predicted [111] and demonstrated in experiment [112] through the formation of *discrete surface solitons* at the edge of a nonlinear waveguide array. In *self-defocusing* materials the existence of *surface gap solitons* at the interface between a uniform and a periodic medium was also suggested [111] and theoretically described [123]. In this case localisation occurs inside the photonic bandgap in the form of staggered surface modes. This enables one to extend the analogy with the localised electronic Tamm states into the nonlinear regime, so the surface gap solitons can be termed nonlinear Tamm states.

In this Section we study the self-action of a narrow beam propagating near the edge of a $LiNbO_3$ waveguide array with self-defocusing nonlinearity, and observe the formation of *surface gap solitons*, or nonlinear Tamm states. Linear surface modes do not exist in this type of system, due to the lack of a large refractive index step at the interface between the substrate and the periodic structure [117]. However, discrete self-trapping is observed in the nonlinear regime above a certain threshold power when the propagation constant of the surface waveguide is shifted into the gap of the photonic transmission spectrum.

3.6.1 Linear diffraction and nonlinear surface self-trapping

Single-site excitation of strongly localised gap solitons, which was demonstrated in Section 3.5 above, can also be used in the study of nonlinear surface waves, as

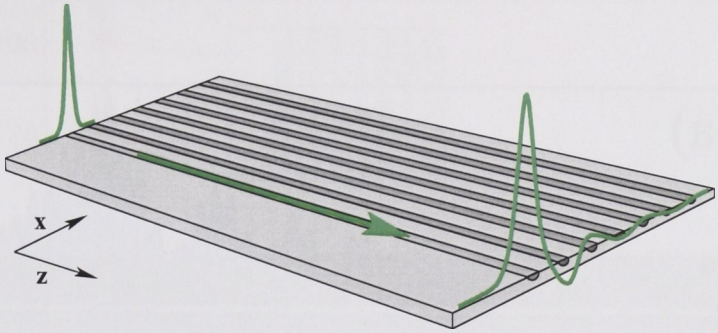

Figure 3.8: Schematic of the single-site excitation of strongly localised surface gap solitons in a waveguide array with self-defocusing nonlinearity.

illustrated in Fig. 3.8. To allow for a detailed characterisation of the self-trapping at the lattice interface we employ a waveguide array with smaller period ($d = 9\ \mu$m) and hence stronger linear coupling than in the above experiment. Similar to the case of extended waveguide arrays, we inject light into a single waveguide at the input, only this time at the very edge of the array, and vary the beam power to observe the nonlinear effects.

At low laser power ($0.1\,\mu$W) we observe that due to coupling between neighboring waveguides the probe beam experiences modified discrete diffraction and spreads out in the horizontal plane upon propagation [Figs. 3.9(a,b)]. In addition, the beam shifts dramatically to the right indicating a strong repulsive effect of the surface. Figure 3.9(a) shows the experimental image of the output intensity distribution and the corresponding transverse intensity profile. After linear propagation through the array the beam profile acquires a complex form, where the major lobe is centered approximately 42 lattice sites away from the input excitation point ($n = 0$ at the edge of the array) due to the surface repulsion and discrete diffraction. Figure 3.9(b) shows the corresponding beam propagation inside the sample, calculated by use of an analytical formula derived from the discrete model $a_n(zC) = A_0 i^n \left[J_n(2zC) + J_{n+2}(2zC)\right]$, where $a_n(zC)$ is the discrete mode amplitude in the $n-$th waveguide, A_0 is the initial field amplitude in the input waveguide $n = 0$, z is the propagation distance, and C is the intersite coupling coefficient [111]. In Fig. 3.9(b) the discrete mode amplitudes have been convoluted by the continuous waveguide mode intensity profile, and the agreement with the experimental observation is found to be excellent. The coupling coefficient is estimated to be $C = 0.46\,\mathrm{mm}^{-1}$. The inset in Fig. 3.9(b) schematically shows the geometry of the waveguide array.

Increasing the laser power leads to strong self-trapping in the surface waveguide in the form of a surface gap soliton. The slow response of the nonlinearity allows us to monitor the transient temporal dynamics of self-trapping and soliton formation, providing additional information about the localisation process. Figures 3.9(c-e) show the output beam intensity profile at times 920, 1050, and 1550 s, respectively,

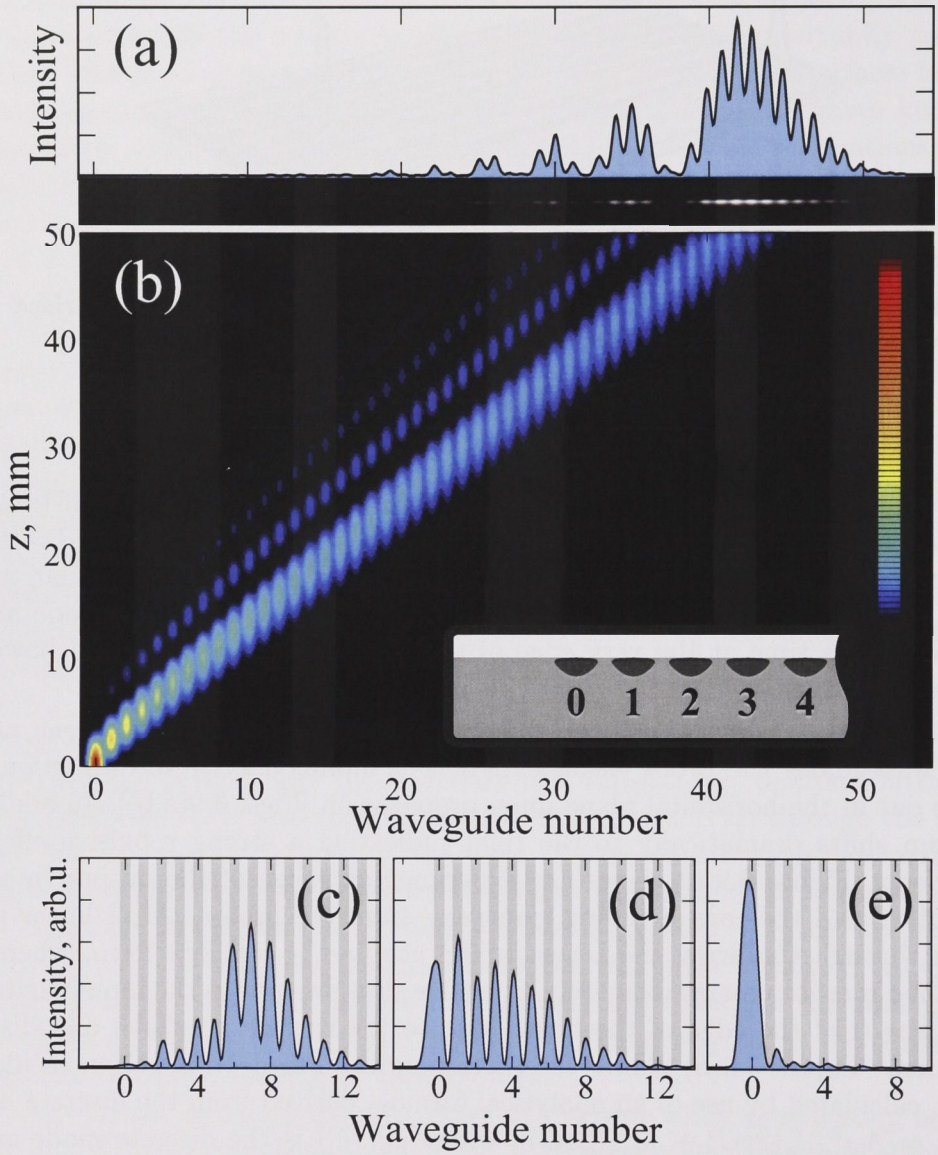

Figure 3.9: (a,b) Linear propagation of a narrow low-power beam when only the edge waveguide of the array is excited. (a) Measured transverse output intensity profile ($P = 0.1\,\mu$W) and (b) corresponding theoretically calculated longitudinal propagation inside the sample. Inset in (b) illustrates the waveguide geometry. (c-e) Formation of surface gap soliton at the array output 920, 1050, and 1550 seconds, respectively, after the input beam power is increased to $P = 0.5$ mW. Grey shading marks the waveguide positions.

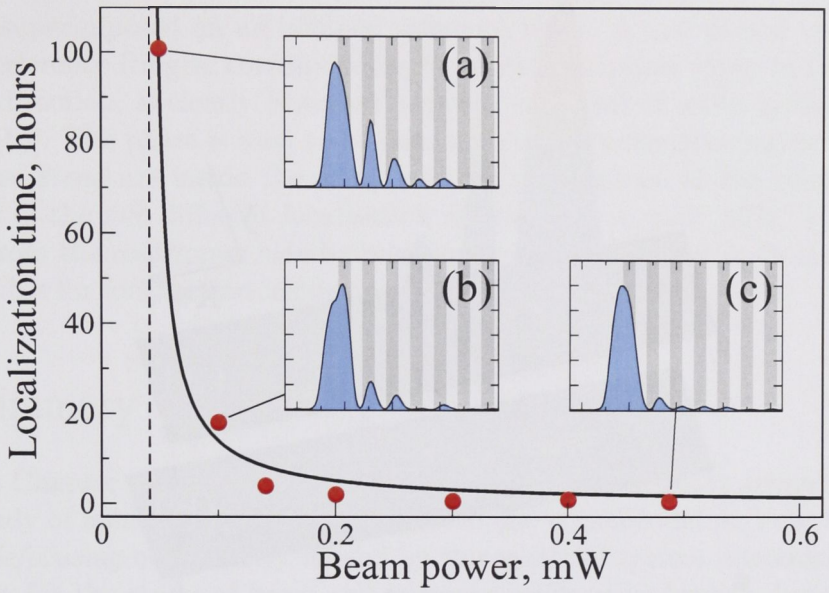

Figure 3.10: Measured surface localisation time vs. probe beam power. Solid curve: $A+B/(P-P_{\rm th})$ fit to experimental data (red dots). Vertical dashed line marks the threshold power ($P_{\rm th} = 0.042\,{\rm mW}$). (a-c) Beam intensity profiles of decreasing width corresponding to the indicated points.

after the beam power is increased to $P = 0.5$ mW. The beam is seen first to contract and shift towards the edge of the array, indicating a nonlinearity-induced suppression of the surface repulsion [Fig. 3.9(c)]. Then partial self-trapping at the surface occurs, with a tail of intensity lobes extending into the periodic structure [Fig. 3.9(d)]. A series of zero intensity points between these lobes indicates the self-induced dynamic formation of *a staggered phase structure* which is clearly absent in Fig. 3.9(a). Eventually, a strongly localised *surface gap soliton* is formed [Fig. 3.9(e)]. The asymmetry of the photonic structure is reflected in the shape of the trapped beam which decays monotonically into the continuum while showing damped oscillations inside the array, resembling the structure of the staggered Bloch wave associated with the band edge at the top of the gap [cf. Fig 1.11 and the findings in Section 3.3 above]. The defocusing nonlinearity effectively decreases the contrast of the surface waveguide, causing the localised beam to broaden and penetrate substantially into the continuous medium.

3.6.2 Localisation dynamics and nonlinear threshold

In order to study in detail the transition from linear diffraction to nonlinear self-trapping, we measure the surface gap soliton formation time as a function of the probe beam power. The results are summarised in Fig. 3.10. The formation time increases dramatically for decreasing input power until, below a certain critical power, no localised surface mode is observed. This observed critical slowing down

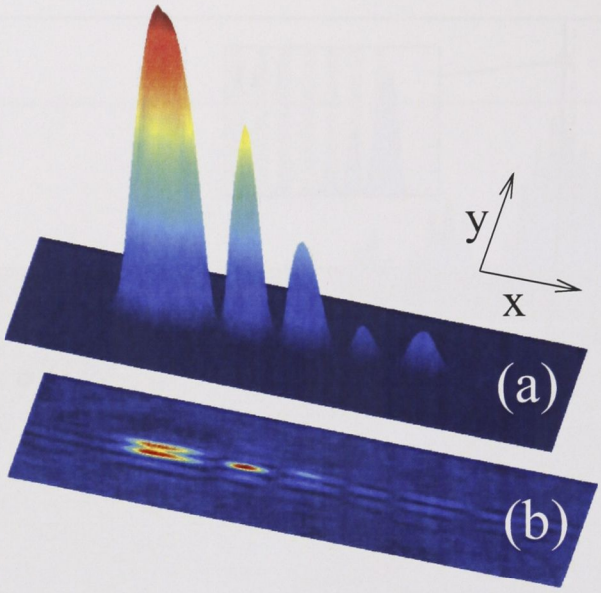

Figure 3.11: (a) Three-dimensional representation of the surface gap soliton observed near the threshold [Fig. 3.10(a)]. (b) Corresponding interferogram demonstrating the staggered phase structure of the surface gap soliton.

indicates the existence of a threshold power below which the nonlinear response is too weak to cause self-trapping. While the analytical form of the dynamics of the soliton formation near the threshold is not known, the value of the threshold power was estimated as $P_{\mathrm{th}} = 42\,\mu$W by modeling the measured dependence of the soliton formation time (Fig. 3.10, red dots) on the beam power with a simple singular relation $A + B/(P - P_{\mathrm{th}})$ (Fig. 3.10, solid curve). A and B are fitting parameters, and P_{th} is the threshold power.

Figures 3.10(a-c) show the beam intensity profiles corresponding to the indicated data points. The width of the localised mode decreases for increasing beam power, spanning about three lattice sites immediately above threshold [Fig. 3.10(a)], and approximately a single lattice site at higher power [Fig. 3.10(c)]. The decrease of the beam width is due to the fact that stronger beam self-action at higher power leads to a deeper surface defect, and hence more pronounced beam localisation.

3.6.3 Phase structure

As in the case of gap solitons in extended periodic structures, an essential feature of the observed surface gap solitons is the staggered phase structure of the beam tail inside the periodic medium. Figure 3.11(a) depicts a three-dimensional representation of the spatial beam intensity distribution of the broad surface gap soliton observed near the threshold [Fig. 3.10(a)]. Figure 3.11(b) shows the corresponding two-dimensional intensity plot of the associated interference pattern when the

output is superimposed on an inclined reference wave. A half period vertical shift of the interference fringes, corresponding to an exact π phase jump in the horizontal beam direction, is clearly observed between each pair of lobes in the structure [Fig. 3.11(b)]. The phase is seen to be constant in the continuous region. The staggered phase structure inside the array and the plane phase in the continuum are signatures of the two different localisation mechanisms in play [123]. The beam is confined from the continuum side by total internal reflection, while Bragg reflection is responsible for localisation inside the periodic structure.

3.7 Summary

In this Chapter we have explored fabricated planar waveguide arrays in $LiNbO_3$ for the study of nonlinear beam propagation in one-dimensional periodic structures. The *self-defocusing* nonlinearity offered by this material system introduces new opportunities for the study of beam self-trapping inside the photonic bandgaps, and such effects are pursued throughout the Chapter.

We have studied in detail the *crossover* between beam self-defocusing and discrete self-trapping in waveguide arrays with self-defocusing nonlinearity. We have shown that an abrupt transition is observed in the beam dynamics for increasing refractive index of the lattice. For a small refractive index modulation, narrow probe beams experience increased spatial spreading at higher input powers. However, when the lattice contrast exceeds a critical value, beam self-trapping associated with the formation of staggered gap solitons becomes possible. The crossover represents a qualitative transition from a weakly modulated system behaving much like a continuous optical medium, to a system characterised by a high degree of discreteness. We have demonstrated experimentally the generation, by single waveguide excitation, of strongly localised gap solitons supported by the self-defocusing nonlinearity. The refractive index modulation of the waveguide arrays was engineered to exceed the threshold for the nonlinear crossover.

Fabricated waveguide structures introduce the additional opportunity of studying boundary effects, including the excitation of nonlinear surface waves in semi-infinite photonic lattices, an area of research which has received considerable attention recently [78, 111, 112, 123–125]. The second study described in this Chapter demonstrated experimentally that gap solitons can exist near the surface of a periodic medium with self-defocusing nonlinearity in the form of surface gap solitons, providing the first experimental evidence of a nonlinear analog of surface Tamm states in optics. The nonlinear surface waves were observed using the single site excitation method developed in the previous work.

The increased coupling in the waveguide array employed in the study of nonlinear surface waves allowed for a detailed characterisation of the dynamics of the nonlinear localisation process. The results revealed a critical slowing down of the nonlinear response time for decreasing beam power, which was used to identify a power threshold for the formation of surface gap solitons. In addition, it was observed that the width of the self-trapped surface waves increases near the threshold

due to less pronounced beam localisation at weaker lattice defects.

In both investigated cases of discrete self-trapping, the characteristic staggered phase structure of waves localised at negative type lattice defects, i.e. in the Bragg reflection bandgap, was verified experimentally by precise interferometric measurements.

The single site excitation method demonstrated in this Chapter represents a novel approach to studying nonlinear gap localisation in discrete systems, and provides a simplified and hence powerful experimental scheme compared to the two-beam excitation technique employed in Chapter 2, and the preparation of staggered input beams in previous studies of self-trapping in defocusing waveguide arrays [114]. In addition, the use of compact fabricated waveguide structures, in combination with material systems exhibiting strong nonlinearity at moderate laser powers, further simplifies experimental efforts and reduces the footprint of the optical setup, thus increasing the potential for applications of the observed effects in microphotonic devices.

Other groups have independently reported the observation of discrete self-trapping for self-defocusing nonlinearity in the form of strongly localised surface gap solitons [124, 125], reflecting the surge of interest in nonlinear surface effects in periodic systems. Both studies adapted the single-site excitation method developed in our work [77], and thus bear witness of its universal applicability.

CHAPTER 4

Two-dimensional periodic structures

4.1 Introduction

Thus far this thesis has focused on light propagation in nonlinear media exhibiting a periodic refractive index modulation in one transverse dimension only. Such one-dimensional structures represent the simplest possible generic examples of nonlinear periodic systems, and yet a host of novel fundamental effects can be observed in one-dimensional slab and planar waveguide arrays, as discussed in the previous Chapters. One-dimensional periodic nonlinear structures are thus a natural and attractive basis for studies of the interplay between nonlinearity and periodicity in optics. Furthermore, mature lithographic microfabrication technologies enable the realisation of high quality planar waveguide structures in a number of different material systems, which makes light control in one-dimensional nonlinear periodic structures interesting for potential applications in integrated optical circuits.

In general, beam propagation in a three-dimensional space comprises dynamics in two transverse dimensions (x and y) and one longitudinal propagation dimension (z). In the case of one-dimensional periodic structures one transverse dimension (y) is ignored because there is no evolution of the field in this direction, due to either the infinite extension of beams along y (Chapter 2), or the vertical waveguiding confinement (Chapter 3), in the cases of slab and planar geometries, respectively. On the other hand, as mentioned in Section 1.7, it is possible to design *two-dimensional structures* with periodic refractive index modulations in both transverse dimensions [see Fig. 1.6(b)], and this opens up a range of novel opportunities for spatial control of light.

Many of the fundamental concepts discussed in the previous Chapters can be extended from the one-dimensional case to the two-dimensional case, including e.g. discrete diffraction and self-trapping in nonlinear lattices. In addition to these effects, two-dimensional structures can support *novel phenomena* such as discrete vortex solitons [83, 126, 127], which have no analog in the one-dimensional case. The new possibilities offered by two-dimensional periodic systems broaden the perspectives for the study of discrete and nonlinear behavior of light, which is of both fundamental and practical interest.

Whereas fundamental design options are inherently limited in one-dimensional systems, two-dimensional structures offer a number of different transverse lattice

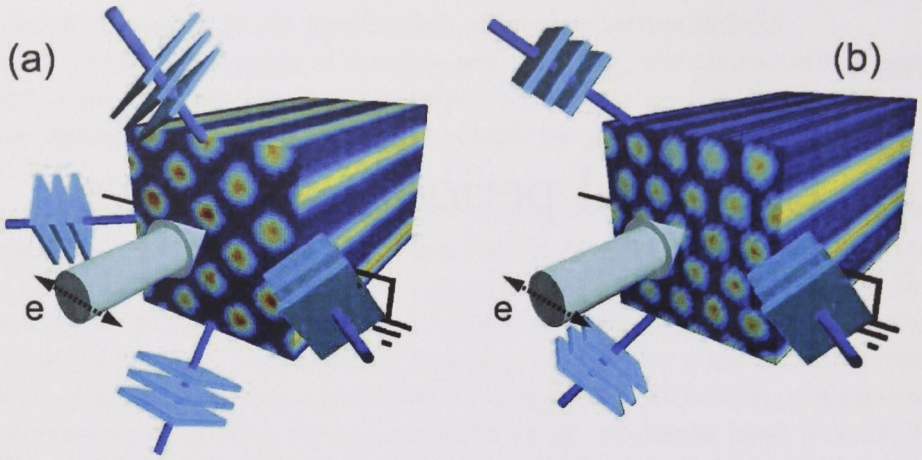

Figure 4.1: Schematic of the optical induction of (a) square and (c) triangular two-dimensional photonic lattices by plane wave interference in a biased photorefractive crystal (SBN). Lattice beams are ordinarily polarised while probe beams are extraordinarily polarised and propagate along the longitudinal lattice direction as indicated by the arrows.

geometries, including the highly symmetric square and triangular (or hexagonal) lattices [47, 63, 64, 70, 72, 82, 128–134] [see Figs. 4.1], rectangular [60] and honeycomb [135, 136] lattices, radially symmetric lattices [137–140], as well as more complex configurations such as quasiperiodic [141] and disordered lattices [73, 142]. The various two-dimensional lattice geometries exhibit different symmetries, each displaying unique properties with respect to linear and nonlinear beam propagation. For example, it was recently observed that reduced-symmetry solitons, trapped by the combined effects of total internal reflection and Bragg reflection in square photonic lattices, can possess highly anisotropic mobility properties due to the different localisation mechanisms in play along the two orthogonal symmetry axes of the lattice [129]. In addition, linear and nonlinear beam propagation in two-dimensional photonic lattices offer strong links to the fields of photonic crystals and photonic crystal fibers [50–53].

The majority of previous experimental work on nonlinear beam propagation in two-dimensional structures has focused on the square geometry [47, 63, 64, 72, 82, 129–132] [see Fig. 4.1(a)]. Self-trapping in the form of discrete and gap solitons was recently demonstrated experimentally in square photonic lattices [63, 64, 72, 129] [see also Section 1.9], whereas such effects remain largely unexploited in triangular lattices. However, self-trapping in triangular lattices was predicted and studied theoretically [60, 135]. Furthermore, periodic structures with triangular geometry are the subject of intense studies in the field of photonic crystals. This is partly due to the fact that triangular lattices are known to support larger bandgaps, and therefore most of the currently fabricated planar structures possess this symmetry. Also, the triangular geometry appears naturally in the stacking method fabrication

of photonic crystal fibers [51, 52].

The observation of discrete diffraction and nonlinear self-trapping represents a benchmark experiment in discrete nonlinear optics. In Section 4.2 of this Chapter we present the first experimental demonstration of nonlinear self-trapping of light in triangular photonic lattices [79]. The lattices are optically induced in a biased photorefractive crystal by three wave interference in a way similar to the structures studied in Chapter 2. Apart from their value as a demonstration of fundamental nonlinear effects, the results of this study represent a precursor for the observation of similar effects in fabricated periodic structures with triangular lattice geometry, in e.g. microstructured optical fibers [134].

As mentioned above, the multitude and diversity of two-dimensional lattice geometries and their unique symmetry properties greatly add to the wealth of both linear and nonlinear effects associated with light propagation in periodic structures. However, the increased complexity in two dimensions also introduces additional challenges, in particular for the experimental study of two-dimensional periodic structures. Whereas the realisation of two-dimensional optically induced lattices is a relatively straightforward extension of the one-dimensional case, the inclusion of an additional transverse dimension represents a nontrivial issue in the context of fabricated structures. To fully explore the rich physics and technological potential of two-dimensional periodic and nonlinear optical media, it is desirable to identify accessible experimental platforms that combine the advantages of high quality fabricated structures with the attractiveness of tunability and strong nonlinearity.

In Section 4.3 and the remainder of the Chapter we suggest and demonstrate a novel platform for the study of tunable nonlinear light propagation in two-dimensional discrete systems, based on photonic crystal fibers filled with high index nonlinear liquids. Using the infiltrated cladding region of a photonic crystal fiber as a nonlinear waveguide array, we experimentally demonstrate highly tunable beam diffraction and thermal self-defocusing, and realise a compact all-optical power limiter based on a tunable nonlinear response.

4.2 Self-trapping in triangular optically induced lattices

In the experiment described in this Section we study linear and nonlinear beam propagation in optically induced triangular photonic lattices. We selectively excite beams associated with Bloch waves at the upper edges of the first and second linear transmission bands of the triangular lattice structure, and employ the photorefractive self-focusing nonlinearity to observe self-trapping inside the total internal reflection gap and the Bragg reflection gap, respectively.

4.2.1 Experimental setup

Figure 4.1(b) illustrates how a triangular photonic lattice can be created by the interference of three plane waves inside a biased photorefractive crystal, in a similar way to the case of the one-dimensional optically induced lattices studied in

Chapter 2. In the study of triangular lattices we thus employ an experimental setup which strongly resembles the one described in Section 2.3 and shown in Fig. 2.2 on page 38.

We obtain three ordinarily polarised lattice writing beams by using the extended interferometer design illustrated in Fig. 2.18 on page 62. As previously, a set of extraordinarily polarised probe beams can be shaped to selectively match specific Bloch wave profiles (instead of the cylindrical lenses used to generate stripe beams in the case of one-dimensional lattices, we now focus the probe beams onto the front face of the crystal by use of spherical lenses).

The electro-optic anisotropy of the photorefractive crystal can lead to increased connectivity of lattice sites along the direction perpendicular to the c-axis of the crystal, resulting in a nonuniform contrast of the two-dimensional induced photonic lattice along its different symmetry directions [143]. To minimise such unwanted effects the triangular lattice in our experiment is oriented such that the separation of neighboring lattice sites along lines in the vertical direction is maximised, as shown in Fig. 4.2(c). Lattices rotated by 30 degrees compared to this configuration, on the other hand, can experience strong distortion of their structural symmetry.

4.2.2 Band structure and Bloch waves

The propagation of a beam along a triangular optically induced lattice is governed by the full nonlinear Schrödinger equation taking into account beam dynamics in both transverse propagation directions [see Section 1.2.6],

$$i\frac{\partial\psi}{\partial z} + D\left(\frac{\partial^2\psi}{\partial x^2} + \frac{\partial^2\psi}{\partial y^2}\right) + \mathcal{F}(x, y, |\psi|^2)\psi = 0, \tag{4.1}$$

where x and y are the transverse coordinates and z the longitudinal propagation coordinate normalised to the characteristic values $x_0 = y_0 = 1, \mu$m and $z_0 = 1$,mm, respectively, and as previously $D = z_0\lambda/(4\pi n_0 x_0^2)$ is the diffraction coefficient, λ is the wavelength in vacuum, and n_0 is the average refractive index of the medium. For a triangular lattice, the total refractive index modulation induced by the lattice beams and the nonlinear self-action of the probe beam is characterised by the function

$$\mathcal{F}(x, y, |\psi|^2) = -\frac{\gamma}{I_b + I_p(x, y) + |\psi|^2}, \tag{4.2}$$

where $I_b = 1$ is the normalised constant dark irradiance, and $I_p(x, y)$ is the three-wave interference pattern [see Fig. 4.2(c)] given by

$$I_p(x, y) = I_g|\exp(ikx) + \exp(-ikx/2 - iky\sqrt{3}/2) + \exp(-ikx/2 + iky\sqrt{3}/2)|^2, \tag{4.3}$$

where I_g is the lattice intensity, and $\gamma > 0$ is a nonlinear coefficient proportional to the applied DC field. The resulting lattice period is $d = 4\pi/(3k)$. The parameters are chosen to match the experimental conditions: $n_0 = 2.4$ is the refractive index of the bulk photorefractive crystal, $\lambda = 532$ nm is the laser wavelength in vacuum, the lattice period is $d = 23\mu m$ or $d = 30\mu m$, $\gamma = 2.36$, and $I_g = 0.49$. The applied electric field is 5 kV/cm.

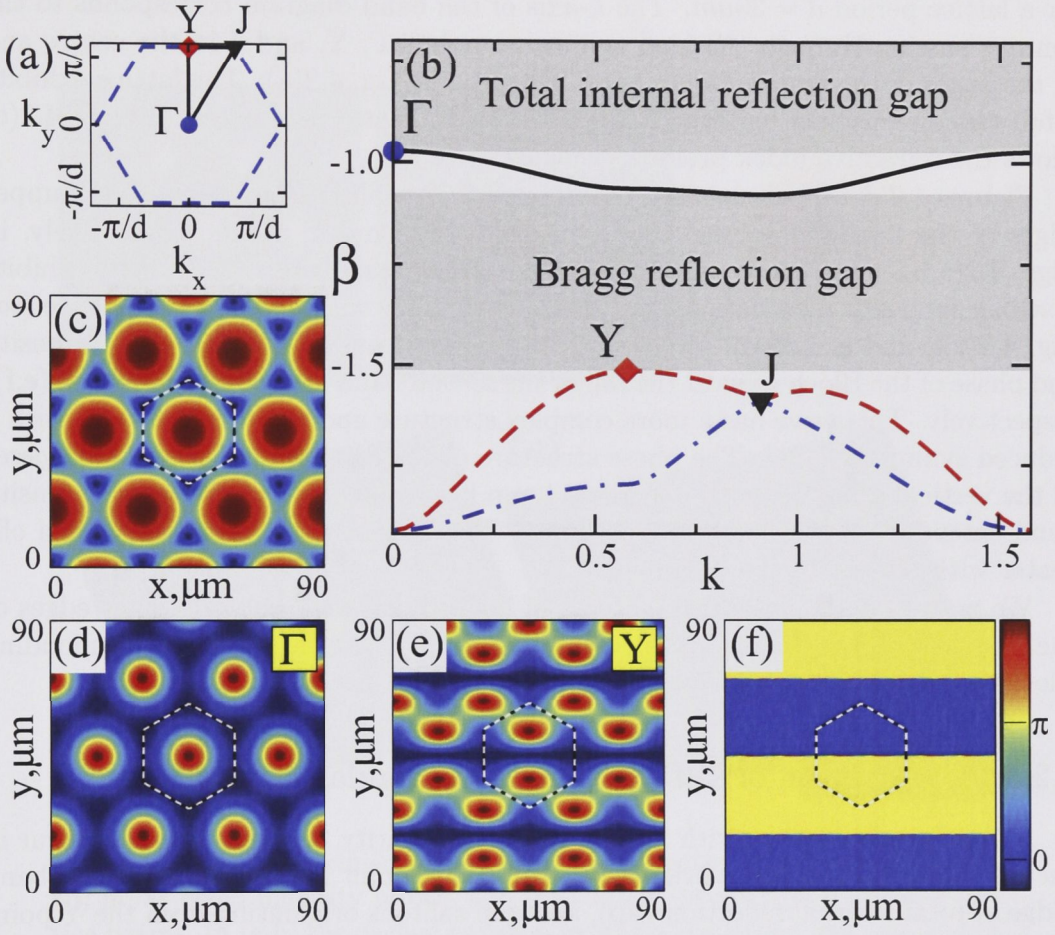

Figure 4.2: (a) Lattice unit cell in Fourier space; (b) Bloch wave dispersion along the contour passing through the high symmetry points marked in (a); (c) Refractive index profile of the triangular lattice; (d-f) Bloch waves corresponding to the Γ and Y points in (a,b): (d) intensity at the Γ point of the first band, and (e,f) intensity and phase at the Y point of the second band.

The two-dimensional Bloch waves associated with the triangular lattice geometry are found as solutions of the linearised equation (4.1) in the form $\psi(x, y, z) = u(x, y) \exp(i\kappa_x x + i\kappa_y y + i\beta z)$ where each Bloch wave profile $u(x, y)$ possesses the same periodicity as the underlying lattice. The corresponding linear diffraction relations $\beta(\kappa_x, \kappa_y)$ are periodic and fully defined by their values in the first Brillouin zone, shown in Fig. 4.2(a). The calculated bandgap spectrum is shown in Fig. 4.2(b) for a lattice period $d = 30\mu m$. The k-axis of the band diagram corresponds to the contour passing through the high symmetry points Γ, Y, and J in the centre and at the edges of the first Brillouin zone, as traced in Fig. 4.2(a). The lattice exhibits a full two-dimensional bandgap for typical experimental parameters. Figure 4.2(c) shows the refractive index profile of the lattice.

Figures 4.2(d,e) show examples of Bloch wave profiles associated with the upper edges of the first and second bands, i.e. at the Γ and Y points, respectively, in Figs. 4.2(a,b). The Bloch wave at the top of the first band [Fig. 4.2(d)] exhibits a strong intensity modulation with peaks coinciding with those of the lattice [see Fig. 4.2(c)], and a uniform phase structure in the transverse plane. The intensity and phase of the Bloch wave at the top of the second band are shown in Figs. 4.2(e,f), respectively. This wave has a more complex structure and represents a state with a reduced symmetry [129]. The phase structure of the second band wave is *staggered* in the vertical direction with a π phase jump between each zigzag-shaped intensity band extending in the horizontal direction. The intensity peaks are positioned off-center with respect to the lattice sites.

We note that the described features of both Bloch waves at the upper edges of the first and second bands are qualitatively similar to those of the corresponding Bloch waves found in one-dimensional periodic structures [cf. Fig. 1.11].

4.2.3 Observation of self-trapping in triangular lattices

In a triangular lattice with self-focusing nonlinearity, self-trapping can occur in the form of discrete solitons originating from the Γ point at the top of the first band (edge of total internal reflection gap), and gap solitons originating from the Y point at the top of the second band (edge of Bragg reflection gap) [see Fig. 4.2(b)].

In order to excite both types of self-trapped waves in the experiment, we shape the probe beams so as to approximate the symmetry of the Bloch waves associated with the corresponding points in the linear transmission spectrum. The Bloch wave at the top of the first band (Γ point) [Fig. 4.2(d)] is excited by a Gaussian beam focused onto a single lattice site at the input face of the crystal, as shown in Fig. 4.3(b). The spectral components of the input beam are centered around the Γ point in Fourier space [see Fig. 4.2(a) and Fig. 4.3(c)].

At low laser power (10 nW) the beam experiences discrete diffraction as shown in the three-dimensional plot of the output beam intensity distribution in Fig. 4.3(d). At high laser power (1 μW), on the other hand, the beam localises at the central lattice site [see Fig. 4.3(e)], resembling the discrete soliton theoretically predicted for such lattices [60, 135]. The soliton profile calculated numerically for our experimental conditions is shown in Fig. 4.3(f).

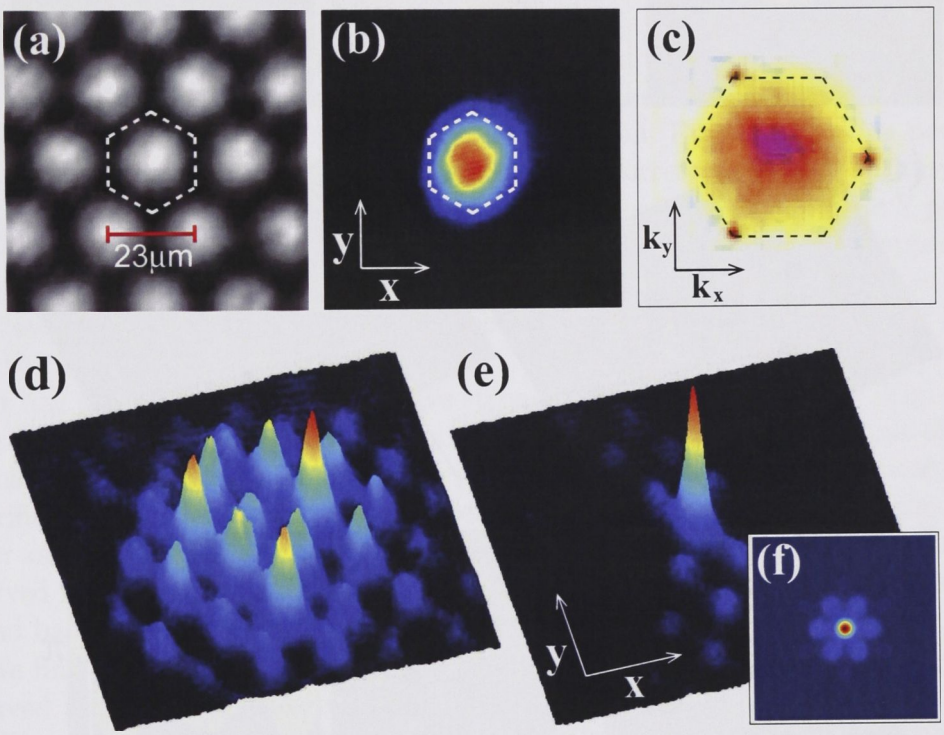

Figure 4.3: (a-c) Experimental images of (a) triangular lattice (period 23μm), (b) input beam intensity profile, and (c) Fourier spectrum of input and lattice beams. In (a,b) the dashed hexagon indicates the lattice unit cell, and in (c) the edge of the first Brillouin zone as defined by the three lattice beams. (d,e) Measured linear discrete diffraction and nonlinear self-trapping, respectively, from the top of the first band. The plot dimensions are 150μm along both x and y. (f) Numerically calculated intensity profile of a discrete soliton.

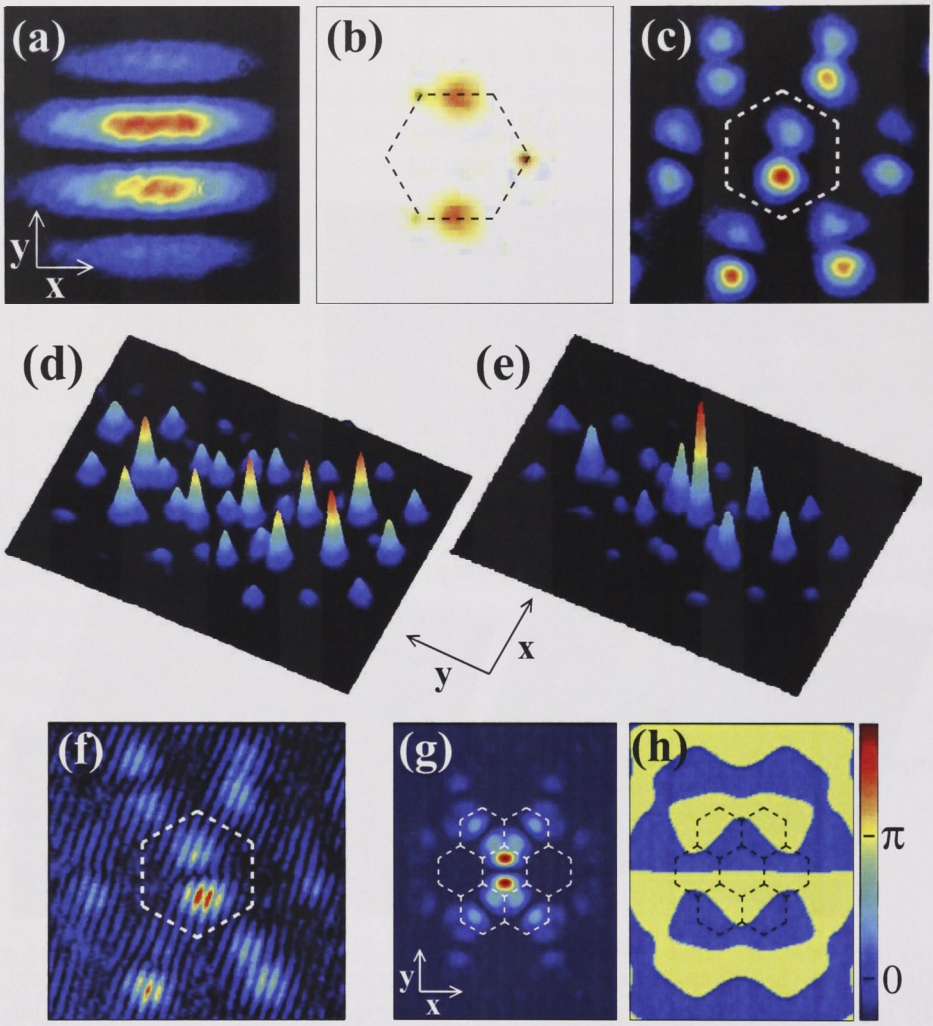

Figure 4.4: Experimental images of (a) two-beam input intensity profile, (b) Fourier spectrum of input and lattice beams, and (c) linear second band Bloch wave observed at the crystal output. In (b) the dashed hexagon indicates the edge of the first Brillouin zone, and in (c) the lattice unit cell. (d,e) Measured linear diffraction [as in (c)] and nonlinear self-trapping, respectively, from the top of the second band. The plot dimensions are $150\mu m$ along x and $200\mu m$ along y. (f) Measured interferogram for the self-trapped beam in (e). (g,h) Numerically calculated gap soliton intensity profile and phase, respectively. The lattice period is 30μm in this experiment.

We note that unlike the cases of one-dimensional and two-dimensional square lattices, where discrete diffraction leads to strong energy depletion at the central lattice site upon linear propagation, typical discrete diffraction in triangular lattices is characterised by a beam profile where a large amount of light remains in the input waveguide [133, 134] [see also Section 4.4]. The slight departure from such triangular discrete diffraction in the above experiment [Fig. 4.3(d)] may be attributed to a small lattice asymmetry caused by the anisotropy of the crystal, as discussed above, resulting in enhanced waveguide coupling and diffraction in the vertical direction (along y).

The Bloch wave associated with the Y point at the top of the second band [Figs. 4.2(e,f)] is excited experimentally by a two-beam interference pattern with a staggered phase structure along the vertical direction [Fig. 4.4(a)]. The period of the interference fringes is matched to that of the corresponding Bloch wave, and the spectral components of the two input beams are centered around the Y point in Fourier space [see Fig. 4.2(a) and Fig. 4.4(b)]. Despite the rather crude approximation to the Bloch wave profile, the second band wave is successfully excited in the experiment, as seen in Fig. 4.4(c) which shows the central part of the linear output from the lattice.

At low power the second band wave strongly diffracts in the lattice [Fig. 4.4(d)] while at high power it localises to almost a single lattice site with two out-of-phase and off-center lobes [Fig. 4.4(e)], thus preserving the Bloch wave symmetry. This is verified by interferometric measurements revealing a clear π phase jump at the center of the self-trapped beam [Fig. 4.4(f)]. Numerical calculations confirm the observed intensity [Fig. 4.4(g)] and phase [Fig. 4.4(h)] structure of the self-trapped second band beam.

We find that observations agree well with theory, although the symmetry of the observed second band wave appears to be slightly rotated at the crystal output [see Fig. 4.4(c) and Fig. 4.4(f)]. Such a rotation can be associated with mode transformation to a different family of gap solitons originating from the J point of the second spectral band [144] [Figs. 4.2(a,b)] where the phase structure at the soliton core is rotated by 30 degrees compared to the Y state. According to numerical calculations, the internal energies of the Y and J gap solitons are similar under our experimental conditions, and transformation between these states could therefore be induced by a small asymmetry of the input beam. On the other hand, we find that the nonlinear gap state [Fig. 4.4(e)] remains strongly trapped at the central lattice site subject to small variations in the tilt of the input beams.

The observed immobility demonstrates a different regime of soliton dynamics compared to the previously reported strong directional mobility of reduced-symmetry gap solitons in square lattices [129].

4.3 Photonic lattices in infiltrated microstructured fibers

Two-dimensional structures offer a range of transverse geometries with different symmetries and unique properties [63, 64, 70, 73, 79, 128–130, 133, 134] which intro-

duce new opportunities for exploiting discreteness and nonlinear effects to achieve enhanced spatial control of light. However, so far only a few physical systems have proved suitable for experimental studies of wave propagation in nonlinear media exhibiting periodicity in two transverse dimensions. These include (i) optically induced lattices [63, 64, 79, 128–130], offering tunable index contrast ($\sim 10^{-4}$) and strong photorefractive nonlinearity, but requiring a bulky setup subject to real-time conditions; (ii) fs-laser written waveguide arrays [70, 72, 133]; and (iii) multicore optical fibers [134]. The latter two types of structures offer excellent stability and structural regularity, but rely on highly specialised fabrication techniques and material systems that require large laser powers for the access to nonlinearity, and offer no dynamic tunability.

It is thus important to develop new experimental platforms that combine the advantages of high quality fabricated two-dimensional structures with the attractiveness of tunability and strong nonlinearity, in order to take full advantage of the rich physics and the technological potential of periodic and nonlinear optical media. Photonic crystal fibers [51, 52] (PCFs) are prime examples of fabricated two-dimensional microstructures which have recently become widely available. Typical PCFs are made entirely of silica and feature a periodic arrangement of air holes that extend along the length of the fiber. Filling the hollow sections of PCF structures with liquids, by use of capillary forces or pressure, allows for combining specific light guiding properties with strong material interactions for e.g. optical sensing [145–147], tunable devices [148–152], and enhancement of nonlinear effects [153–155].

In this work we suggest to use liquid-filled PCFs for the study of discrete and nonlinear light propagation in extended two-dimensional periodic systems. Conventional PCFs feature a light guiding core defect surrounded by a periodic cladding structure, and as such do not represent fully periodic systems. However, the cladding structure itself, if sufficiently large, can be regarded as an extended periodic array that displays no structural defects [156].

We experimentally demonstrate strongly tunable beam diffraction in a triangular waveguide array created by infiltrating the cladding holes of a standard PCF with a high index nonlinear liquid, and employ the thermal nonlinearity of the liquid to achieve beam self-defocusing at higher light intensity. Based on the observed effects we devise a compact all-optical power limiter device with tunable characteristics.

4.3.1 Experimental setup

The experiment is performed in a 20 mm long piece of commercially available silica PCF (Crystal Fibre LMA-15). An optical microscope image showing the cross section of the fiber is depicted in Fig. 4.5(a). The cladding region consists of 84 air holes of diameter $d = 5\mu$m arranged around the fiber core in a triangular pattern with inter-hole distance (pitch) $\Lambda = 10\mu$m. By use of capillary forces the air holes are filled with castor oil, which has a refractive index ($n = 1.48$) slightly higher than that of silica ($n = 1.46$). This results in the creation of a two-dimensional array of high index waveguides [149, 150] as shown in Fig. 4.5(b).

Light from a Verdi-V5 continuous-wave laser ($\lambda = 532$nm) is coupled into the

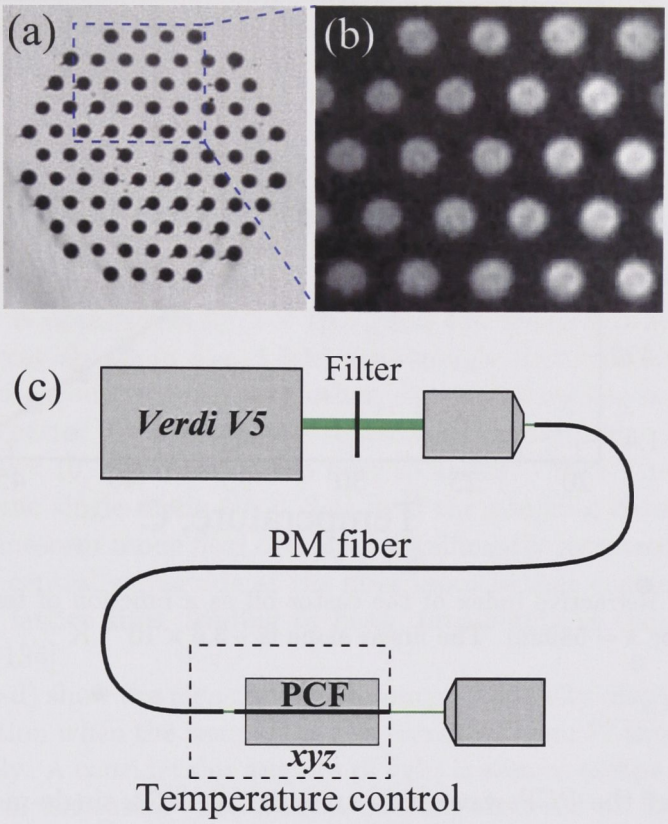

Figure 4.5: Microscope images of (a) the photonic crystal fiber, and (b) section of fiber cladding after infiltration with a high index liquid. (c) Schematic of the experimental setup for coupling of light into the infiltrated PCF. PM – polarisation maintaining fiber, xyz – three axis translation stage.

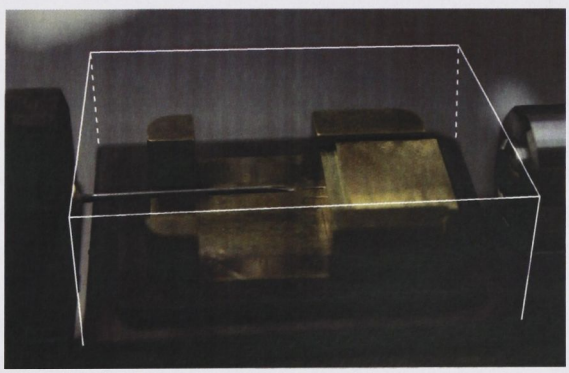

Figure 4.6: Photograph of the temperature-controlled section of the experimental setup outlined by the dashed rectangle in Fig. 4.5(c). White lines mark the position of the oven lid, removed here in order to allow for visualisation of the input fiber tube (left) and the mounted PCF sample (right).

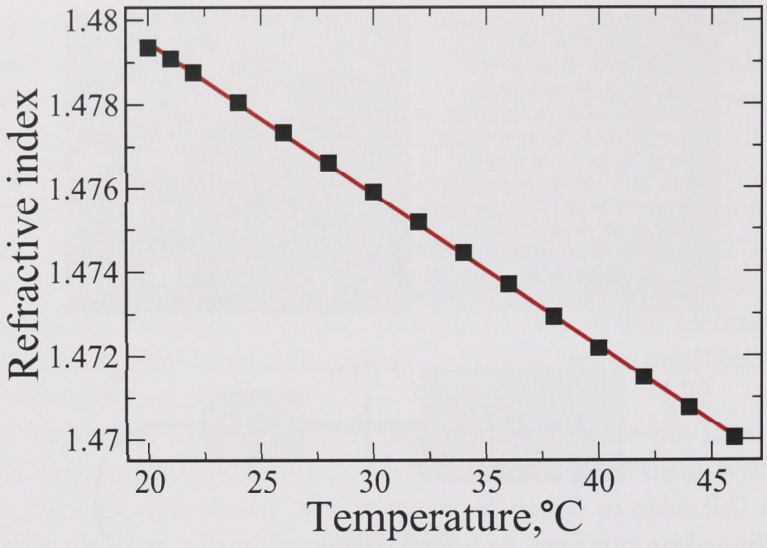

Figure 4.7: Refractive index of the castor oil as a function of temperature, measured for $\lambda = 589$nm. The linear slope is -3.6×10^{-4} K^{-1}.

central channel of the PCF waveguide array by use of a single-mode polarisation maintaining (PM) fiber [Fig. 4.5(c)]. The mode field diameter of the PM fiber (Newport F-SPA) is 3.6μm which provides a good match to the fundamental mode of the infiltrated waveguides. A drop of castor oil is applied between the input fiber and the PCF in order to further enhance the butt-coupling efficiency. After propagation through the sample, the output beam is imaged by a microscope objective. A thin glass plate is placed in contact with the end of the PCF to ensure good imaging of the near field. Neutral density filters mounted between the laser and the PM fiber allow for controlling the input beam power.

The PCF sample is placed inside a temperature controlled oven (HC Photonics TC038) which can be stabilised to ± 0.1°C over a wide temperature range, allowing for precise thermo-optic tuning of the infiltrated castor oil. The oven is mounted on a three axis translation stage to allow for precise alignment between input fiber and the PCF sample. Figure 4.6 shows a picture of the central, temperature-controlled section of the experimental setup. A thin suspended metal tube is used to position the end of the input fiber next to the PCF sample, which is fixed in a v-groove between two thermally conducting brass plates. In Fig. 4.6 the lid of the oven (outlined by white lines) has been removed in order for the details of the setup to show in the picture.

The thermo-optic response of the castor oil was characterised by measuring the refractive index as a function of temperature, using an automatic digital refractometer (Atago RX-9000-α). Figure 4.7 shows the obtained result for the wavelength $\lambda = 589$nm (D-line of sodium), and the relationship is perfectly linear in the considered temperature range, with a slope of -3.6×10^{-4} K^{-1} which defines the

thermo-optic coefficient of the oil [cf. Section 1.4]. For comparison the thermo-optic coefficient of fused silica is 1.2×10^{-5} K^{-1} [3], i.e. more than one order of magnitude smaller.

4.4 Tunable discrete diffraction

At room temperature the refractive index step between the glass and the infiltrated castor oil is approximately 2×10^{-2}, and the cladding waveguides forming the triangular array shown in Fig. 4.5(b) are strongly multi-mode (the V parameter [2] is 7.2) and decoupled from each other. By exploiting the large thermo-optic coefficient of the castor oil, it is possible to decrease the refractive index step in the lattice to below 2×10^{-3} by heating the fiber to above $\sim 70\,°C$. In this regime, the waveguides become single-mode ($V < 2.4$), and the coupling between neighboring sites through evanescent mode field overlap is significantly increased. Light which is coupled into the central waveguide at the fiber input is thus enabled to tunnel into the surrounding lattice sites, leading to beam broadening in the form of discrete diffraction [133, 134].

Figures 4.8(a-d) show the measured linear output intensity distribution for single site input excitation when the temperature is increased from 72 through 73, 74, and 75 °C, respectively. A considerable amount of light is seen to escape from the central site as the system is heated. The output pattern observed at 75 °C [Fig. 4.8(d)] features a central dominating peak while light in the neighboring waveguides form a lower intensity distribution resembling a hexagonal star. At higher temperatures the waveguide coupling is further increased, and as a result the strongly diffracting beam reaches the boundaries of the periodic structure [cf. Figs. 4.5(a) and 4.5(b)], and the triangular symmetry is broken.

Apart from such boundary effects, small irregularities of the structure (due to nonuniform hole size and separation, or variations in the composition or infiltration of the waveguide liquid) are expected to significantly compromise symmetric diffraction and lead to disorder and randomness effects [73, 134]. Indeed, even for beams confined within the periodic structure, some degree of disorder and coupling asymmetry is always observed in the experiment. Typical output profiles [Fig. 4.8(a-d)], however, resemble the discrete diffraction pattern predicted by theory and observed previously in triangular lattices [79, 133, 134].

The tunable beam diffraction demonstrated above can be used for realising dynamically controlled optical attenuation [148], as illustrated in Fig. 4.8(e) which shows the measured output transmitted through the central waveguide as a function of fiber temperature. The measurement was done by imaging the output beam onto a spatial filter blocking all but the central part of the beam.

4.5 Thermal self-defocusing

Next we investigate how the thermal defocusing nonlinearity of castor oil affects beam propagation in the two-dimensional waveguide array. Because of the large

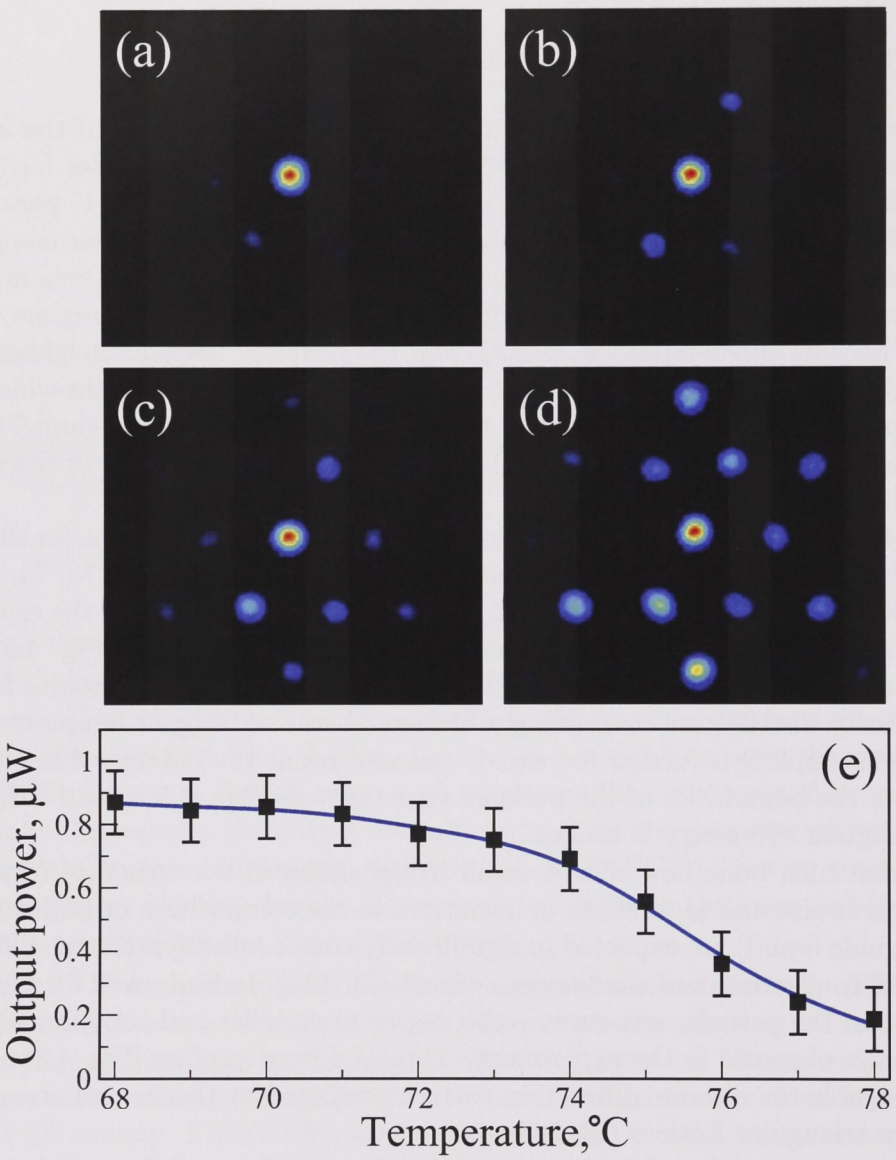

Figure 4.8: (a-d) Linear output intensity distribution for single site input excitation at temperature 72, 73, 74, and 75 °C, respectively. (e) Output power at the central lattice site measured as a function of temperature.

and negative thermo-optic coefficient inherent to most liquids, heating produced by partial absorption of the propagating beam translates into a significant decrease of the refractive index at higher light intensity [see Section 1.4]. Introducing absorbent dye into the liquid before infiltration allows for increasing this thermal nonlinear response [151]. In our experiments we use disperse red dye to control absorption losses in the infiltrated samples.

Figures 4.9(a-d) show the measured output intensity distribution for increasing laser power, when the externally controlled temperature is fixed at a level corresponding to weak linear coupling, in this case 74 °C. Figure 4.9(a) corresponds to low power linear propagation. The thermal nonlinear response causes increased diffraction or *self-defocusing* of the probe beam, eventually spreading over most of the structure as the laser power is increased [Figs. 4.9(b-d)]. As a consequence, the output power in the central waveguide decreases relative to the input power, giving rise to a nonlinear power characteristic as shown in Fig. 4.9(e). Two regimes of propagation can be identified: at low laser power the dependence is linear to a very good approximation, but above 25 mW input power the nonlinear defocusing increasingly limits the optical throughput, and the output power eventually drops after reaching a maximum at about 52 mW input power.

We finally demonstrate how this nonlinear power characteristic can be combined with the independent thermal control of the linear properties, discussed in the previous Section, to realise a tunable all-optical power limiter. Figure 4.10(a) shows the nonlinear power characteristic traced for a range of different temperatures with the top and bottom curves corresponding to 73 and 77 °C, respectively. We point out that beam self-defocusing is observed for all temperatures in the experiment, i.e. regardless of the strength of the linear coupling in the array. However, the linear slope of the characteristic curve at low input power is seen to drop for increasing temperature [Fig. 4.10(a)], in agreement with our characterisation of the linear properties [Fig. 4.8(e)]. Correspondingly, the maximum output power in the nonlinear regime also varies with temperature, and can be tuned externally as shown in Fig. 4.10(b).

We note that a photoinduced degradation of the oil leading to increased absorption and stronger nonlinearity was observed for long exposure at high laser power. This effect, however, was found to have no qualitative effect on our results. Any significant degradation was avoided in our measurements by limiting the high power exposure time.

We also note that the strong defocusing observed in the experiment [Fig. 4.9] could indicate a high degree of nonlocality [9] associated with the thermal nonlinear response. That is, heat produced in the input waveguide diffuses throughout the structure and may substantially increase the temperature and waveguide coupling in the entire array, rather than detuning only a single waveguide. This idea is supported by the fact that the defocusing behavior is observed for any input position in the array, regardless of boundary and disorder effects and the strength of the linear coupling. In disordered arrays a local nonlinear response, on the other hand, can lead to both beam localisation and spreading, depending on the input position [73].

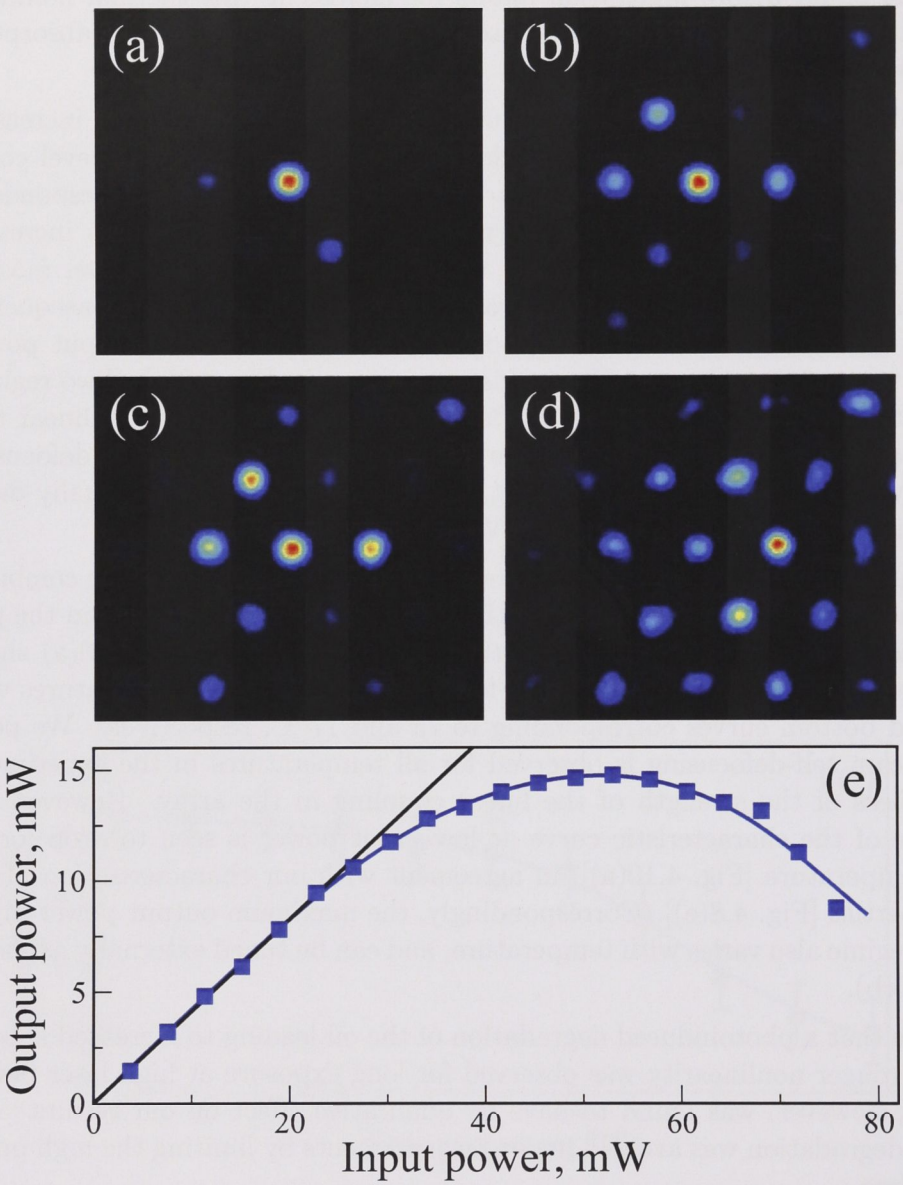

Figure 4.9: (a-d) Output intensity distribution at 74 °C for increasing laser power; (a) corresponds to linear propagation. (e) Output power measured at the central lattice site versus input beam power for weakly absorbing sample.

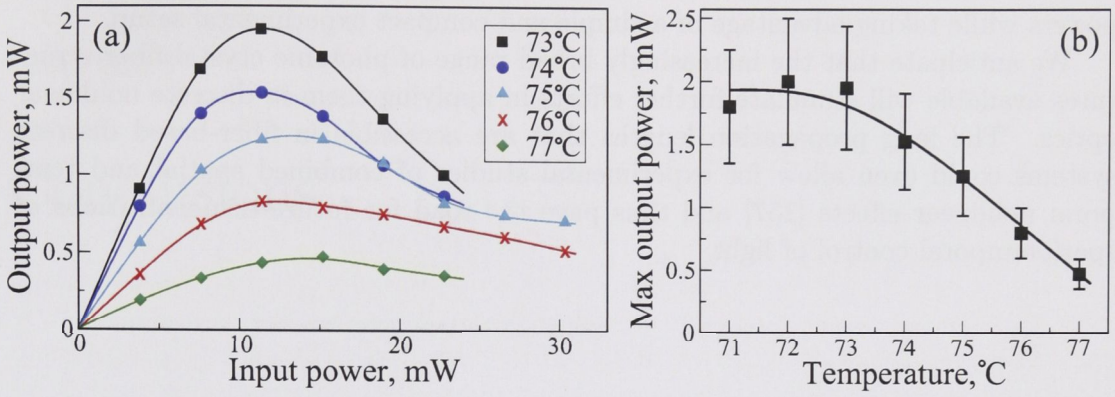

Figure 4.10: (a) Output versus input power at the central lattice site measured at different temperatures for moderately absorbing sample. (b) Corresponding maximum output power as a function of temperature.

We believe that a characterisation of the temporal dynamics of the system could shed further light on the possible effect of nonlocality, as e.g. transitory beam self-trapping at a negative type lattice defect may happen on a short time scale before thermal equilibrium is reached.

4.6 Summary

In this Chapter we have studied linear and nonlinear light propagation in two-dimensional photonic structures exhibiting triangular (or hexagonal) lattice geometry. Beam self-trapping in the form of two-dimensional discrete and gap solitons was demonstrated experimentally in *optically induced* triangular photonic lattices. The observed effects may be applied to other types of nonlinear periodic structures with similar geometry, e.g. in the field of photonic crystals and microstructured optical fibers.

As a step towards fabricated and device oriented structures, we have developed and studied a novel experimental platform for the study of discrete and nonlinear light propagation in two-dimensional periodic systems, based on liquid-filled *photonic crystal fibers*. We have experimentally demonstrated thermal control of linear discrete diffraction and nonlinear self-defocusing in a triangular fiber waveguide array and, based on these effects, realised dynamically tunable all-optical power limiting. The spatial control of light is enabled by the combined effects of discreteness, strong material tunability and nonlinearity of the infiltrated liquid, and does not rely on any architectural light guiding core defects as in the case of conventional photonic crystal fibers.

The use of commercially available fabricated microstructures in combination with liquid infiltration avoids the need for specialised high-precision fabrication procedures [134], and provides high tunability and nonlinearity at moderate laser

powers while taking advantage of a simple and compact experimental setup.

We anticipate that the increasingly broad range of photonic crystal fiber structures available will stimulate further efforts in applying them in discrete nonlinear optics. The long propagation lengths that are accessible in fiber-based discrete systems could even allow for experimental studies of combined spatial and temporal nonlinear effects [157] and thus pave the road for future demonstrations of spatiotemporal control of light.

CHAPTER 5

Conclusions

Nonlinear and periodic optical media exhibit a range of unique properties, which represent powerful tools for the fundamental study of light, and which can be exploited for controlling and manipulating the flow of light in optical systems. Developments in the field, particurlarly towards applications in photonic systems and devices, strongly rely on advances in microfabrication technology and experimental capabilities.

This thesis has explored a number of different experimental platforms for the study of nonlinear light propagation in periodic photonic structures. Two main aspects characterise the structure of the research which was undertaken: (i) the transition from one-dimensional to two-dimensional systems, which enhances the diversity of lattice geometries and phenomena that can be observed; and (ii) the transition from bulky testbed experiments based on optically induced lattices to the use of compact and highly nonlinear fabricated periodic structures, which facilitate the technological application of the fundamental effects discovered in discrete nonlinear optics.

Optically induced lattices in photorefractive strontium barium niobate (SBN) crystals were used as an established experimental platform upon which the research was built, first in the study of one-dimensional photonic lattices [74–76], and then in the demonstration of light self-trapping in two-dimensional triangular lattices [79]. The experiments involving one-dimensional optically induced lattices were focused at demonstrating novel effects reaching beyond the fundamentals of discrete nonlinear light propagation studied previously in such structures [47, 61, 62, 92]. In particular, the experiments took advantage of the inherent tunability of the system to realise electro-optically and all-optically controlled beam manipulation. Nonlinear interaction of several different Bloch waves, including the effect of discrete interband mutual focusing, was demonstrated and studied in detail [74], as well as tunable beam refraction and steering in tilted lattices [75], and optically controlled beam steering in modulated lattices [76].

The study of linear and nonlinear beam propagation in lithium niobate ($LiNbO_3$) waveguide arrays represented a transition towards the use of high quality fabricated photonic lattices, and thus the possibility of applying spatial nonlinear effects in device oriented structures. In addition, the self-defocusing nonlinearity introduced new opportunities for studying fundamental beam propagation effects, including

discrete self-trapping in photonic bandgaps in the form of gap solitons and nonlinear surface waves, and for characterising the dynamics of the nonlinear localisation process [77, 78].

Finally a novel experimental platform based on liquid-filled photonic crystal fibers was proposed and implemented experimentally, combining the advantages of tunable structures and strong nonlinearity with the use of commercially available fabricated periodic structures. This system was used to demonstrate thermo-optically tunable discrete diffraction, and thermal nonlinear self-action leading to controllable beam defocusing and all-optical power limiting [80].

The use of fiber based structures in discrete nonlinear optics opens up a promising future avenue where combined temporal and spatial nonlinear effects such as spatio-temporal solitons or light bullets could be observed. This represents one of the most exciting possible new research directions, which can further consolidate the field and establish new links to other research areas and to novel applications in the domain of fiber optics.

Bibliography

[1] C. R. Rosberg, R. Fischer, and A. Prasad, "Long-distance learning: teaching optics in the outback," Opt. Phot. News **18**(6), 22–23 (2007).

[2] B. E. A. Saleh and M. C. Teich, *Fundamentals of Photonics* (Wiley, New York, 1991).

[3] R. W. Boyd, *Nonlinear Optics*, 2nd ed. (Academic Press, New York, 2003), Chap. IV.

[4] Yu. S. Kivshar and G. P. Agrawal, *Optical Solitons: From Fibers to Photonic Crystals* (Academic Press, San Diego, 2003).

[5] G. P. Agrawal, *Nonlinear Fiber Optics*, 3rd ed. (Academic Press, New York, 2001).

[6] J. Feinberg, "Photorefractive nonlinear optics," Physics Today **41,** 46–52 (1988).

[7] M. Segev, G. C. Valley, B. Crosignani, P. D. Porto, and A. Yariv, "Steady-state spatial screening solitons in photorefractive materials with external applied field," Phys. Rev. Lett. **73,** 3211–3214 (1994).

[8] D. N. Christodoulides and M. I. Carvalho, "Bright, dark, and gray spatial soliton states in photorefractive media," J. Opt. Soc. Am. B **12,** 1628–1633 (1995).

[9] W. Królikowski, O. Bang, N. I. Nikolov, D. Neshev, J. Wyller, J. J. Rasmussen, and D. Edmundson, "Modulational instability, solitons and beam propagation in spatially nonlocal nonlinear media," J. Opt. B: Quantum Semiclass. Opt. **6,** S288–S294 (2004).

[10] D. N. Christodoulides, F. Lederer, and Y. Silberberg, "Discretizing light behaviour in linear and nonlinear waveguide lattices," Nature **424,** 817–823 (2003).

[11] N. W. Ashcroft and N. D. Mermin, *Solid State Physics* (Holt, Rinehart And Winston, New York, 1976).

[12] D. N. Christodoulides and R. I. Joseph, "Discrete self-focusing in nonlinear arrays of coupled waveguides," Opt. Lett. **13,** 794–796 (1988).

[13] Yu. S. Kivshar, "Self-localization in arrays of defocusing waveguides," Opt. Lett. **18,** 1147–1149 (1993).

[14] P. St. J. Russell, T. A. Birks, and F. D. Lloyd Lucas, "Photonic Bloch waves and photonic band gaps," in *Confined Electrons and Photons*, E. Burstein and C. Weisbuch, eds. (Plenum Press, New York, 1995), pp. 585–633.

[15] E. Fermi, J. Pasta, and S. Ulam, "Studies of nonlinear problems," (Los Alamos Scientific Laboratory, Los Alamos, N.M., 1955), Tech. Rep. LA-1940.

[16] M. Hercher, "Laser-induced damage in transparent media," J. Opt. Soc. Am. **54,** 563 (1964).

[17] R. Y. Chiao, E. Garmire, and C. H. Townes, "Self-trapping of optical beams," Phys. Rev. Lett. **13,** 479–482 (1964).

[18] V. E. Zakharov and A. B. Shabat, "Exact theory of two-dimensional self-focusing and one-dimensional self-modulation of waves in nonlinear media," Zh. Eksp. Teor. Fiz. **61,** 118–134 (1971) [Sov. Phys. JETP **34,** 62–69 (1972)].

[19] N. J. Zabusky and M. D. Kruskal, "Interaction of "solitons" in a collisionless plasma and the recurrence of initial states," Phys. Rev. Lett. **15,** 240–243 (1965).

[20] A. S. Davydov, "The theory contraction of proteins under their excitation," J. Theor. Biol. **38,** 559–569 (1973).

[21] B. Eiermann, Th. Anker, M. Albiez, M. Taglieber, P. Treutlein, K.-P. Marzlin, and M. K. Oberthaler, "Bright Bose-Einstein gap solitons of atoms with repulsive interaction," Phys. Rev. Lett. **92,** 230401–4 (2004).

[22] A. Hasegawa and F. Tappert, "Transmission of stationary nonlinear optical pulses in dispersive dielectric fibers. I. Anomalous dispersion," Appl. Phys. Lett. **23,** 142–144 (1973).

[23] L. F. Mollenauer, R. H. Stolen, and J. P. Gordon, "Experimental observation of picosecond pulse narrowing and solitons in optical fibers," Phys. Rev. Lett. **45,** 1095–1098 (1980).

[24] A. Barthélemy, S. Maneuf and C. Froehly, "Propagation soliton et auto-confinement de faisceaux laser par non linéarité optique de Kerr," Optics Comm. **55,** 201–206 (1985).

[25] S. Maneuf, R. Desailly, and C. Froehly, "Stable self-trapping of laser beams: observation in a nonlinear planar waveguide," Optics Comm. **65,** 193–198 (1988).

[26] J. S. Aitchison, A. M. Weiner, Y. Silberberg, M. K. Oliver, J. L. Jackel, D. E. Leaird, E. M. Vogel, and P. W. E. Smith, "Observation of spatial optical solitons in a nonlinear glass waveguide," Opt. Lett. **15,** 471–473 (1990).

[27] M. Segev, B. Crosignani, A. Yariv, and B. Fischer, "Spatial solitons in photorefractive media," Phys. Rev. Lett. **68,** 923–926 (1992).

[28] E. DelRe, B. Crosignani, and P. Di Porto, "Photorefractive spatial solitons," in *Spatial Solitons*, Vol. 82 of *Springer Series in Optical Sciences*, S. Trillo and W. Torruellas, eds. (Springer-Verlag, Berlin, 2001), pp. 61–85.

[29] G. C. Duree, Jr., J. L. Shultz, G. J. Salamo, M. Segev, A. Yariv, B. Crosignani, P. Di Porto, E. J. Sharp, and R. R. Neurgaonkar, "Observation of self-trapping of an optical beam due to the photorefractive effect," Phys. Rev. Lett. **71,** 533–536 (1993).

[30] M. D. Iturbe Castillo, P. A. Marquez Aguilar, J. J. Sanchez-Mondragon, S. Stepanov, and V. Vysloukh, "Spatial solitons in photorefractive $Bi_{12}TiO_{20}$ with drift mechanism of nonlinearity," Appl. Phys. Lett. **64,** 408–410 (1994).

[31] G. C. Valley, M. Segev, B. Crosignani, A. Yariv, M. M. Fejer, and M. C. Bashaw, "Dark and bright photovoltaic spatial solitons," Phys. Rev. A **50,** R4457–R4460 (1994).

[32] S. M. Jensen, "The nonlinear coherent coupler," IEEE J. Quantum Electron. **QE-18,** 1580–1583 (1982).

[33] H. S. Eisenberg, Y. Silberberg, R. Morandotti, A. R. Boyd, and J. S. Aitchison, "Discrete spatial optical solitons in waveguide arrays," Phys. Rev. Lett. **81,** 3383–3386 (1998).

[34] R. Morandotti, U. Peschel, J. S. Aitchison, H. S. Eisenberg, and Y. Silberberg, "Dynamics of discrete solitons in optical waveguide arrays," Phys. Rev. Lett. **83,** 2726–2729 (1999).

[35] H. S. Eisenberg, Y. Silberberg, R. Morandotti, and J. S. Aitchison, "Diffraction management," Phys. Rev. Lett. **85,** 1863–1866 (2000).

[36] T. Pertsch, T. Zentgraf, U. Peschel, A. Bräuer, and F. Lederer, "Anomalous refraction and diffraction in discrete optical systems," Phys. Rev. Lett. **88,** 093901–4 (2002).

[37] R. Morandotti, H. S. Eisenberg, Y. Silberberg, M. Sorel, and J. S. Aitchison, "Self-focusing and defocusing in waveguide arrays," Phys. Rev. Lett. **86,** 3296–3299 (2001).

[38] Y. S. Kivshar and D. K. Campbell, "Peierls-Nabarro potential barrier for highly localized nonlinear modes," Phys. Rev. E **48,** 3077–3081 (1993).

[39] A. B. Aceves, C. De Angelis, T. Peschel, R. Muschall, F. Lederer, S. Trillo, and S. Wabnitz, "Discrete self-trapping, soliton interactions, and beam steering in nonlinear waveguide arrays," Phys. Rev. E **53,** 1172–1189 (1996).

[40] O. Bang and P. D. Miller, "Exploiting discreteness for switching in waveguide arrays," Opt. Lett. **21,** 1105–1107 (1996).

[41] W. Krolikowski and Y. S. Kivshar, "Soliton-based optical switching in waveguide arrays," J. Opt. Soc. Am. B **13,** 876–880 (1996).

[42] T. Pertsch, U. Peschel, and F. Lederer, "All-optical switching in quadratically nonlinear waveguide arrays," Opt. Lett. **28,** 102–104 (2003).

[43] T. Pertsch, P. Dannberg, W. Elflein, A. Bräuer, and F. Lederer, "Optical Bloch oscillations in temperature tuned waveguide arrays," Phys. Rev. Lett. **83**, 4752–4755 (1999).

[44] T. Pertsch, T. Zentgraf, U. Peschel, A. Bräuer, and F. Lederer, "Beam steering in waveguide arrays," Appl. Phys. Lett. **80,** 3247–3249 (2002).

[45] D. Mandelik, H. S. Eisenberg, Y. Silberberg, R. Morandotti, and J. S. Aitchison, "Band-gap structure of waveguide arrays and excitation of Floquet-Bloch solitons," Phys. Rev. Lett. **90,** 053902–4 (2003).

[46] D. Mandelik, R. Morandotti, J. S. Aitchison, and Y. Silberberg, "Gap solitons in waveguide arrays," Phys. Rev. Lett. **92,** 093904–4 (2004).

[47] D. Neshev, A. A. Sukhorukov, B. Hanna, W. Krolikowski, and Yu. S. Kivshar, "Controlled generation and steering of spatial gap solitons," Phys. Rev. Lett. **93,** 083905–4 (2004).

[48] E. Yablonovitch, "Inhibited spontaneous emission in solid-state physics and electronics," Phys. Rev. Lett. **58,** 2059–2062 (1987).

[49] S. John, "Strong localization of photons in certain disordered dielectric superlattices," Phys. Rev. Lett. **58,** 2486–2489 (1987).

[50] J. D. Joannopoulos, R. D. Meade, and J. N. Winn, *Photonic Crystals: Molding the Flow of Light* (Princeton University Press, Princeton, 1995).

[51] P. St. J. Russell, "Photonic Crystal Fibers," Science **299,** 358-362 (2003).

[52] A. Bjarklev, J. Broeng, and A. S. Bjarklev, *Photonic Crystal Fibres* (Kluwer/Springer, Dordrecht, 2003).

[53] *Nonlinear Photonic Crystals*, Vol. 10 of *Springer Series in Photonics,* R. E. Slusher and B. J. Eggleton, eds. (Springer-Verlag, Berlin, 2003).

[54] W. Chen and D. L. Mills, "Gap solitons and the nonlinear optical response of superlattices," Phys. Rev. Lett. **58,** 160–163 (1987).

[55] D. N. Christodoulides and R. I. Joseph, "Slow Bragg solitons in nonlinear periodic structures," Phys. Rev. Lett. **62,** 1746–1749 (1989).

[56] C. M. de Sterke and J. E. Sipe, "Gap solitons," in *Progress in Optics XXXIII*, E. Wolf, ed. (Elsevier, Amsterdam, 1994), Chap. III, pp. 203–260.

[57] B. J. Eggleton, R. E. Slusher, C. M. de Sterke, P. A. Krug, and J. E. Sipe, "Bragg grating solitons," Phys. Rev. Lett. **76,** 1627–1630 (1996).

[58] B. J. Eggleton, R. E. Slusher, C. M. de Sterke, P. A. Krug, and J. E. Sipe, "Bragg solitons in the nonlinear Schrödinger limit: experiment and theory," J. Opt. Soc. Am. B **16,** 587–599 (1999).

[59] C. M. de Sterke, B. J. Eggleton, and J. E. Sipe, "Bragg solitons: theory and experiments," in *Spatial Solitons*, Vol. 82 of *Springer Series in Optical Sciences*, S. Trillo and W. Torruellas, eds. (Springer-Verlag, Berlin, 2001), pp. 169–209.

[60] N. K. Efremidis, S. Sears, D. N. Christodoulides, J. W. Fleischer, and M. Segev, "Discrete solitons in photorefractive optically induced photonic lattices," Phys. Rev. E **66,** 046602–5 (2002).

[61] J. W. Fleischer, T. Carmon, M. Segev, N. K. Efremidis, and D. N. Christodoulides, "Observation of discrete solitons in optically induced real time waveguide arrays," Phys. Rev. Lett. **90,** 023902–4 (2003).

[62] D. Neshev, E. Ostrovskaya, Y. Kivshar, and W. Krolikowski, "Spatial solitons in optically induced gratings," Opt. Lett. **28,** 710–712 (2003).

[63] H. Martin, E. D. Eugenieva, Z. G. Chen, and D. N. Christodoulides, "Discrete solitons and soliton-induced dislocations in partially coherent photonic lattices," Phys. Rev. Lett. **92,** 123902–4 (2004).

[64] J. W. Fleischer, M. Segev, N. K. Efremidis, and D. N. Christodoulides, "Observation of two-dimensional discrete solitons in optically induced nonlinear photonic lattices," Nature **422,** 147–150 (2003).

[65] A. Fratalocchi, G. Assanto, K. A. Brzdakiewicz, and M. A. Karpierz, "Discrete propagation and spatial solitons in nematic liquid crystals," Opt. Lett. **29**, 1530–1532 (2004).

[66] A. Fratalocchi, G. Assanto, K. Brzdakiewicz, and M. Karpierz, "Discrete propagation and spatial solitons in nematic liquid crystals," Opt. Express **13**, 1808–1815 (2005).

[67] T. Pertsch, U. Peschel, and F. Lederer, "Discrete bright solitary waves in quadratically nonlinear media," Phys. Rev. E **57,** 1127–1133 (1998).

[68] S. Darmanyan, A. Kobyakov, and F. Lederer, "Strongly localized modes in discrete systems with quadratic nonlinearity," Phys. Rev. E **57,** 2344–2349 (1998).

[69] R. Iwanow, R. Schiek, G. I. Stegeman, T. Pertsch, F. Lederer, Y. Min, and W. Sohler, "Observation of discrete quadratic solitons," Phys. Rev. Lett. **93,** 113902–4 (2004).

[70] T. Pertsch, U. Peschel, F. Lederer, J. Burghoff, M. Will, S. Nolte, and A. Tünnermann, "Discrete diffraction in two-dimensional arrays of coupled waveguides in silica," Opt. Lett. **29,** 468–470 (2004).

[71] A. Szameit, D. Blömer, J. Burghoff, T. Schreiber, T. Pertsch, S. Nolte, A. Tünnermann, and F. Lederer, "Discrete nonlinear localization in femtosecond laser written waveguides in fused silica," Opt. Express **13,** 10552–10557 (2005).

[72] A. Szameit, J. Burghoff, T. Pertsch, S. Nolte, A. Tünnermann, and F. Lederer, "Two-dimensional soliton in cubic fs laser written waveguide arrays in fused silica," Opt. Express **14,** 6055–6062 (2006).

[73] T. Pertsch, U. Peschel, J. Kobelke, K. Schuster, H. Bartelt, S. Nolte, A. Tünnermann, and F. Lederer, "Nonlinearity and disorder in fiber arrays," Phys. Rev Lett. **93,** 053901–4 (2004).

[74] C. R. Rosberg, B. Hanna, D. N. Neshev, A. A. Sukhorukov, W. Krolikowski, and Yu. S. Kivshar, "Discrete interband mutual focusing in nonlinear photonic lattices," Opt. Express **13**, 5369–5376 (2005).

[75] C. R. Rosberg, D. N. Neshev, A. A. Sukhorukov, Y. S. Kivshar, and W. Krolikowski, "Tunable positive and negative refraction in optically induced photonic lattices," Opt. Lett. **30,** 2293–2295 (2005).

[76] C. R. Rosberg, I. L. Garanovich, A. A. Sukhorukov, D. N. Neshev, W. Krolikowski, and Yu. S. Kivshar, "Demonstration of all-optical beam steering in modulated photonic lattices," Opt. Lett. **31**, 1498–1500 (2006).

[77] M. Matuszewski, C. R. Rosberg, D. N. Neshev, A. A. Sukhorukov, A. Mitchell, M. Trippenbach, M. W. Austin, W. Krolikowski, and Yu. S. Kivshar, "Crossover from self-defocusing to discrete trapping in nonlinear waveguide arrays," Opt. Express **14**, 254–259 (2006).

[78] C. R. Rosberg, D. N. Neshev, W. Krolikowski, A. Mitchell, R. A. Vicencio, M. I. Molina, and Yu. S. Kivshar, "Observation of surface gap solitons in semi-infinite waveguide arrays," Phys. Rev. Lett. **97**, 083901–4 (2006).

[79] C. R. Rosberg, D. N. Neshev, A. A. Sukhorukov, W. Krolikowski, and Y. S. Kivshar, "Observation of nonlinear self-trapping in triangular photonic lattices," Opt. Lett. **32,** 397–399 (2007).

[80] C. R. Rosberg, F. H. Bennet, D. N. Neshev, P. D. Rasmussen, O. Bang, W. Krolikowski, A. Bjarklev, and Yu. S. Kivshar, "Tunable diffraction and self-defocusing in liquid-filled photonic crystal fibers," Opt. Express **15**, 12145–12150 (2007).

[81] Z. Chen and K. McCarthy, "Spatial soliton pixels from partially incoherent light," Opt. Lett. **27,** 2019–2021 (2002).

[82] Z. G. Chen, H. Martin, E. D. Eugenieva, J. Xu, and A. Bezryadina, "Anisoptrophic enhancement of discrete diffraction and discrete soliton trains in partially coherent photonic lattices," Phys. Rev. Lett. **92**, 143902–4 (2004).

[83] D. N. Neshev, T. J. Alexander, E. A. Ostrovskaya, Y. S. Kivshar, H. Martin, I. Makasyuk, and Z. Chen, "Observation of discrete vortex solitons in optically-induced photonic lattices," Phys. Rev. Lett. **92**, 123903–4 (2004).

[84] X. S. Wang. J. Young, and Z. G. Chen, "Observation of lower to higher bandgap transition of one-dimensional defect modes," Opt. Express **14**, 7362–7367 (2006).

[85] I. Makasyuk, Z. Chen, and J. Yang, "Bandgap guidance in optically-induced photonic lattices with a negative defect," Phys. Rev. Lett. **96,** 223903–4 (2006).

[86] D. Neshev, Y. S. Kivshar, H. Martin, and Z. Chen, "Soliton stripes in two-dimensional nonlinear photonic lattices," Opt. Lett. **29,** 486–488, (2004).

[87] A. Bezryadina, D. Neshev, A. Desyatnikov, J. Young, Z. Chen, and Y. S. Kivshar, "Observation of topological transformations of optical vortices in two-dimensional photonic lattices," Opt. Express **14,** 8317–8327 (2006).

[88] U. B. Dörfler, R. Piechatzek, T. Woike, M. K. Imlau, V. Wirth, L. Bohatý, T. Volk, R. Pankrath, and M. Wöhlecke, "A holographic method for the determination of all linear electrooptic coefficients applied to Ce-doped strontium-barium-niobate," Appl. Phys. B **68**, 843–848 (1999).

[89] K. Onuki, N. Uchida, and T. Saku, "Interferometric method for measuring electro-optic coefficients in crystals," J. Opt. Soc. Am. **62**, 1030–1032 (1972).

[90] J. Feng, "Alternative scheme for studying gap solitons in an infinite periodic Kerr medium," Opt. Lett. **18,** 1302–1304 (1993).

[91] A. A. Sukhorukov, and Yu. S. Kivshar, "Generation and stability of discrete gap solitons," Opt. Lett. **28,** 2345–2347 (2003).

[92] A. A. Sukhorukov, D. Neshev, W. Krolikowski, and Yu. S. Kivshar, "Nonlinear Bloch-wave interaction and Bragg scattering in optically induced lattices," Phys. Rev. Lett. **92,** 093901–4 (2004).

[93] C. E. Rüter, J. Wisniewski, and D. Kip, "Prism coupling method to excite and analyze Floquet-Bloch modes in linear and nonlinear waveguide arrays," Opt. Lett. **31,** 2768–2770 (2006).

[94] O. Cohen, T. Schwartz, J. W. Fleischer, M. Segev, and D. N. Christodoulides, "Multiband vector lattice solitons," Phys. Rev. Lett. **91,** 113901–4 (2003).

[95] A. A. Sukhorukov and Yu. S. Kivshar, "Multigap discrete vector solitons," Phys. Rev. Lett. **91,** 113902–4 (2003).

[96] H. Buljan, O. Cohen, J. W. Fleischer, T. Schwartz, M. Segev, Z. H. Musslimani, N. K. Efremidis, and D. N. Christodoulides, "Random-phase solitons in nonlinear periodic lattices," Phys. Rev. Lett. **92,** 223901–4 (2004).

[97] K. Motzek, A. A. Sukhorukov, F. Kaiser, and Yu. S. Kivshar, "Incoherent multi-gap optical solitons in nonlinear photonic lattices," Opt. Express **13,** 2916–2923 (2005).

[98] O. Cohen, G. Bartal, H. Buljan, T. Carmon, J. W. Fleischer, M. Segev, and D. N. Christodoulides, "Observation of random-phase lattice solitons," Nature **433,** 500–503 (2005).

[99] D. Mandelik, H. S. Eisenberg, Y. Silberberg, R. Morandotti, and J. S. Aitchison, "Observation of mutually trapped multiband optical breathers in waveguide arrays," Phys. Rev. Lett. **90,** 253902–4 (2003).

[100] Y. Lahini, D. Mandelik, Y. Silberberg, and R. Morandotti, "Polarization dependent properties of waveguide arrays: band-structure anomaly and high-band localizations," Opt. Express **13,** 1762–1773 (2005).

[101] A. Fratalocchi, G. Assanto, K. A. Brzdakiewicz, and M. A. Karpierz, "Optical multiband vector breathers in tunable waveguide arrays," Opt. Lett. **30**, 174–176 (2005).

[102] E. Cubukcu, K. Aydin, E. Ozbay, S. Foteinopoulou, and C. M. Soukoulis, "Negative refraction by photonic crystals," Nature **423**, 604–605 (2003).

[103] D. R. Smith, W. J. Padilla, D. C. Vier, S. C. Nemat-Nasser, and S. Schultz, "Composite medium with simultaneously negative permeability and permittivity," Phys. Rev. Lett. **84**, 4184–4187 (2000).

[104] C. G. Parazzoli, R. B. Greegor, K. Li, B. E. C. Koltenbah, and M. Tanielian, "Experimental verification and simulation of negative index of refraction using Snell's law," Phys. Rev. Lett. **90**, 107401 (2003).

[105] H. Trompeter, T. Pertsch, F. Lederer, D. Michaelis, U. Streppel, A. Bräuer, and U. Peschel, "Visual observation of Zener tunneling," Phys. Rev. Lett. **96**, 023901–4 (2006).

[106] A. Fratalocchi, G. Assanto, K. Brzdakiewicz, and M. Karpierz, "All-optical switching and beam steering in tunable waveguide arrays," Appl. Phys. Lett. **86**, 051112–3 (2005).

[107] J. Meier, G. I. Stegeman, D. N. Christodoulides, Y. Silberberg, R. Morandotti, H. Yang, G. Salamo, M. Sorel, and J. S. Aitchison, "Beam interactions with a blocker soliton in one-dimensional arrays," Opt. Lett. **30,** 1027–1029 (2005).

[108] Y. V. Kartashov, L. Torner, and D. N. Christodoulides, "Soliton dragging by dynamic optical lattices," Opt. Lett. **30,** 1378–1380 (2005).

[109] I. L. Garanovich, A. A. Sukhorukov, and Yu. S. Kivshar, "Soliton control in modulated optically-induced photonic lattices," Opt. Express **13,** 5704–5710 (2005).

[110] S. R. Singh, M. I. Carvalho, and D. N. Christodoulides, "Higher-order space charge field effects on the evolution of spatial solitons in biased photorefractive crystals," Optics Comm. **130,** 288–294 (1996).

[111] K. G. Makris, S. Suntsov, D. N. Christodoulides, G. I. Stegeman, and A. Hache, "Discrete surface solitons," Opt. Lett. **30**, 2466–2468 (2005).

[112] S. Suntsov, K. G. Makris, D. N. Christodoulides, G. I. Stegeman, and A. Haché, R. Morandotti, H. Yang, G. Salamo, and M. Sorel, "Observation of discrete surface solitons," Phys. Rev. Lett. **96**, 063901–4 (2006).

[113] G. L. Alfimov, P. G. Kevrekidis, V. V. Konotop, and M. Salerno, "Wannier functions analysis of the nonlinear Schrödinger equation with a periodic potential," Phys. Rev. E **66,** 46608–6 (2002).

[114] F. Chen, M. Stepić, C. E. Rüter, D. Runde, D. Kip, V. Shandarov, O. Manela, and M. Segev, "Discrete diffraction and spatial gap solitons in photovoltaic $LiNbO_3$ waveguide arrays," Opt. Express **13,** 4314–4324 (2005).

[115] I. E. Tamm, "A possible kind of electron binding on crystal surfaces," Z. Phys. **76**, 849–850 (1932).

[116] H. Ohno, E. E. Mendez, J. A. Brum, J. M. Hong, F. Agulló-Rueda, L. L. Chang, and L. Esaki, "Observation of "Tamm states" in superlattices," Phys. Rev. Lett. **64**, 2555–2558 (1990).

[117] P. Yeh, A. Yariv, and C.-S. Hong, "Electromagnetic propagation in periodic stratified media. I. General theory," J. Opt. Soc. Am. **67**, 423–438 (1977).

[118] P. Yeh, A. Yariv, and A. Y. Cho, "Optical surface waves in periodic layered media," Appl. Phys. Lett. **32**, 104–105 (1978).

[119] W. J. Tomlinson, "Surface wave at a nonlinear interface," Opt. Lett. **5**, 323–325 (1980).

[120] A. D. Boardman, P. Egan, F. Lederer, U. Langbein, and D. Mihalache, "Third order nonlinear electromagnetic TE and TM guided waves," in: *Nonlinear Surface Electromagnetic Phenomena*, V. M. Agranovich, A. A. Maradudin, H.-E. Ponath, and G. I. Stegeman, eds. (Elsevier/North-Holland, Amsterdam, 1991), Vol. 29, pp. 73–287.

[121] D. Mihalache, M. Bertolotti, and C. Sibilia, "Nonlinear wave propagation in planar structures," Prog. Opt. **27**, 229–313 (1989).

[122] Yu. S. Kivshar, F. Zhang, and S. Takeno, "Nonlinear surface modes in monoatomic and diatomic lattices," Physica D **113**, 248–260 (1998).

[123] Ya. V. Kartashov, V. A. Vysloukh, and L. Torner, "Surface gap solitons," Phys. Rev. Lett. **96**, 073901–4 (2006).

[124] G. A. Siviloglou, K. G. Makris, R. Iwanow, R. Schiek, D. N. Christodoulides, G. I. Stegeman, Y. Min, and W. Sohler, "Observation of discrete quadratic surface solitons," Opt. Express **14,** 5508–5516 (2006).

[125] E. Smirnov, M. Stepić, C. E. Rüter, D. Runde, D. Kip, and V. Shandarov, "Observation of staggered surface solitary waves in one-dimensional waveguide arrays," Opt. Lett. **31,** 2338–2340 (2006).

[126] B. Malomed, and P. G. Kevrekidis, "Discrete vortex solitons," Phys. Rev. E **64,** 026601–6 (2001).

[127] J. W. Fleischer, G. Bartal, O. Cohen, O. Manela, M. Segev, J. Hudock, and D. N. Christodoulides, "Observation of vortex-ring "discrete" solitons in 2D photonic lattices," Phys. Rev. Lett. **92**, 123904–4 (2004).

[128] G. Bartal, O. Cohen, H. Buljan, J. W. Fleischer, O. Manela, and M. Segev, "Brillouin Zone Spectroscopy of Nonlinear Photonic Lattices," Phys. Rev. Lett. **94**, 163902–4 (2005).

[129] R. Fischer, D. Trager, D. N. Neshev, A. A. Sukhorukov, W. Krolikowski, C. Denz, and Yu. S. Kivshar, "Reduced-Symmetry Two-Dimensional Solitons in Photonic Lattices," Phys. Rev. Lett. **96**, 023905–4 (2006).

[130] H. Trompeter, W. Krolikowski, D. N. Neshev, A. S. Desyatnikov, A. A. Sukhorukov, Y. S. Kivshar, T. Pertsch, U. Peschel, and F. Lederer, "Bloch oscillations and Zener tunneling in two-dimensional photonic lattices," Phys. Rev. Lett. **96**, 053903–4 (2006).

[131] J. Yang. I. Makasyuk, H. Martin, P. G. Kevrekidis, B. A. Malomed, D. J. Frantzeskakis, and Z. Chen, "Necklace-like solitons in optically induced photonic lattices," Phys. Rev. Lett. **94**, 113902–4 (2005).

[132] C. Lou, X. Wang, J. Xu, Z. Chen, and J. Yang, "Nonlinear spectrum reshaping and gap-soliton-train trapping in optically induced photonic structures," Phys. Rev. Lett. **98**, 213903–4 (2007).

[133] A. Szameit, D. Blömer, J. Burghoff, T. Pertsch, S. Nolte, and A. Tünnermann, "Hexagonal waveguide arrays written with fs-laser pulses," Appl. Phys. B. **82,** 507–512 (2006).

[134] U. Röpke, H. Bartelt, S. Unger, K. Schuster, and J. Kobelke, "Two-dimensional high-precision fiber waveguide arrays for coherent light propagation," Opt. Express **15,** 6894–6899 (2007).

[135] P. G. Kevrekidis, B. A. Malomed, and Y. B. Gaididei, "Solitons in triangular and honeycomb dynamical lattices with the cubic nonlinearity," Phys. Rev. E **66**, 016609–10 (2002).

[136] O. Peleg, G. Bartal, B. Freedman, O. Manela, M. Segev and D. N. Christodoulides, "Conical diffraction and gap solitons in honeycomb photonic lattices," Phys. Rev. Lett. **98**, 103901–4 (2007).

[137] Y. V. Kartashov, V. A. Vysloukh, and L. Torner, "Rotary solitons in Bessel optical lattices," Phys. Rev. Lett. **93**, 093904–4 (2004).

[138] X. S. Wang. Z. G. Chen, and P. G. Kevrekidis, "Observation of discrete solitons and soliton rotation in optically induced periodic ring lattices," Phys. Rev. Lett. **96**, 083904–4 (2006).

[139] X. S. Wang. Z. G. Chen, and J. Yang, "Guiding light in optically induced ring lattices with a low-refractive-index core," Opt. Lett. **31**, 1887–1889 (2006).

[140] R. Fischer, D. N. Neshev, S. Lopez-Aguayo, A. S. Desyatnikov, A. A. Sukhorukov, W. Krolikowski, and Yu. S. Kivshar, "Observation of light localization in modulated Bessel optical lattices," Opt. Express **14**, 2825–2830 (2006).

[141] B. Freedman, G. Bartal, M. Segev, R. Lifshitz, D. N. Christodoulides, and J. W. Fleischer, "Wave and defect dynamics in nonlinear photonic quasicrystals," Nature **440**, 1166–1169 (2006).

[142] T. Schwartz, G. Bartal, S. Fishman and M. Segev, "Transport and Anderson localization in disordered two-dimensional photonic lattices," Nature **446**, 52–55 (2007).

[143] A. S. Desyatnikov, N. Sagemerten, R. Fischer, B. Terhalle, D. Träger, D. N. Neshev, A. Dreischuh, C. Denz, W. Krolikowski, and Y. S. Kivshar, "Two-dimensional self-trapped nonlinear photonic lattices," Opt. Express **14**, 2851–2863 (2006).

[144] N. Akozbek and S. John, "Optical solitary waves in two- and three-dimensional nonlinear photonic band-gap structures," Phys. Rev. E **57,** 2287–2319 (1998).

[145] T. M. Monro, D. J. Richardson, and P. J. Bennett, "Developing holey fibres for evanescent field devices," Electron. Lett. **35,** 1188–1189 (1999).

[146] J. B. Jensen, L. H. Pedersen, P. E. Hoiby, L. B. Nielsen, T. P. Hansen, J. R. Folkenberg, J. Riishede, D. Noordegraaf, K. Nielsen, A. Carlsen, and A. Bjarklev, "Photonic crystal fiber based evanescent-wave sensor for detection of biomolecules in aqueous solutions," Opt. Lett. **29,** 1974–1976 (2004).

[147] F. M. Cox, A. Argyros, and M. C. J. Large, "Liquid-filled hollow core microstructured polymer optical fiber," Opt. Express **14,** 4135–4140 (2006).

[148] B. J. Eggleton, C. Kerbage, P. S. Westbrook, R. S. Windeler, and A. Hale, "Microstructured optical fiber devices," Opt. Express **9,** 698–713 (2001).

[149] R. T. Bise, R. S. Windeler, K. S. Kranz, C. Kerbage, B. J. Eggleton, and D. J. Trevor, "Tunable photonic band gap fiber," in OSA Trends in Optics and Photonics (TOPS) 70, Optical Fiber Communication Conference Technical Digest, Postconference Edition (Optical Society of America, Washington, DC, 2002), 466-468.

[150] T. T. Larsen, A. Bjarklev, D. S. Hermann, and J. Broeng, "Optical devices based on liquid crystal photonic bandgap fibres," Opt. Express **11,** 2589–2596 (2003).

[151] T. T. Alkeskjold, J. Lægsgaard, A. Bjarklev, D. S. Hermann, A. Anawati, J. Broeng, J. Li, and S. T. Wu, "All-optical modulation in dye-doped nematic liquid crystal photonic bandgap fibers," Opt. Express **12,** 5857–5871 (2004).

[152] P. Steinvurzel, B. Kuhlmey, T. White, M. Steel, C. de Sterke, and B. Eggleton, "Long wavelength anti-resonant guidance in high index inclusion microstructured fibers," Opt. Express **12,** 5424–5433 (2004).

[153] A. Fuerbach, P. Steinvurzel, J. A. Bolger, A. Nulsen, and B. J. Eggleton, "Nonlinear propagation effects in antiresonant highindex inclusion photonic crystal fibers," Opt. Lett. **30,** 830–832 (2005).

[154] S. Lebrun, P. Delaye, R. Frey, and G. Roosen, "High-efficiency single-mode Raman generation in a liquid-filled photonic bandgap fiber," Opt. Lett. **32,** 337–339 (2007).

[155] R. Zhang, J. Teipel, and H. Giessen, "Theoretical design of a liquid-core photonic crystal fiber for supercontinuum generation," Opt. Express **14,** 6800–6812 (2006).

[156] F. Couny, F. Benabid, P. J. Roberts, M. T. Burnett, and S. A. Meier, "Identification of Bloch-modes in hollow-core photonic crystal fiber cladding," Opt. Express **15,** 325–338 (2007).

[157] A. B. Aceves, C. De Angelis, A. M. Rubenchik, and S. K. Turitsyn, "Multidimensional solitons in fiber arrays," Opt. Lett. **19,** 329–331 (1994).